OUKA
The University of Osaka
Institutional Knowledge Archive

Title	Emissive Sumanene Derivatives: Effect of Bowl Structure on Their Optical Properties
Author(s)	Han, Junyi
Citation	大阪大学, 2026, 博士論文
Version Type	VoR
URL	https://doi.org/10.18910/105426
rights	
Note	

The University of Osaka Institutional Knowledge Archive : OUKA

https://ir.library.osaka-u.ac.jp/

The University of Osaka

Doctoral Dissertation

Emissive Sumanene Derivatives: Effect of Bowl Structure on Their Optical Properties

(発光性スマネン誘導体:おわん構造がもたらす光物性への影響)

HAN JUNYI

January 2026

Graduate School of Engineering

The University of Osaka

Table of contents

Chapter 1 **Introduction**

Section 1. Structure–property relations in luminophores 1

Section 2. Sumanene-based curved frameworks 3

Section 3. This work 6

References 8

Chapter 2 **Sumanene-functionalized bis(terpyridine)-ruthenium(ii) complexes showing photoinduced structural change and cation sensing**

Section 1. Ru(II) terpyridine complexes and curved π-systems in ion sensing 10

Section 2. Synthesis and photophysical properties of sumanene–Ru(II) complexes 12

Section 3. Cation sensing property 23

Section 4. Summary 26

Experimental section 28

References 52

Chapter 3 **Derivatization of trioxosumanene by Lewis acid-mediated Suzuki-Miyaura coupling and an unprecedented ring opening**

Section 1. Unique electronic features of trioxosumanene 56

Section 2. Synthesis and properties of trioxosumanene derivatives 57

Section 3. Unexpected ring-opening reaction 63

Section 4. Summary 64

Experimental section 66

References 82

Chapter 4 **High quantum yield NIR emission via charge transfer states in Buckybowl-TPA based D–A systems**

Section 1. Design strategies and functional significance of NIR dyes 86

Section 2. Synthesis and characterization of TPA-TOS 88

Section 3. Spectroscopic analyses 90

Section 4. Transient absorption and time-resolved spectroscopy 96

Section 5. Plausible discussion about the effect of the curved-π structure 102

Section 6. Summary 105

Experimental section 107

References 125

Conclusions 129
List of publications 132
Copyright 133
Acknowledgments 134

Chapter 1. Introduction

Section 1. Structure–property relations in luminophores

Luminous materials have attracted sustained interest because their emission underpins a wide spectrum of technologies—from flat-panel displays and solid-state lighting to bioimaging, chemical sensing, information security, and energy conversion.[1] Over the past two decades, diversified molecular and nanostructured platforms have emerged, including phosphorescent organometallic emitters that harvest triplet excitons for near-unity internal quantum efficiency,[2] aggregation-induced-emission (AIE) luminogens that suppress non-radiative decay upon clustering,[3] and highly emissive metal-halide perovskite nanocrystals with narrow bandwidths and solution processability.[4] Foundational photophysical principles continue to guide materials discovery and device engineering,[5] while application-oriented advances in sensing and imaging leverage turn-on/turn-off responses,[6] ratiometric readouts,[7] and environment-responsive emission.[8] Despite rapid progress, key challenges remain in operational stability, color purity, and scalable, sustainable synthesis—motivating ongoing efforts to couple molecular design with device-level optimization. Recent progress in thermally activated delayed fluorescence (TADF), organic room temperature phosphorescence (RTP), and nanocrystal surface chemistry further illustrates how emitter design and interfacial control can push efficiency and stability.[9-13]

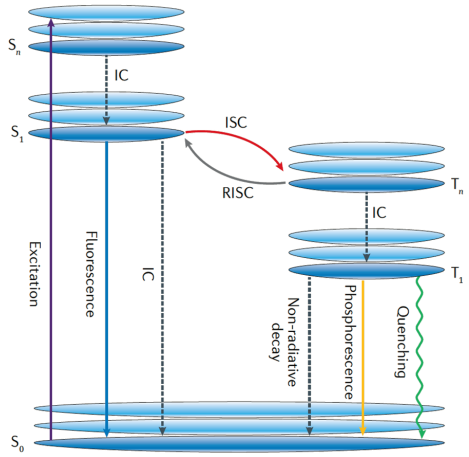

Figure 1. Schematic Jablonski diagram illustrating electronic states and intersystem crossing (ISC) / reverse intersystem crossing (RISC) pathways relevant to luminescent processes.

Understanding structure–property relationships in luminescence organic compounds is essential both for elucidating excited-state processes and for realizing functional materials in nonlinear optics, up-conversion, and lasing applications.[14, 15] Fluorescence, the spontaneous emission from an excited singlet to the ground state, follows the same spin and symmetry selection rules as absorption. Phosphorescence, emission from an excited triplet state to the singlet ground state, is enabled by ISC

from the singlet manifold and proceeds through spin-forbidden but spin–orbit coupling (SOC) assisted transitions, following relaxed spin and symmetry selection rules. Excited-state decay pathways comprise radiative and nonradiative processes (Figure 1); the latter are often promoted by large-amplitude conformational relaxation, whereas rigid chromophores tend to favor radiative decay. Consequently, planar and rigid π systems have long dominated emitter design. However, purely planar chromophores can be limiting for advanced targets such as polarized emission, organic electronics, spintronics, and nonlinear optics, etc.[16] Nonplanar conjugated molecules introduce conformational asymmetry and uneven charge distribution, which lead to distinctive photophysical and electronic behaviors. These systems are commonly classified into fused architecture and rotatable architectures. Fused nonplanar architectures, exemplified by fullerenes,[17] bowls,[18] helicenes, and other cyclic or bowl–helical hybrids,[19] impart smoothly varying curvature that modulates π conjugation across the scaffold. In contrast, rotatable nonplanar motifs, such as U-shaped,[20] square-shaped,[21] X-shaped,[22] and hash-mark-shaped[23] topologies, disrupt conjugation locally through torsion at specific junctions. The resulting tunability of excited-state dynamics continues to drive interest in the design, synthesis, and performance optimization of nonplanar organic emitters.

In addition, the curvature offers a simple structural handle to enhance SOC in π-conjugated organics. Bending induces local pyramidalization and σ–π mixing, tilting adjacent p orbitals and breaking pure π symmetry. The spin–orbit matrix element that governs ISC and RISC therefore increases, approximately scaling as $|\mathrm{SOC}| \propto R\sin\theta$, where R is the effective orbital separation distance and θ is the dihedral between two π orbitals. Planar chromophores ($\theta \approx 0$) minimize this term, whereas curved buckybowls and helicenes enlarge θ and amplify SOC (Figure 2).[24] The resulting stronger spin mixing facilitates singlet–triplet population exchange (ISC and RISC), promoting TADF, RTP, and long-lived charge-separated states.

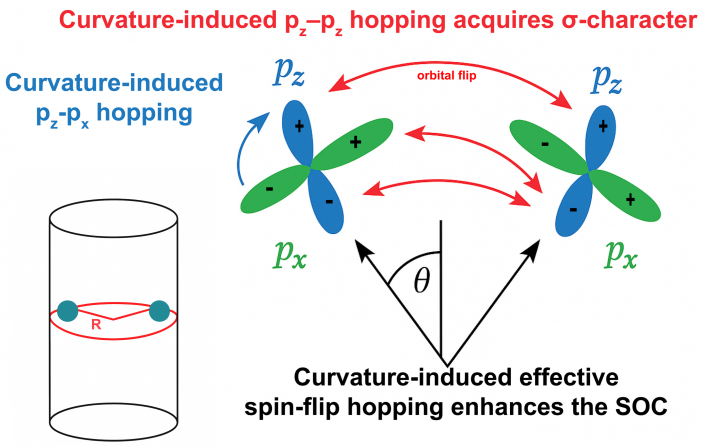

Figure 2. Curvature-induced π–σ rehybridization, blue arrows represent newly allowed p_z–p_x hopping, red arrows indicate curvature-modified p_z–p_z hopping with σ-character admixture

Section 2. Sumanene-based curved frameworks

Sumanene is a bowl-shaped, curved π-conjugated molecule possessing C_{3v} symmetry, composed of a central benzene ring fused to three alternating benzene and cyclopentadiene units. This architectural arrangement generates a rigid, concave–convex framework and represents the smallest C_{3v}-symmetric fragment of the fullerene (C_{60}) surface, as well as a structural model for the hemispherical end-caps of carbon nanotubes (Figure 3). The curvature introduces intrinsic pyramidalization at the carbon atoms, bending the π-system out of planarity and producing a characteristic bowl depth that defines its molecular geometry and electronic structure. From a synthetic perspective, the development of sumanene marked a long-standing challenge due to the difficulty of controlling multi-step annulation and maintaining the bowl geometry under solution conditions. This challenge was overcome in 2003, when Sakurai and co-workers achieved the first solution-phase synthesis of sumanene through a carefully designed sequence involving selective cyclization, rearrangement, and oxidative aromatization steps. This breakthrough not only provided access to the parent bowl compound but also opened the door to a broad family of functionalized sumanene derivatives, enabling systematic exploration of curvature-dependent properties.[25] This breakthrough not only provided access to the parent bowl compound but also enabled systematic exploration of functionalized sumanene derivatives and their curvature-dependent properties. Furthermore, the curved architecture of sumanene imparts characteristic electronic transport behaviors. Its polarized π-surface and uneven charge distribution facilitate anisotropic electron mobility, making it a valuable model for probing charge conduction across nonplanar aromatic frameworks. Derivatives bearing electron-donating or electron-withdrawing substituents have revealed tunable redox properties and frontier orbital energies, illustrating how curvature modulates conductivity pathways.[26]

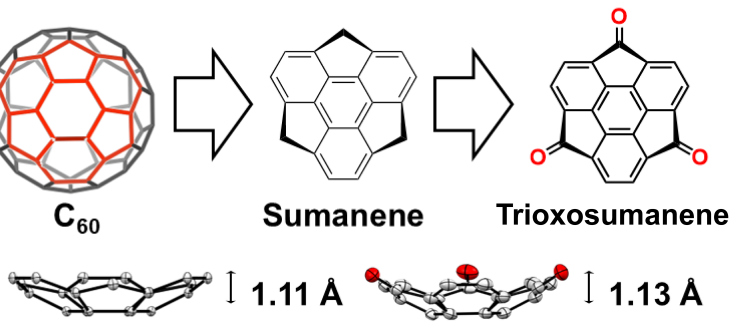

Figure 3. Molecular structures of sumanene and its triketone derivative (trioxosumanene), highlighting bowl curvature and conjugated frameworks

In addition to its distinctive structural and electronic properties, sumanene is also known for its

remarkable metal cation-binding ability, arising from the polarized concave–convex topology. Early theoretical investigations predicted that the convex face of the six-membered rim ring provides the most favorable binding environment, offering the highest stabilization energy for alkali metal cations due to optimal electrostatic interactions and curvature-induced orbital polarization.[27] Subsequent experimental studies validated these theoretical predictions, demonstrating that neutral sumanene can indeed accommodate metal cations on its convex face through noncovalent interactions, with binding geometries consistent with computational models.[28] These findings established sumanene as a rare example of a neutral, curvature-defined π-receptor capable of selective ion encapsulation without relying on classical Lewis basic sites. More recent work has further uncovered the Cs^+ sensing capability of neutral sumanene, revealing distinct optical and electronic signatures upon coordination.[29] The high curvature and rigid bowl geometry create a localized electrostatic potential that is particularly well-matched to the large ionic radius of Cs^+, enabling selective binding and detectability even in complex environments (Figure 4). This behavior positions sumanene as a promising scaffold for the design of curved π-based ion receptors and chemosensors, where bowl depth, substituents, and π-surface polarization can be tuned to modulate selectivity and sensitivity.

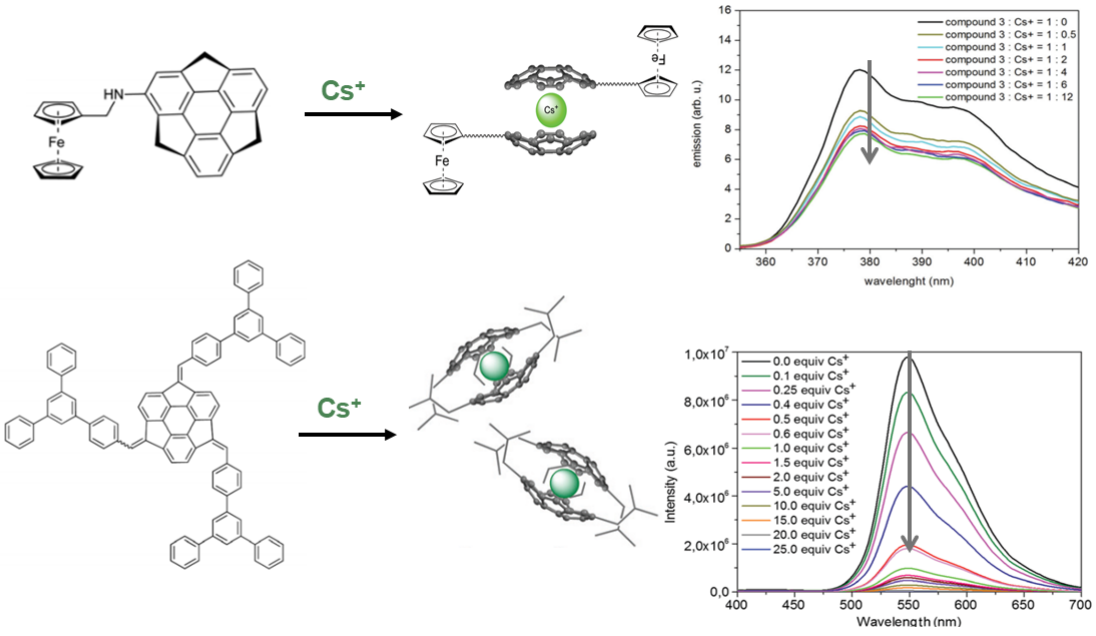

Figure 4. Illustration of Cs^+ binding sites and fluorescent response in sumanene derivatives, emphasizing curvature-dependent cation interactions.[30]

Like sumanene, its triketone derivative trioxosumanene also adopts a pronounced bowl-shaped geometry, in which each of the three carbonyl groups is fully conjugated with the curved π-framework.[31] Introduction of electron-withdrawing C=O units not only preserves the intrinsic

concave–convex topology but also slightly enhances the molecular curvature. This is reflected in the bowl depth at the benzylic carbon atoms, measured to be 99 pm, which is marginally greater than that of the parent sumanene (90 pm).[32] This increased curvature indicates increased pyramidalization of the aromatic carbon atoms and a greater deviation from planarity, both of which can influence the frontier orbital distribution and the associated photophysical or electronic responses. Electrochemical studies have revealed that trioxosumanene exhibits two well-separated reduction processes, with the first reduction occurring at −0.92 V and the second at −1.43 V (vs. Fc/Fc^{+}). These values demonstrate that trioxosumanene behaves as a strong electron acceptor, substantially more electron-deficient than its hydrocarbon precursor due to the presence of three carbonyl functionalities. The stabilization of the LUMO through conjugation with the curved π-system further contributes to its enhanced acceptor strength. The combination of pronounced curvature and electron-deficient character makes trioxosumanene a compelling platform for studying curvature-induced orbital interactions, charge-transfer behavior, and excited-state dynamics in nonplanar π-conjugated systems. [33]

The rigid, curved π-surface of sumanene derivatives also confers distinctive electronic and photophysical characteristics, arising directly from its bowl-shaped architecture. Curvature introduces measurable σ–π mixing, bending the p-orbitals out of coplanarity and creating a locally polarized π-framework. This geometric distortion enhances SOC by facilitating effective spin–flip pathways and modifying the orbital angular momentum contributions, while simultaneously reshaping the frontier molecular orbitals through curvature-induced rehybridization and uneven charge distribution.

These properties position sumanene derivatives as a model curved π-system for probing how molecular geometry dictates electronic structure and excited-state behavior. Studies on sumanene and its derivatives have provided valuable insights into excited-state relaxation, intersystem crossing dynamics, charge transport, and curvature-dependent SOC modulation, linking structural distortion to functional photophysical outcomes. Sun et al. showed that pyrazine-fused trichalcogenasumanenes translate these effects into strong nonlinear optical behavior. The bowl-shaped C_{3v} framework increases SOC and promotes ISC to long-lived triplet states, while pyrazine fusion creates a donor–acceptor orbital pattern that strengthens charge-transfer transitions. Under 532 nm excitation, both derivatives display pronounced reverse saturable absorption arising from triplet–triplet absorption, giving nonlinear coefficients and optical-limiting thresholds superior to C_{60}. These results highlight how curvature and D–A orbital engineering enable efficient nonlinear optical (NLO) and optical power limiting (OPL) materials (Figure 5).[34]

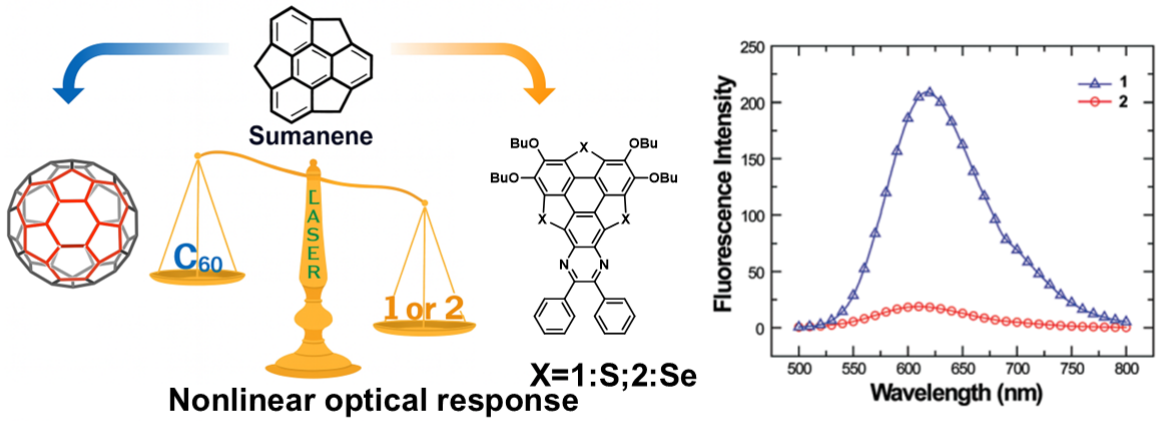

Figure 5. Nonlinear optical response of pyrazine-fused trichalcogenasumanenes

Section 3. This work

In this doctoral dissertation, the author aims to exploit the curved architecture of sumanene to construct a series of novel ion-responsive molecules capable of rapid and accurate recognition of alkali metal ions. Furthermore, by leveraging the combined curvature and electron-accepting ability of trioxosumanene, the author develops new luminescent molecules based on this unique scaffold (Scheme 1).

In Chapter 2, four luminescent Ru(II) complexes (C1–C4) bearing sumanene-functionalized terpyridine ligands were synthesized, in which the curved sumanene unit introduced ligand-centered emission and enabled facile rotation around the sumanene–terpyridine bond. This structural flexibility facilitated dual emission through a twisted intramolecular charge transfer (TICT) process involving photoinduced electron transfer from sumanene to the terpyridine–Ru center followed by back-transfer to the phenyl moiety. Moreover, the complexes displayed sensitive Li^+ recognition, likely arising from cation–π interactions on the convex face of the sumanene core.

In Chapter 3, a series of trioxosumanene derivatives were synthesised via Lewis acid–mediated Suzuki–Miyaura cross-coupling, revealing the intrinsically strong electron-accepting character of the trioxosumanene core. Their optical properties consistently reflected this electron-deficient nature. Notably, the bowl strain in the 2-hydroxyphenyl derivative enabled a ring-opening process adjacent to the substituent at room temperature, a transformation that typically requires much harsher activation conditions.

In Chapter 4, a novel bowl-shaped NIR dye was designed and synthesised, featuring trioxosumanene (TOS) as an electron-accepting curved core and triphenylamine (TPA) as the donor. TPA-TOS shows solvent-dependent photophysics, displaying weak UV emission in polar media but intense NIR emission (650–850 nm) in nonpolar environments with a quantum yield exceeding 60%,

enabled by a photo-relaxation pathway involving exciton relaxation from local excitation to a CT state, followed by TADF and RTP to a long-lived charge-separated state. The amphiphilic character, efficient NIR dual emission, and long-lived CS state are attributed to enhanced spin–orbit coupling arising from the curved sumanene scaffold, establishing TPA-TOS as a promising platform for NIR materials and non-planar photophysics.

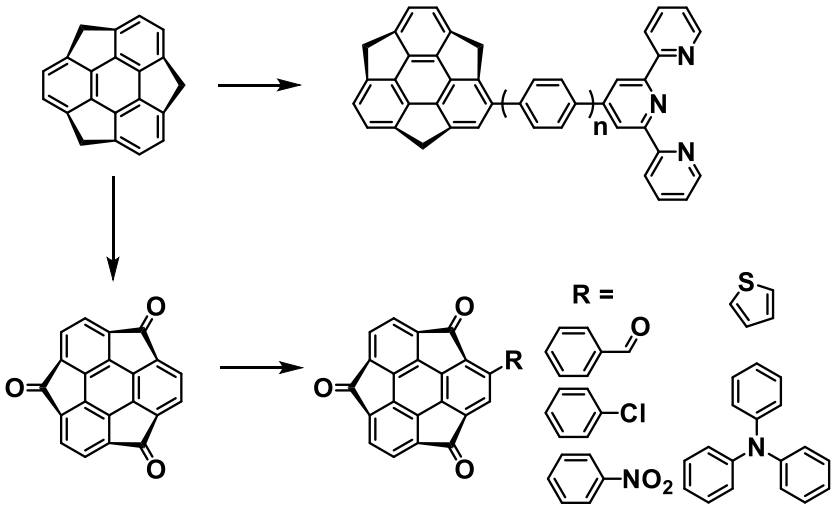

Scheme 1. Selected structures of the sumanene derivatives synthesized in this study.

References

1. B. Valeur and M. N. Berberan-Santos, *Mol. Fluoresc.: Princ. Appl.*, John Wiley & Sons, 2013.
2. S. Welter, K. Brunner, J. Hofstraat and L. De Cola, *Nature*, 2003, **421**, 54.
3. J. Mei, N. L. Leung, R. T. Kwok, J. W. Lam and B. Z. Tang, *Chem. Rev.*, 2015, **115**, 11718.
4. L. Protesescu, S. Yakunin, M. I. Bodnarchuk, F. Krieg, R. Caputo, C. H. Hendon, R. X. Yang, A. Walsh and M. V. Kovalenko, *Nano Lett.*, 2015, **15**, 3692.
5. A. Morteza Najarian, M. Vafaie, B. Chen, F. P. García de Arquer and E. H. Sargent, *Nat. Rev. Phys.*, 2024, **6**, 219.
6. J. Geng, Y. Chen, S. Xie, H. Lin and X. Wang, *Inorg. Chem.*, 2023, **62**, 5158.
7. C.-Y. Chen and C.-T. Chen, *Chem. Commun.*, 2011, **47**, 994.
8. X. Hu, J. Zhang, Z. Yu, Y. Xie, H. He, J. Qi, X. Dong, Y. Lu, W. Zhao and W. Wu, *Nanomedicine*, 2015, **11**, 1939.
9. J. M. Dos Santos, D. Hall, B. Basumatary, M. Bryden, D. Chen, P. Choudhary, T. Comerford, E. Crovini, A. Danos and J. De, *Chem. Rev.*, 2024, **124**, 13736.
10. H. J. Kim and T. Yasuda, *Adv. Opt. Mater.*, 2022, **10**, 2201714.
11. W. Dai, Y. Jiang, Y. Lei, X. Huang, P. Sun, J. Shi, B. Tong, D. Yan, Z. Cai and Y. Dong, *Chem. Sci.*, 2024, **15**, 4222.
12. H. Uoyama, K. Goushi, K. Shizu, H. Nomura and C. Adachi, *Nature*, 2012, **492**, 234.
13. V. Morad, A. Stelmakh, M. Svyrydenko, L. G. Feld, S. C. Boehme, M. Aebli, J. Affolter, C. J. Kaul, N. J. Schrenker and S. Bals, *Nature*, 2024, **626**, 542.
14. A. Barh, P. J. Rodrigo, L. Meng, C. Pedersen and P. Tidemand-Lichtenberg, *Adv. Opt. Photonics*, 2019, **11**, 952.
15. B. H. Wallikewitz, M. de la Rosa, J. H. W. Kremer, D. Hertel and K. Meerholz, *Adv. Mater.*, 2010, **22**, 531.
16. R. Kumar, H. Aggarwal and A. Srivastava, *Chem. Eur. J.*, 2020, **26**, 10653.
17. H. Peng, F. S. Leung, A. X. Wu, Y. Dong, Y. Dong, N.-T. Yu, X. Feng and B. Z. Tang, *Chem. Mater.*, 2004, **16**, 4790.
18. M. A. Majewski and M. Stępień, *Angew. Chem.*, 2019, **131**, 90.
19. G. Povie, Y. Segawa, T. Nishihara, Y. Miyauchi and K. Itami, *Science*, 2017, **356**, 172.
20. H. Tsujimoto, D.-G. Ha, G. Markopoulos, H. S. Chae, M. A. Baldo and T. M. Swager, *J. Am. Chem. Soc.*, 2017, **139**, 4894.
21. F. Schlosser, M. Moos, C. Lambert and F. Würthner, *Adv. Mater.*, 2012, **25**, 410.
22. Y. Wu, J.-M. Han, M. Hong, M. D. Krzyaniak, A. K. Blackburn, I. R. Fernando, D. D. Cao, M. R. Wasielewski and J. F. Stoddart, *J. Am. Chem. Soc.*, 2018, **140**, 515.
23. Y. Inoue, D. Sakamaki, Y. Tsutsui, M. Gon, Y. Chujo and S. Seki, *J. Am. Chem. Soc.*, 2018,

140, 7152.

24. D. Huertas-Hernando, F. Guinea and A. Brataas, *Phys. Rev. B*, 2006, **74**, 155426.
25. H. Sakurai, T. Daiko and T. Hirao, *Science*, 2003, **301**, 1878.
26. S. Higashibayashi and H. Sakurai, *Chem. Lett.*, 2011, **40**, 122.
27. D. Vijay, H. Sakurai, V. Subramanian and G. N. Sastry, *Phys. Chem. Chem. Phys.*, 2012, **14**, 3057.
28. S. N. Spisak, Z. Wei, N. J. O'Neil, A. Y. Rogachev, T. Amaya, T. Hirao and M. A. Petrukhina, *J. Am. Chem. Soc.*, 2015, **137**, 9768.
29. A. Kasprzak and H. Sakurai, *Dalton Trans.*, 2019, **48**, 17147.
30. A. Kasprzak, *Angew. Chem. Int. Ed.*, 2024, **63**, e202318437.
31. T. Amaya, M. Hifumi, M. Okada, Y. Shimizu, T. Moriuchi, K. Segawa, Y. Ando and T. Hirao, *J. Org. Chem.*, 2011, **76**, 8049.
32. K. Kanahara, M. D. M. R. Badal, S. Hatano, M. Abe, S. Higashibayashi, N. Takashina and H. Sakurai, *Bull. Chem. Soc. Jpn.*, 2015, **88**, 1612.
33. S. Higashibayashi, B. B. Shrestha, Y. Morita, M. Ehara, K. Ohkubo, S. Fukuzumi and H. Sakurai, *Chem. Lett.*, 2014, **43**, 1297.
34. J. Sun, Y. Sun, C. Yan, D. Lin, Z. Xie, S. Zhou, C. Yuan, H.-L. Zhang and X. Shao, *J. Mater. Chem. C*, 2018, **6**, 13114.

Chapter 2. Sumanene-functionalized bis(terpyridine)-ruthenium(ii) complexes showing photoinduced structural change and cation sensing

Section 1. Ru(II) terpyridine complexes and curved π-systems in ion sensing

In the design strategy of sensing materials based on coordination compounds, metal fragments are used as the reporter units that change physical properties such as color, emission intensity, and electrochemical potentials by interacting with the target ions and molecules.[1] In this context, Ru(II) complexes are useful scaffolds and widely applied to optical sensors due to their photosensitising ability induced by enough long high-energy excited state to facilitate the desired electron-/energy-transfer process or photochemical reaction.[2, 3] Especially, $[Ru(terpy)]^{2+}$ (terpy = 2,2':6',2''-terpyridine) avoids diastereomeric problems in preparation, which is often observed in $[Ru(bpy)_3]^{2+}$ (bpy = 2,2'-bipyridine) and allows high stability.[4, 5] Various applications of $[Ru(terpy)]^{2+}$-based systems are reported, in which donor or acceptor moieties and/or π-conjugation system are introduced[6-12] to overcome the intrinsic low emission property of $[Ru(terpy)]^{2+}$. Some selected Ru(II) complexes also show dual emission, which occurred simultaneously from LC and MLCT states or different MLCT states.[13-18] Especially in the case of highly conjugated $[Ru(terpy)]^{2+}$ complex, it is confirmed that the dual emission caused by the electronic coupling of the π−π* and the MLCT states due to the structure planarisation at the excited state, which is the potential strategy to the preparation of white emitters.[19, 20] However, the application of the $[Ru(terpy)]^{2+}$ system to the sensing materials draws much less attention compared to the effort to improve its emission property, probably because of the difficulty in the concomitance of the emission property improvement and the effective target recognition.

Sumanene is a fullerene fragment and therefore possesses a unique curved structure.[21] This structural feature has been the source of the emergence of unique physical properties in various kinds of sumanene derivatives.[22-27] In addition, it is worth noting that sumanene shows metal cation trapping ability. In the early stage, Sastry et al. systematically explored Li^+, Na^+, K^+ and Cu^+ complexes of sumanene in terms of the formation of cation-π interaction by employing ab initio quantum mechanical tools.[28] They concluded that the complex in which the metal ion binds to the convex side of the 6-membered rim ring (Figure 1) is the most stable. This assumption was experimentally proofed by the X-ray structural characterisation of a novel complex of six potassium ions sandwiched by convex faces of two sumanene anions.[29] The author also recently reported the Cs^+ sensing ability of neutral sumanene.[30-32]

Based on the above reported knowledges about the high scalability of $[Ru(terpy)]^{2+}$ complexes for various applications and the cation trapping ability of curved π-conjugated sumanene skeleton, the author newly designed and synthesised a total of four homo- and heteroleptic complexes **C1**-**C4** to apply in stable $[Ru(terpy)]^{2+}$ complex (Figure 1). The experimental results showed that all the complexes were emissive at room temperature in solution on the excitation of ligand-centred π–π* band. Significantly, **C2**, **C3** and **C4** exhibited dual emission properties caused by the molecular twisting in the excited state, which was evaluated by spectroscopic and theoretical analyses. The cation sensing ability of **C1**-**C4** was also investigated to find that all of them work as Li^+ detectors, probably via the cation–π interaction.

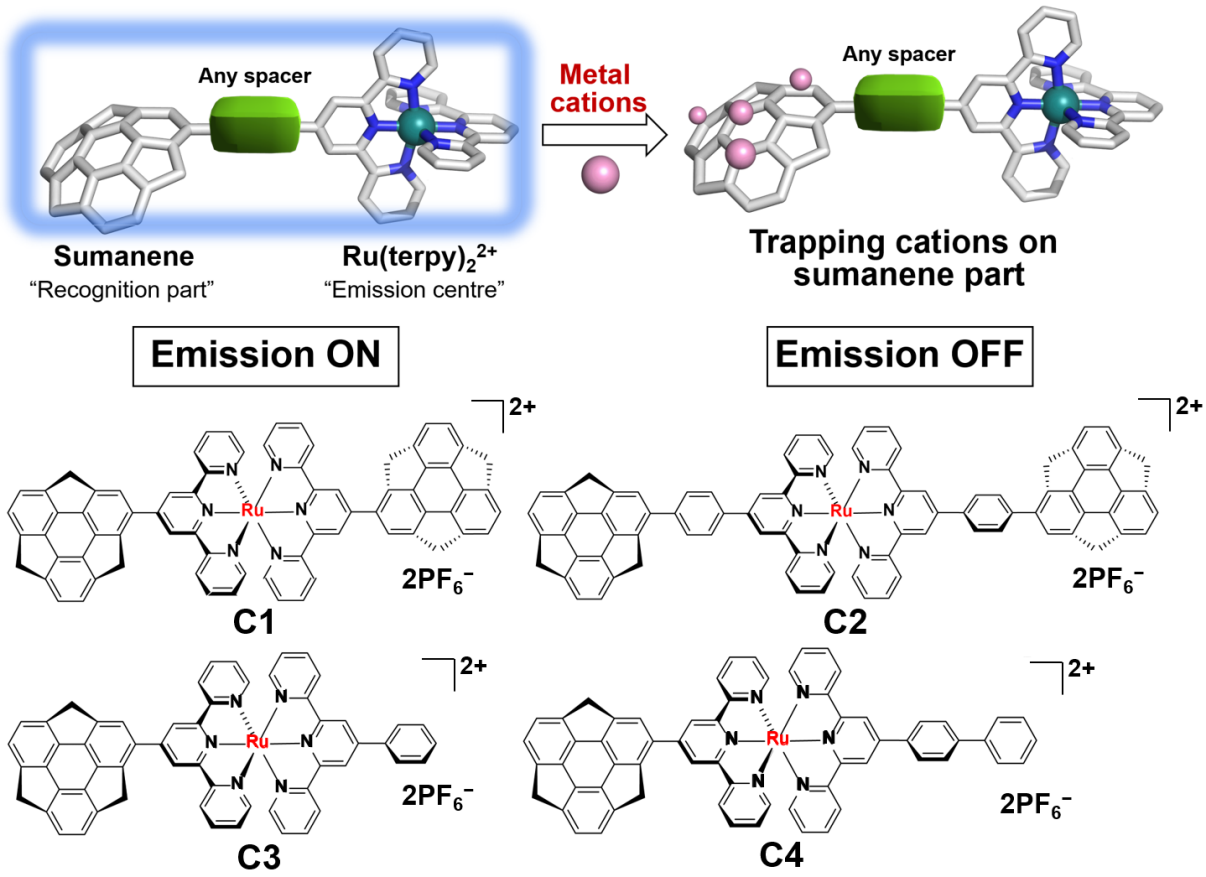

Figure 1. A concept of sumanene-Ru(II) cation sensors and the structures of **C1-C4**.

Section 2. Synthesis and photophysical properties of sumanene–Ru(II) complexes

Regarding the ligand preparation, the 4-sumanenylterpyridine **L1** was synthesised by Kröhnke reaction from formylsumanene,[33] and the phenylene-tethered derivative **L2** by Pd-catalyzed Suzuki-Miyaura coupling reaction from bromosumanene,[24] respectively (Scheme 1). Complexation of **L1** with 50 mol% of $RuCl_2(DMSO)_4$ the author performed in $EtOH/CHCl_3$ mixed solution, followed by the counterion exchange reaction with an excess amount of NH_4PF_6 yielded **C1** as red solids. The same method was used to obtain the red solid **C2** using **L2** as a ligand. Unsymmetrical **C3** and **C4** were prepared by the complexation of **L1** with a stoichiometric amount of Ru^{2+} complexes **5** and **6**.[34] In addition to **C1-C4**, the

control complexes **SC1-SC3** without sumanene unit were also prepared. Their characterisation was performed using ^{1}H NMR, correlation spectroscopy (COSY) NMR, and matrix-assisted laser desorption-ionisation time-of-flight mass spectrometry (MALDI-TOF-MS). The optimized structures obtained by density functional theory (DFT) calculation showed the terpyridine moieties in the complexes were flat and the coordination sphere did not show significant distortion (Figure 2). The torsion angles of sumanene and terpy moieties in all the complexes were around 45°.

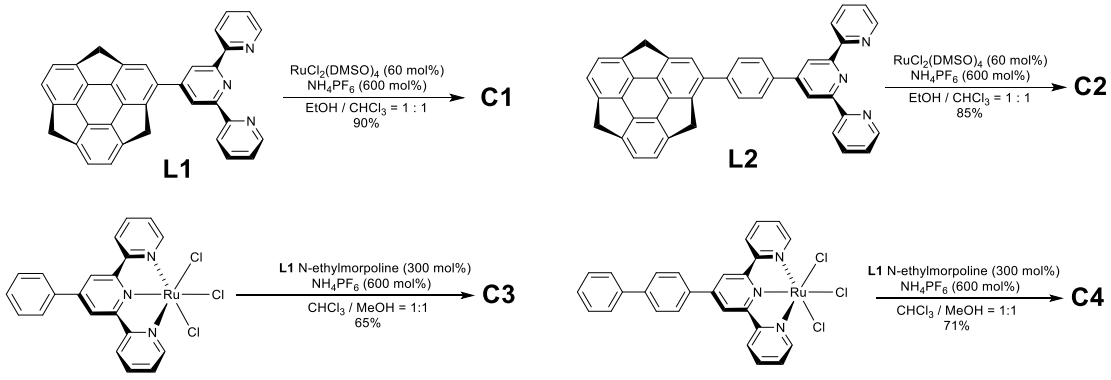

Scheme 1. Synthesis of **C1**, **C2**, **C3** and **C4**.

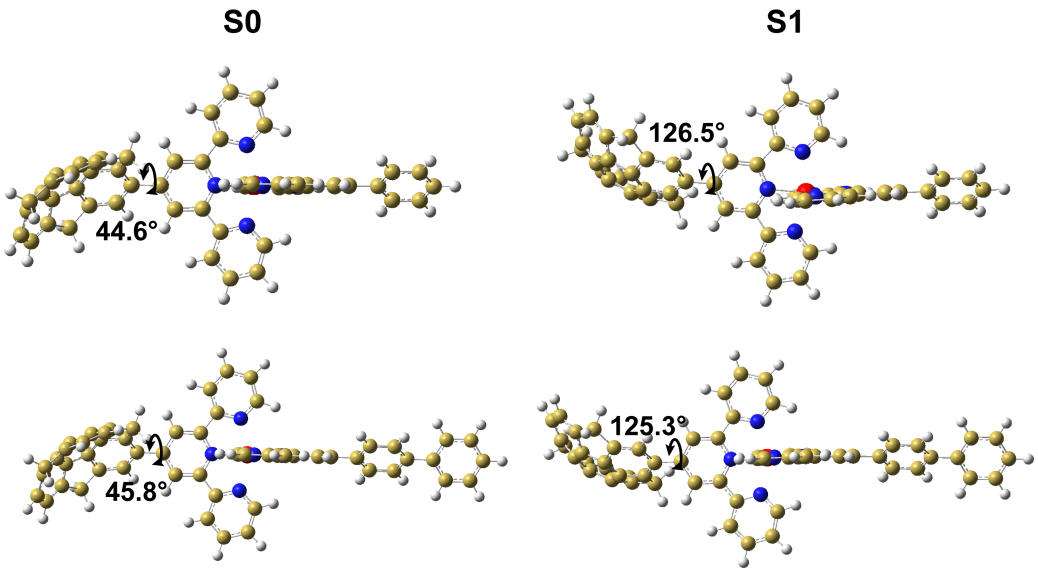

Figure 2. Optimized structure of **C3** and **C4** in both S0 and S1 states.

The photophysical properties of two ligands were first investigated by UV−vis absorption and fluorescence spectroscopy. UV−vis spectra of **L1** and **L2** diluted in CH_3CN show absorption peaks at 245 and 295 nm. Both **L1** and **L2** showed strong emissions at 420 nm (Figure 3A). The details of the optical properties of **C1**−**C4** were next investigated (Table 1). All the absorption spectra of the complexes exhibited similar patterns, intense bands around 280-350 nm and around 500 nm (Figure 3B). Time-dependent (TD)-DFT calculation revealed that the former band was composed of the sumanene π−π* transition (280-350 nm) and the ligand-to-ligand charge transfer (LLCT) from sumanene to terpyridine core (350-400 nm). The strong absorption peak at around 500 nm was attributable to the mixture of Ru(II) to terpyridine charge transfer (MLCT) and sumanene to terpyridine charge transfer (LLCT) bands.

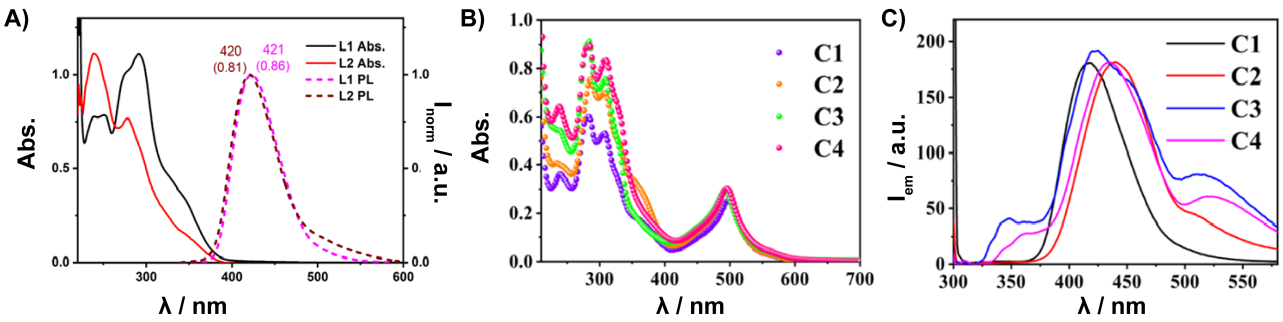

Figure 3. A) Absorption (solid lines) and photoluminescence spectra (λ_{ex} = 300 nm, dashed lines) of **L1** and **L2** in CH_3CN (1.0×10^{-6} M), B) absorption and C) photoluminescence spectra (λ_{ex} = 300 nm) of **C1-C4** in CH_3CN (1.0×10^{-5} M) at 300 K

Table 1. Photophysical properties of complexes **C1-C4** at 300 K.

complex	λ_{abs} [nm][a] ($\varepsilon \times 10^4$ [$M^{-1} \times cm^{-1}$])	λ_{em} [nm][ab] ($\Phi_{em} \times 10^{-2}$)
C1	283 (6.0), 308 (5.3), 494 (2.5)	403 (0.8)
C2	286 (7.5), 309 (6.9), 497 (3.0)	442 (4.3)
C3	287 (9.1), 309 (7.5), 492 (3.1)	424 (7.9), 511 (3.2)
C4	290 (9.1), 308 (8.3), 495 (3.1)	434 (8.4), 534 (3.3)

[a]In CH_3CN (1.0×10^{-5} M). [b]λ_{ex} = 300 nm.

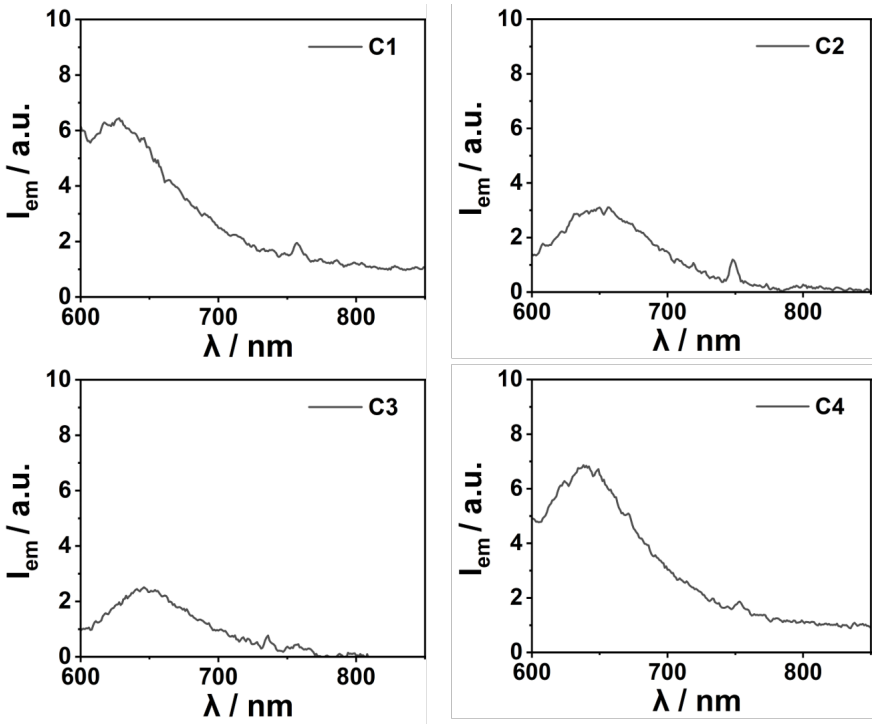

Figure 4. Emission spectra of **C1-C4** in CH_3CN (1.0×10^{-4} M) at 298 K. Excitation wavelength was 510 nm for all the spectra.

Meanwhile, the emission spectra of **C1-C4** exhibited significant differences depending on the molecular structure (Figure 3C). All the Ru(II) complexes showed only weak emission at around 650 nm by excitation at MLCT band (510 nm) at 298 K (Figure 4). Meanwhile, they exhibited one broad, strong emission band, which lay at 400-500 nm by excitation at the π−π*

band (300 nm). This contrasted with most $[Ru(terpy)_2]^{2+}$ complexes, in which the internal conversion process is very fast and efficient, and therefore, ligand centre (LC) emission is quenched effectively to give only weak emission. Indeed, the control compounds **SC1**-**SC3** did not show any strong emission at around 500 nm (Figure 5), indicating that the presence of sumanene induced a different relaxation process from the conventional $[Ru(terpy)_2]^{2+}$ complexes. Furthermore, one small shoulder peak at 500 nm in **C2** and one additional broadened band at 530 nm in **C3** and **C4** were also observed. To reveal the source of them, the author first chose **C4** as a representative and investigated its concentration effect on the emission property (Figure 6A). As a result, it was found that **C4** started to show aggregation-caused quenching at more than 5×10^{-6} M, while the emission intensity decreased at lower concentration ($< 1 \times 10^{-6}$ M). However, the second emission bands at more than 500 nm were retained even at 1×10^{-7} M, indicating that the source of the second band existed in the intramolecular process rather than the intermolecular one, such as the formation of some specific excimer. The same tendencies were confirmed in **C2** and **C3** (Figure 7). Emission spectra of **C4** in a CH_3CN/water mixture with a water fraction from 0% to 70% did not show a significant emission intensity change at 534 nm, which also supported that there is no contribution of the intermolecular process to the generation of the second emission (Figure 7C).

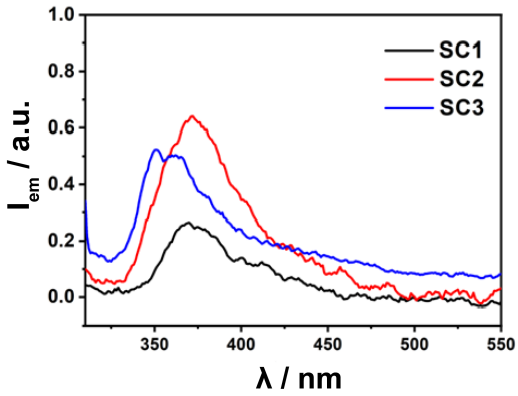

Figure 5. Photoluminescence spectra (λ_{ex} = 300 nm) of **SC1-SC3** in CH_3CN ($c = 10^{-5}$ M) at 300K.

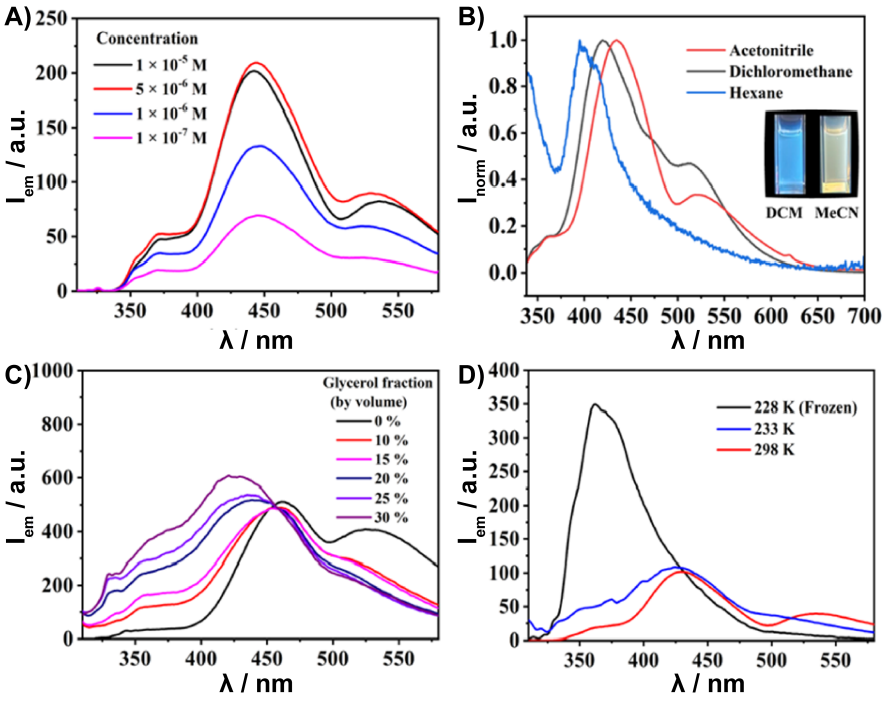

Figure 6. Photoluminescence spectra of **C4** in A) CH_3CN with different concentrations, B) 1.0×10^{-5} M different solvents. C) 1.0×10^{-5} M CH_3CN /water/glycerol mixtures with different glycerol fractions, and D) 1.0×10^{-5} M CH_3CN solution at different temperatures. Excitation wavelength λ_{ex} = 300 nm.

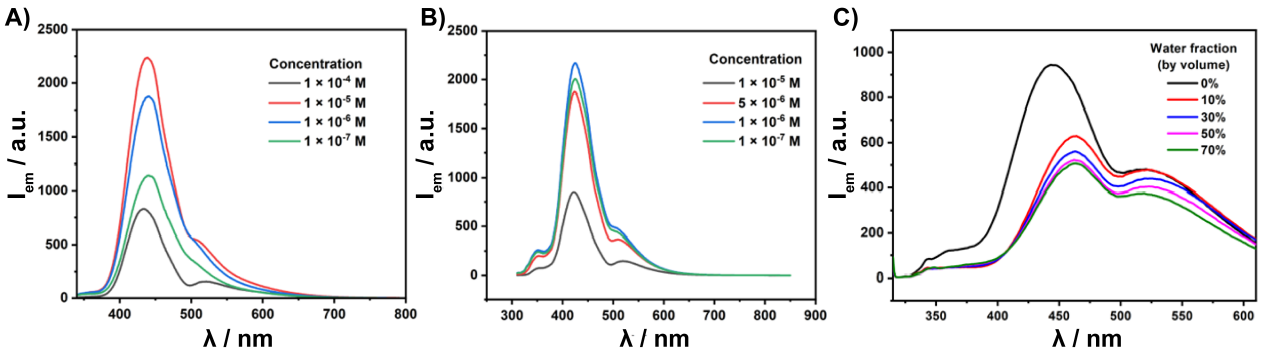

Figure 7. Photoluminescence spectra of A) **C2** and B) **C3** with different concentrations in CH_3CN and C) **C4** in a water/CH_3CN mixture (1.0×10^{-5} M, water fraction 0–70%).at room temperature ($\lambda_{ex.}$ = 300 nm).

These experimental results indicated the significant contribution of the intramolecular process. Considering this system's flexibility, especially at the connecting bond between sumanene and the phenyl ring, twisted intramolecular charge transfer (TICT) was the most likely reason to explain the phenomena. It is known that TICT is an electron transfer process that occurs upon photoexcitation in molecules that usually consist of a donor and acceptor part linked by a single bond. Following intramolecular twisting, the TICT state returns to the ground state through red-shifted emission. The emission properties are potentially environment dependent. In this context, the author next performed solvents, viscosity, and temperature-dependent emission property investigation (Figure 6B-D). The emission spectral envelop for **C1**-**C4** showed substantial solvatofluorochromism. With an increase in solvent polarity from hexane to CH_3CN, the emission peak gradually shifted to the lower energy (Figure 6B). Such a clear bathochromic shift was displayed by the emission colour change. This indicated the presence of the charge-transferred structures of **C1**-**C4** in the excited state. Furthermore, the emission spectra of **C4** in the CH_3CN/water/glycerol mixture showed a

significant decrease in the second emission intensity by the increment of the system viscosity with the generation of a new emission peak at 420 nm (Figure 6C). This was because of the restriction of the molecular rotation in a viscous media. Temperature-dependent measurement also indicated the contribution of intramolecular rotation to emerge the second emission (Figure 6D). When the temperature decreased to 228 K, the second emission disappeared, and only one intense peak remained. These results confirmed that the key to exhibiting the dual emission was the geometrical arrangement of the fluorophores controlled by the intramolecular rotation. The lifetime of **C3** and **C4** at their different emission maxima also supported the contribution of TICT (Figure 8). The analysis data showed that the lifetime of both longer wavelength emissions (511 nm for **C3**, 534 nm for **C4**) were shorter than those with shorter wavelength in each. In particular, the negative amplitudes of the fitting parameters for both of longer wavelength fluorescence lifetimes were cogent evidences for TICT (Table 2).[35, 36] Another important observation is that Ru complexed without a sumanene unit, as seen in **SC1**-**SC3,** did not show dual emission. The fact indicated that the rotation of the sumanene skeleton in the excited state of the complexes having phenylene tether triggered the exhibition of the second emission.

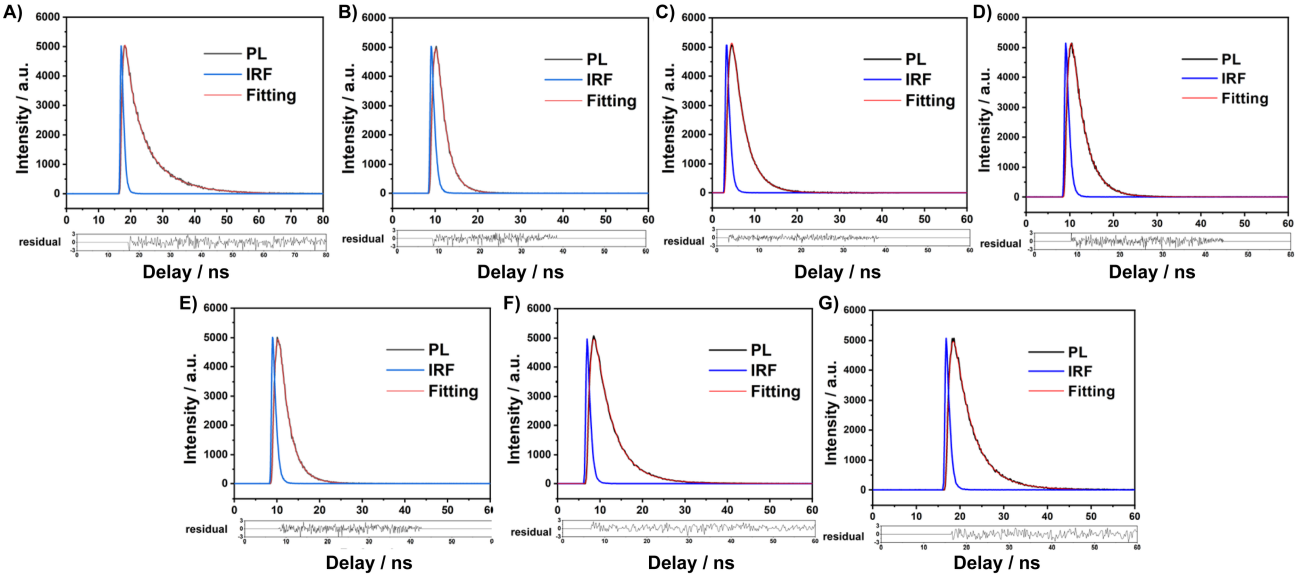

Figure 8. Time-resolved fluorescence emission A-D) λ_{em} = 420 nm for **C1-C4** and E-G) λ_{em} = 534 nm for **C3-C4** (10^{-4} M) in MeCN at 300 K under nitrogen. (λ_{ex} = 280 nm).

Table 2. Lifetime of **C1** to **C4** at different emission maxima.

complex	λ_{em} [nm]	τ [ns]	A_1	A_2	A'_1	A'_2	A'_3
C1	400	7.3	-	-	566.894	448.254	429.909
C2	430 515	3.8 3.2	673.468	29.1798	−928.279	517.818	201.204
C3	424 511	3.1 6.8	200.634	513.121	−1434.45	889.63	135.61
C4	434 534	3.2 7.5	84.238	476.555	−1505.83	1038.29	147.223

The fittings for **C2**, **C3** and **C4** at 430, 424 and 434 nm emission using second order equation (1), and fittings for **C1**, **C2**, **C3** and **C4** at 400, 515, 511 and 534 nm emission using third order equation (2).

$F_{it} = B + A_1 e^{-t/\tau_1} + A_2 e^{-t/\tau_2}$ (1); $F_{it} = B + A'_1 e^{-t/\tau_1} + A'_2 e^{-t/\tau_2} + A'_3 e^{-t/\tau_3}$ (2)

To obtain further information, the author calculated the ground state (S_0) and excited state (S_1) potential energy surfaces of **C3** and **C4** in CH_3CN by using DFT/TD-DFT method at PBE0/SDD-6-31G(d) level of theory. Optimisation results suggested that the dihedral angles of sumanene−terpyridine in both **C3** and **C4** were 45° at the S_0 state, whereas they

changed to 125° at the S_1 state. These results were further investigated by potential energy scans (Figure 9). In the calculation, the sumanene−terpyridine dihedral angles of both S_0 and S_1 structures were systematically fixed between 0 and 180 degrees, while other parts were relaxed. The calculation results showed two minima at both S_0 and S_1 states in each complex. The rotation energy barriers ΔE, here it is defined as the energy difference between the two minima, were much smaller in the excited state (**C3**: 0.63 kcal/mol, **C4**: 0.44 kcal/mol) than in the ground state (**C3**: 9.43 kcal/mol, **C4**: 7.67 kcal/mol). Relatively low rotation energy in S_1 probably allowed photo-induced structural change in the present systems.[37] MOs at the minimum energy states enabled a more detailed discussion about the mechanism (Figure 10). TD-DFT calculation revealed that the contributing orbitals for $S_1 \rightarrow S_0$ transitions were mainly HOMO and LUMO. In case of **C4**, LUMO of both S_0 and S_1 were delocalised onto the terpyridine-metal centre, while HOMOs were located on the sumanene skeleton at the S_0 state and on the terpyridylphenyl unit at the S_1 state. This means that an electron transfer from sumanene to the terpyridine-metal centre occurred while absorbing a photon, followed by a molecular twisting caused in the excitation process. The same tendency was confirmed in **C2** and **C3** while not in **C1** (Figure 10). This is explained by the molecular symmetry which affected by the phenyl linker. Indeed, the high molecular symmetry of **C1** exhibited a symmetrical HOMO distribution at S_0 state, while asymmetrical **C3**, **C4**, and phenyl bridged **C2** were not. However, the simulated TD-DFT data showed almost negligible effect of symmetrical HOMO distribution of **C1** to its absorption property. Meanwhile, the absence of phenyl linker caused the disappearance of the pass for the second emission, which was caused by the electron back transfer to the phenyl moiety from the terpyridine-metal centre. The much

small amount of HOMO distribution on phenyl moiety in the S_1 state of **C2** was probably reflected by the weaker intensity of the second emission compared with **C3** and **C4**. These results were consistent with the experimental observation, especially at low temperatures and highly viscous conditions in which the molecular motions were significantly suppressed to restrict the molecular twisting.

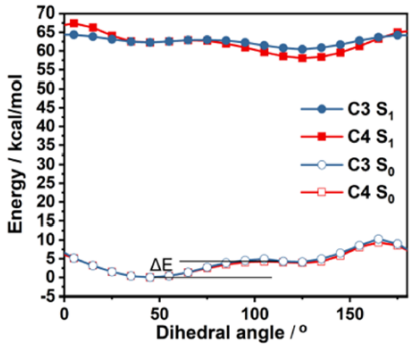

Figure 9. Potential energy scan of the S_0 and S_1 states of **C3** and **C4** versus sumanene and terpyridine dihedral angle in CH_3CN.

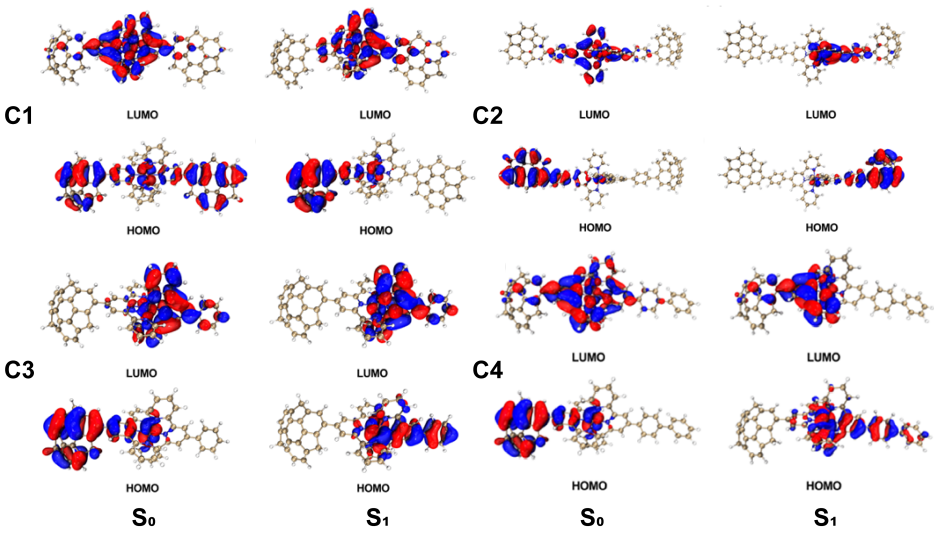

Figure 10. Molecular orbitals of **C1-C4** at S_0 and S_1 geometry.

Section 3. Cation sensing property

Finally, the author applied the recently reported cation trapping ability of sumanene for cation sensing via emission colour or intensity change. To achieve this, the author chose **C4** as the representative. The author checked the emission properties of 1:10 solutions of **C4** and various kinds of PF_6^- salts of alkali metals (in CH_3CN/water = 1:1 (v/v)) (Figure 11A). While no change in the emission intensity of **C4** was observed in cases of the addition of Na^+, K^+, Rb^+, and Cs^+, **C4** exclusively exhibited "turnoff" fluorescence behaviour in the addition of Li^+. Li^+ concentration-dependent experiment showed a gradual decrease of emission intensity when the Li^+ amount increased (Figure 11B). The same tendency was observed in the other three complexes (Figure 11C-D), indicating that the Li^+ sensing ability was attributable to sumanene core. Li^+ sensing abilities of **C1**-**C4** were evaluated by the Stern-Volmer plot based on the emission titration data (Table 2 and Figure 12A). The quenching process of **C4** was not a simple linear shape, indicating the presence of some acceleration effects for quenching in the high Li^+ concentration condition. The detection limit of Li^+ in CH_3CN/water for **C1**-**C4** are 160, 5,40 and 35 μM respectively (Figure 12B). In particular, **C2** exhibited a lower detection limit than the reported lithium-ion sensing materials.[38] Further analyses using Job's plot (Figure 12C) revealed the 1:8 binding mode for the di-sumanenyl complexes (**C1** and **C2**), whilst the 1:4 mode was found for the mono-sumanenyl complexes (**C3** and **C4**), indicating that four Li^+ were trapped in each sumanene core via the cation-p interaction, in which electrostatics play essential roles.

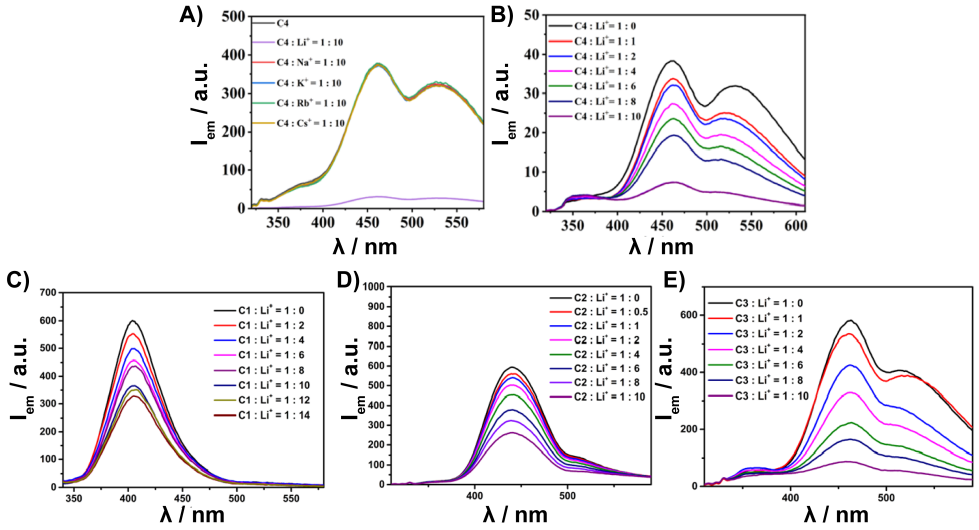

Figure 11. The cation sensing ability of **C1-C4**. A) Emission spectra of **C4**: alkali metal ions = 1:10 solutions (1.0×10^{-5} M in CH_3CN/water = 1:1, λ_{ex} = 300 nm). B-E) Emission spectra change of **C1-C4** by Li^+ titration (1.0×10^{-4} M in CH_3CN/water = 1:1, λ_{ex} = 300 nm)

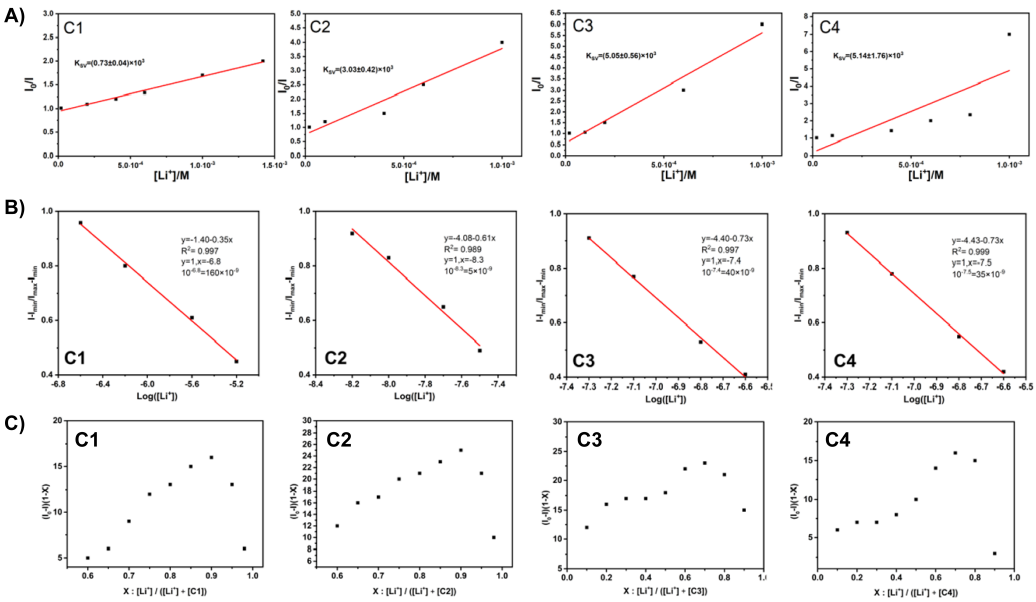

Figure 12. A) Stern-Volmer plots for the emission quenching of **C1-C4** by the addition of Li^+. B) Plot of $(I-I_{min})/(I_{max}-I_{min})$ vs Log ([Li^+]) for the calculation of detection limit of **C1-C4**. C) The Job's plot related to the interactions of the a) **C1**, b) **C2**, c) **C3** and d) **C4** with Li^+. All the data is based on the florescence spectra titration results. *x* stands for the molar fraction of

Li^+, I_0 stands for the emission intensity of **C1-C4** without Li^+ added, and I stands for the emission intensity of **C1-C4** with the given amount of Li^+ added.

In this context, the author attempted to find the trend of binding capacity by calculating the electrostatic potential of **C1-C4**. The results showed that the most electron-negative moieties were at the convex side of sumanene for all the complexes (Figure 13A). Thus, the structures of the complexes were hypothesised to be that the metal ion is bound to the convex side of the 6-membered ring of sumanene (Figure 13B). The differences in electron density on the sumanene skeleton of the complexes also explained the variations of the ion trapping ability. A comparison of the electron density on the convex side of the four compounds shows that C2 possesses the highest electron density. This can be attributed to the fact that the positively charged $[Ru(terpy)_2]^{2+}$ moiety is separated from the sumanene unit by a phenyl spacer, which significantly reduces the electronic influence of the $[Ru(terpy)_2]^{2+}$ center on the sumanene framework. This result well matched the experimental finding that **C2** exhibited the lowest detection limit. However, it should be considered that the electrostatic contribution is not the sole element for controlling the stability of the cation-π interaction. Previous computational studies have shown that cation–π interactions in buckybowls are strongly influenced by polarization rather than pure electrostatics. Energy decomposition analysis further confirms that Li^+, with its highest charge density, induces a markedly larger polarization of the curved π-surface of sumanene than Na^+ or K^+. Prior work consistently reports this enhanced inductive response for Li^+ in bowl-shaped systems. The molecular curvature amplifies polarization effects, making Li^+ uniquely capable of forming strongly stabilized complexes, whereas Na^+ and K^+ lack sufficient field strength to polarize the π-cloud

to a comparable extent.[28] This might explain why only Li^+ could be adsorbed in such electropositive complexes.

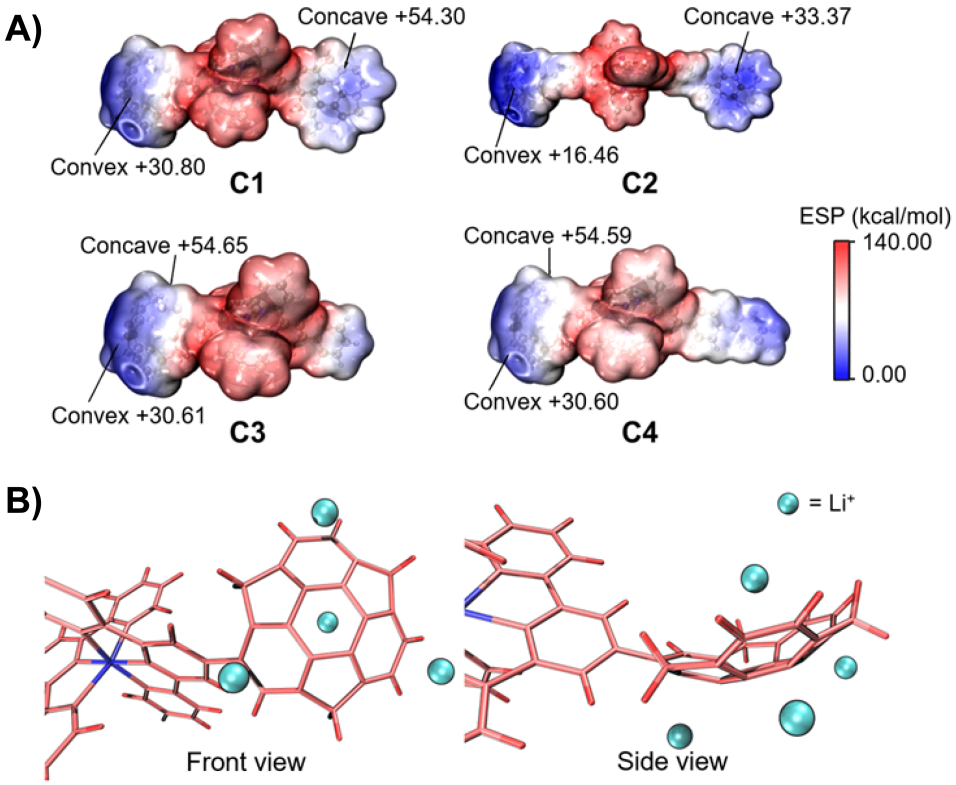

Figure 13. A) ESP plots on **C1**-**C4**. B) Schematic model of Li^+ binding on sumanene skeleton of **C4**.

Section 4. Summary

The author reported sumanene-ligated four Ru(II)-terpyridine complexes **C1**-**C4**. All the complexes showed higher emission ability than the conventional terpyridylphenyl complexes by excitation at ligand-centred π–π* band. Especially the ones containing phenylene tether parts exhibited the dual emission caused by the TICT, which was caused by a quick intramolecular rotation due to the low rotation barrier of sumanene and next terpyridine in the

excited state. The cation recognition experiments also revealed the susceptible Li^+ trapping ability of the complexes at the sumanene cores. the author's findings will contribute to the further understanding the bowl-shape effect for the curved-π based emissive materials. They will also extend the applicability of sumanene-based sensing materials.

Experimental section

Instrumentations and chemicals

All the chemical reagents and solvents were commercially purchased and purified according to the standard methods, if necessary. Air- and moisture-sensitive reactions were carried out using commercially available anhydrous solvents under inert atmosphere of nitrogen. Unless otherwise noted. ^{1}H and ^{13}C NMR spectra were recorded on a JEOL JNM-ECS400 NMR spectrometer (^{1}H: 400 MHz and ^{13}C: 100 MHz). Chemical shift (δ) are expressed relative to the resonances of the residual non-deuterated solvent for ^{1}H ($CDCl_3$: $^{1}H(\delta)$ = 7.26 ppm) and for ^{13}C ($CDCl_3$: $^{13}C(\delta)$ = 77.0 ppm). High resolution mass spectra (HRMS) were measured using electron impact (EI) methods on JEOL JMS-777V spectrometer. Matrix-assisted laser desorption/ionization coupled to time-of-flight (MALDI-TOF) mass spectra were measured on Bruker Autoflex III spectrometer. The preparative TLC (PTLC) purification was conducted using Wako gel B-5F PTLC plates. Flash column chromatography was prepared using Kanto Silica gel 60N (neutral, spherical, 40-50 μm) and performed with a Yamazen preparative medium pressure liquid chromatography system. UV-vis spectra were recorded on a JASCO V-670 spectrophotometer. Steady-state emission spectra were recorded on a JASCO FP-6500DS spectrometer. Lifetime measurements were recorded on a HAMAMATSU C11347-01 spectrometer with an integrating sphere. Elemental analyses were measured on a J-Science Micro corder JM10 at the Analysis Center in Osaka University.

Evaluation of Quantum Yield

A relative value of quantum yield was obtained by following relationship with using the

corrected spectra data JASCO Spectra Manager™.

$$\Phi_u = \Phi_{st} \cdot \left(\frac{F_u}{F_{st}}\right) \cdot \left(\frac{A_{st}}{A_u}\right) \cdot \left(\frac{D_u}{D_{st}}\right) \cdot \left(\frac{I_{ex,st}}{I_{ex,u}}\right) \cdot \left(\frac{{n_u}^2}{{n_{st}}^2}\right)$$

Here, is the fluorescence quantum yield for the standard sample; F_u and F_{st} are the integrated values for the emission spectra of the unknown and standard samples; A_{st} and A_u are the absorbance at the excitation wavelength of the standard and unknown samples; $I_{ex,st}$ and $I_{ex,u}$ are the intensities of the excitation light at the excitation wavelengths for the standard and unknown samples; and n_u and n_{st} are the average refractive indexes for the emission spectra measurement range for the standard and unknown samples.

In this measurement, quinine sulfate in 0.5 M H_2SO_4 was used as the standard (λ_{ex} = 310 nm, Φ = 0.55).[S4] Sample concentrations were low enough (less than 10% absorption across the spectrum) and the same sample solutions were used in both absorption and emission spectra measurements. Also, $I_{ex,st}/I_{ex,u}$ was corrected automatically in the software and considered to be 1.0. Therefore the above equation becomes:

$$\Phi_u = \Phi_{st} \cdot \left(\frac{F_u}{F_{st}}\right) \cdot \left(\frac{A_{st}}{A_u}\right) \cdot \left(\frac{{n_u}^2}{{n_{st}}^2}\right)$$

The obtained parameters for the calculation of Φ_u are shown below table.

Table 3. The parameter used to calculate quantum yields using quinine sulfate as a standard.

	F_u	A_u	n_u	F_{st}	A_{st}	n_{st}
C1	1472	0.08				
C2	5933	0.06	1.34[S5]	63255	0.05	1.33[S5]
C3	9085	0.05	(CH_3CN)			(water)
C4	11592	0.06				

Stern-Volmer plots

The effectiveness of **C1**-**C4** for Li^+ trapping were evaluated from emission titration data using the following Stern-Volmer equation,

$$\frac{I_0}{I} = 1 + K_{SV} \cdot [\mathrm{Q}]$$

where I_0 and I are emission intensity of complexes in the absence and presence of Li^+ and [Q] is the concentration of Li^+. K_{sv} is the Stern-Volmer constant of the complex of the present system which is represented by the equation,

$$K_{sv} = \tau_0 k_q$$

where τ_0 is the life time of the complex without Li^+ and k_q is the rate of the emission quenching process.

Computational experiments

All the theoretical calculations were conducted by Gaussian 16.[39] The ground state structure optimizations were performed at the PBE0 functional and 6-311G(d) basis set for C, H, N, and O and SDD basis set for Ru. Simulation of UV-vis spectra, and excited state (S_1 and T_1) optimizations were performed by TD-DFT (time-dependent density functional theory) using the optimized coordinates at the PBE0 functional and 6-311G(d) basis set for C, H, N, and O and SDD basis set for Ru. Multiwfn 3.8 was used to analyze the wave functions.[40]

Synthetic procedure and characterization data

4'-(4,7-dihydro-1H-tricyclopenta[def,jkl,pqr]triphenylen-2-yl)-2,2':6',2''-terpyridine (**L1**)

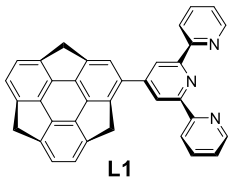

L1

To a solution of NaOH (100.0 mg, 2.40 mmol) in EtOH (10 mL), **2** (40.0 mg, 0.14 mmol)[S1] and 2-acetylpyridine (17.0 mg, 0.30 mmol) was added. After stirring at room temperature for 24 h, aqueous NH_3 (28%, 2 mL) was added. The resulting mixture was refluxed for 16 h. After cooling to room temperature, the solid was collected by suction filtration and was washed with MeOH to give the product **L1** as a pale-yellow solid (52.5 mg, 0.11 mmol, 79%).

L1: mp: 287 °C; ^{1}H NMR (400 MHz, $CDCl_3$) δ (ppm) 8.73 (s, 2H), 8.72 (d, 2H), 8.67 (d, J = 7.9 Hz, 2H), 7.87 (td, J = 7.7, 1.8 Hz, 2H), 7.73 (s, 1H), 7.34 (ddd, J = 7.6, 4.8, 1.2 Hz, 2H), 7.17–7.04 (m, 4H), 5.17 (d, J = 19.8 Hz, 1H), 4.80 (d, J = 19.5 Hz, 1H), 4.72 (d, J = 19.5 Hz, 1H), 3.59 (d, J = 19.5 Hz, 1H), 3.49 (d, J = 19.5 Hz, 1H), 3.44 (d, J = 19.5 Hz, 1H). ^{13}C NMR (100 MHz, $CDCl_3$) δ 156.60, 155.96, 150.18, 150.02, 149.90, 149.36, 149.12, 148.98, 148.81, 148.64, 148.58, 137.00, 123.95, 123.55, 123.89, 123.78, 123.30, 122.92, 121.49, 120.34, 51.51, 43.52, 41.97. HRMS (EI) *m*/*z* Calcd. for $C_{36}H_{21}N_3$ $[M]^+$: 495.1735. Found: 495.1787.

4'-(4-(4,7-dihydro-1H-tricyclopenta[def,jkl,pqr] triphenylen-2-yl)phenyl)-2,2':6',2''-terpyridine (**L2**)

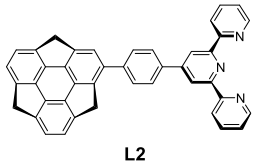

L2

An aqueous solution of K_2CO_3 (1.0 M, 0.16 mL, 0.16 mmol) was added to a THF solution (5 mL) of a mixture of **4** (13.7 mg, 0.040 mmol) **3** (17.6 mg, 0.050 mmol), and Pd $(PPh_3)_4$ (14.0 mg, 0.005 mmol) under N_2 at 25 °C. After stirring at 70 °C for 20 h, the reaction mixture was cooled to room temperature and was extracted with

chloroform (3 × 10mL). The combined organic layer was washed with brine, dried over anhydrous Na_2SO_4, filtered and then concentrated in vacuo. The crude product was then purified by column chromatography on neutral alumina gel with $CHCl_3$ to afford **L2** as a pale-yellow powder (16.7 mg, 0.029 mmol, 73%).

L2: mp: 252 °C (dec.); ^{1}H NMR (400 MHz, $CDCl_3$) δ (ppm) 8.79 (s, 2H), 8.74 (d, J = 4.4 Hz, 2H), 8.69 (d, J = 8.1 Hz, 2H), 7.99 (d, J = 8.1 Hz, 2H), 7.89 (t, J = 7.5 Hz, 2H), 7.72 (d, J = 8.2 Hz, 2H), 7.44 (s, 1H), 7.36 (t, J = 7.5 Hz, 2H), 7.16–7.05 (m, 4H), 4.96 (d, J = 19.8 Hz, 1H), 4.80 (d, J = 19.2 Hz, 1H), 4.72 (d, J = 19.7 Hz, 1H), 3.55 (d, J = 19.3 Hz, 1H), 3.43 (d, J = 17.0 Hz, 1H), 3.38 (d, J = 17.0 Hz, 1H). ^{13}C NMR (100 MHz, $CDCl_3$) δ 156.35, 156.07, 150.18, 149.88, 149.25, 149.15, 149.06, 148.88, 148.74, 148.52, 146.46, 141.61, 137.59, 137.27, 137.01, 132.25, 132.15, 129.12, 128.72, 128.55, 127.69, 123.96, 123.60, 123.51, 123.46, 123.28, 122.74, 121.48, 118.81, 42.67, 41.97, 41.86. HRMS (EI) *m*/*z* Calcd. for $C_{42}H_{25}N_3$ $[M]^+$: 571.2048. Found: 571.2050.

4'-phenyl-2,2':6',2''-terpyridine (**SL1**)

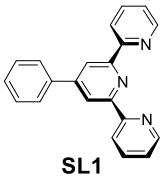

SL1

To a solution of NaOH (0.96 g, 24.00 mmol) in EtOH (20 mL), benzaldehyde (0.60 g, 4.40 mmol) and 2-acetylpyridine (1.06 g, 8.80 mmol) was added. After stirring at room temperature for 24 h, aqueous NH_3•H_2O (28%, 3 mL) was added. The resulting mixture was refluxed for 20 h and was cooled to room temperature. The solid so formed was collected by suction filtration and was washed with EtOH and $CHCl_3$ to give the product **SL1** as a white solid (1.21 g, 3.92 mmol, 89%).

SL1: mp: 189 °C (dec.); ^{1}H NMR (400 MHz, Chloroform-*d*) δ 8.80 (s, 2H), 8.76 (d, J = 4.4 Hz, 2H), 8.71 (d, J = 8.0 Hz, 2H), 7.98–7.91 (m, 4H), 7.52 (t, J = 7.4 Hz, 2H), 7.48–7.38 (m, 3H). HRMS (EI) m/z Calcd. for $C_{21}H_{15}N_3$ $[M^+]$: 309.1266. Found: 309.1215.

4'-([1,1'-biphenyl]-4-yl)-2,2':6',2''-terpyridine (**SL2**)

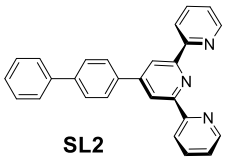

An aqueous solution of K_2CO_3 (1.0 M, 0.4 mL, 0.40 mmol) was added to a THF solution (10 mL) of a mixture of Bromobenzene (15.5 mg, 0.10 mmol), **3** (35.3 mg, 0.10 mmol), and Pd (PPh3)4 (30.0 mg, 0.01 mmol) under N_2 at 25 °C. After stirring at 70 °C for 24 h. After cooling to room temperature, the mixture was extracted with chloroform. The combined organic layer was washed with brine, dried over anhydrous Na_2SO_4, and then concentrated in vacuo, the crude product was purified by column chromatography on neutral alumina gel with $CHCl_3$ to afford the product **SL2** as a pale-yellow powder (25.0 mg, 0.065 mmol, 65%).

SL2: mp: 206 °C (dec.); ^{1}H NMR (400 MHz, Chloroform-*d*) δ 8.84 (s, 2H), 8.77 (d, *J* = 4.8 Hz, 2H), 8.72 (d, *J* = 8.1 Hz, 2H), 8.04 (d, *J* = 7.9 Hz, 2H), 7.93 (t, *J* = 7.7 Hz, 2H), 7.76 (d, *J* = 7.9 Hz, 2H), 7.69 (d, *J* = 7.4 Hz, 2H), 7.49 (t, *J* = 7.5 Hz, 2H), 7.42 – 7.36 (m, 3H). HRMS (EI) m/z Calcd. for $C_{27}H_{19}N_3$ [M^+]: 385.1579. Found: 385.1587.

4'-([1,1':4',1''-terphenyl]-4-yl)-2,2':6',2''-terpyridine (**SL3**)

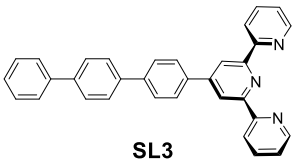

An aqueous solution of K_2CO_3 (1.0 M, 0.4 mL, 0.40 mmol) was added to a THF solution (10 mL) of a mixture of 4-bromobiphenyl (23.3 mg, 0.10 mmol), **3** (35.3 mg, 0.10 mmol), and Pd (PPh_3)$_4$ (30.0 mg, 0.01 mmol) under N_2 at 25 °C. After stirring at 70 °C for 24 h. After cooling to room temperature, the mixture was extracted with chloroform. The combined organic layer was washed with brine, dried over anhydrous Na_2SO_4, and then concentrated in vacuo, the crude product was purified by column chromatography on neutral alumina gel with $CHCl_3$ to afford the product **SL3** as a pale-yellow powder (31.3 mg, 0.068 mmol, 68%).

SL3: mp: 271 °C (dec.); ^{1}H NMR (600 MHz, Chloroform-*d*) δ 8.89 (s, 2H), 8.79 (d, *J* = 4.9 Hz, 2H), 8.75 (d, *J* = 8.0 Hz, 2H), 8.08 (d, *J* = 8.0 Hz, 2H), 7.97 (t, *J* = 7.8 Hz, 2H), 7.82 (d, *J* = 8.3 Hz, 2H), 7.77 (d, *J* = 8.3 Hz, 2H), 7.72 (d, *J* = 8.3 Hz, 2H), 7.67 (d, *J* = 7.2 Hz, 2H), 7.48 (t, *J* = 7.7 Hz, 2H), 7.43 (t, *J* = 6.2 Hz, 2H), 7.38 (t, *J* = 7.4 Hz, 1H). HRMS (EI) m/z Calcd. for $C_{33}H_{23}N_3$ [M^+]: 416.1892. Found: 416.1823.

[Ru (L1)$_2$](PF$_6$)$_2$ (C1)

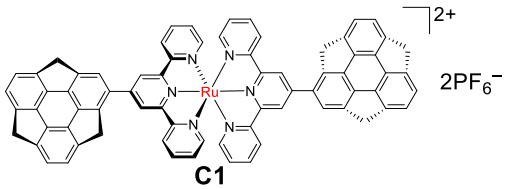

L1 (20.0 mg, 0.04 mmol) was dissolved in EtOH/$CHCl_3$ (10 mL, v/v=1:1) and the mixture was degassed by N_2 bubbling (10 min). $RuCl_2(DMSO)_4$ (9.7mg, 0.02 mmol) was added and the suspension was heated to 80 °C for 24 hours. The deep red solution was allowed to cool and NH_4PF_6 (40.0 mg, 0.24 mmol) was added. A red solid immediately precipitated which was collected by filtration and subsequently washed with water (3×10 mL) and MeOH (3×10 mL, to aid drying). The solid material was washed down with acetonitrile. The solvent was removed in vacuo to yield the complex **C1** as red solid (22.1 mg, 0.016 mmol, 80%).

C1: mp: 371 °C (dec.); ^{1}H NMR (400 MHz, Acetonitrile-d_3) δ 8.96 (s, 4H), 8.60 (d, *J* = 9.1 Hz, 4H), 7.99 (s, 2H), 7.94 (td, *J* = 7.9, 1.5 Hz, 4H), 7.44 (d, *J* = 4.3 Hz, 4H), 7.34 – 7.22 (m, 8H), 7.19 (ddd, *J* = 7.1, 5.6, 1.3 Hz, 4H), 5.40 (d, *J* = 19.9 Hz, 2H), 4.96 (d, *J* = 19.9 Hz, 2H), 4.79 (d, *J* = 19.9 Hz, 2H), 3.83 (d, *J* = 15.4 Hz, 2H), 3.78 (d, *J* = 15.5 Hz, 2H), 3.59 (d, *J* = 20.0 Hz, 2H). MALDI-TOF MS (*m*/*z*): Calcd. for [$C_{72}H_{42}N_6Ru$]$^+$: 1092.25. Found: 1092.48. Anal. Calcd for $C_{72}H_{42}N_6RuF_{12}P_2$: C, 62.57; H, 3.06; N, 6.08. Found: C, 62.74; H, 3.01; N, 6.17.

[Ru (L2)$_2$](PF$_6$)$_2$ (C2)

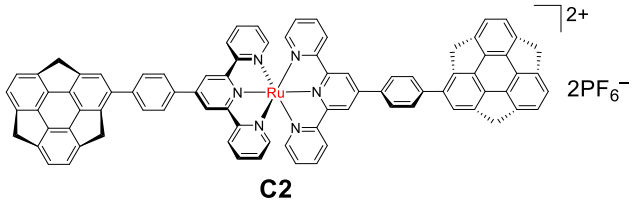

C2

L2 (15.0 mg, 0.026 mmol) was dissolved in EtOH/$CHCl_3$ (10 mL, v/v=1:1) and the mixture was degassed by N_2 bubbling (10 min). $RuCl_2(DMSO)_4$ (6.3 mg, 0.013 mmol) was added and the suspension was heated to 80 °C for 24 hours. The deep red solution was allowed to cool and NH_4PF_6 (25.4 mg, 0.16mmol) was added. A red solid immediately precipitated which was collected by filtration and subsequently washed with water (3×10 mL) and MeOH (3×10 mL, to aid drying). The solid material was washed down with acetonitrile. The solvent was removed in vacuo to yield the complex **C2** as red solid (16.8 mg, 0.011 mmol, 85%).

C2: mp: 335 °C (dec.); ^{1}H NMR (400 MHz, Acetonitrile-d_3) δ 9.09 (s, 4H), 8.69 (d, J = 7.8 Hz, 4H), 8.34 (d, J = 6.7 Hz, 4H), 8.05 (d, J = 7.1 Hz, 4H), 7.96 (t, J = 7.9 Hz, 4H), 7.66 (s, 2H), 7.46 (d, J = 5.6 Hz, 4H), 7.26 – 7.14 (m, 12H), 5.13 (d, J = 19.6 Hz, 2H), 4.85 (d, J = 19.6 Hz, 2H), 4.75 (d, J = 20.0 Hz, 2H), 3.69 (d, J = 19.7 Hz, 2H), 3.54 (d, J = 18.8 Hz, 2H), 3.50 (d, J = 18.4 Hz, 2H). MALDI-TOF MS (*m*/*z*): Calcd. for $[C_{84}H_{50}N_6Ru]^+$: 1244.31. Found: 1244.40. Anal. Calcd for $C_{84}H_{50}N_6RuF_{12}P_2$: C, 65.76; H, 3.28; N, 5.48. Found: C, 65.91; H,3.21; N, 5.57.

[Ru (L1) (SL1)](PF6)$_2$ (C3)

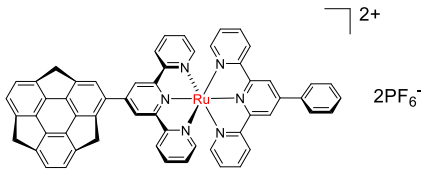

C3

To a solution of **SL1** (50.0 mg, 0.16 mmol) and $RuCl_3$•$3H_2O$ (33.1 mg, 0.16 mmol) in $CHCl_3$ (5mL) and EtOH (5 mL). The mixture was stirred at 80 °C for 24 h. After cooling to ambient temperature, the precipitates were filtered and washed with MeOH to afford **5** (67.7 mg, 0.13 mmol, 82%). After evaporated to dryness under vacuum, it was applied to the synthesis of **C3** directly. To a flask containing a mixture of **5** (10.0 mg, 0.019 mmol) and **L1** (9.6 mg, 0.019 mmol), MeOH (4 mL),

$CHCl_3$ (4 mL), and N-ethylmorpholine (6.5 mg, 0.057 mmol) were added. The mixture was stirred at 80 °C for 24 h. After cooling to ambient temperature, the solvent was evaporated in vacuo and the residue was purified by column chromatography (Al_2O_3), eluting with a mixture of MeOH and CH_2Cl_2. The complex was counterion exchanged with NH_4PF_6 (18.5 mg, 0.114 mmol) to give **C3**, as a red precipitate (14.4 mg, 0.012 mmol, 65%).

C3: mp: 355 °C (dec.); ^{1}H NMR (400 MHz, Acetonitrile-d_3) δ 8.99 (s, 2H), 8.93 (s, 2H), 8.62 (d, J = 7.8 Hz, 2H), 8.58 (d, J = 8.1 Hz, 2H), 8.18 (d, J = 7.3 Hz, 2H), 7.96 (s, 1H), 7.94 – 7.88 (m, 4H), 7.74 (t, J = 7.6 Hz, 2H), 7.66 (t, J = 7.3 Hz, 1H), 7.42 (d, J = 4.1 Hz, 2H), 7.41 (d, J = 4.3 Hz, 2H), 7.29 – 7.12 (m, 8H), 5.37 (d, J = 20.1 Hz, 1H), 4.92 (d, J = 19.4 Hz, 1H), 4.76 (d, J = 20.1 Hz, 1H), 3.81 (d, J = 17.6 Hz, 1H), 3.76 (d, J = 17.1 Hz, 1H), 3.55 (d, J = 20.0 Hz, 1H). MALDI-TOF MS (m/z): Calcd. for $[C_{57}H_{36}N_6Ru]^+$: 906.20. Found: 906.06. Anal. Calcd for $C_{57}H_{36}N_6RuF_{12}P_2$: C, 57.25; H, 3.03; N, 7.03. Found: C, 57.41; H, 3.01; N, 7.09.

[Ru (L1) (SL2)] $(PF6)_2$ (C4)

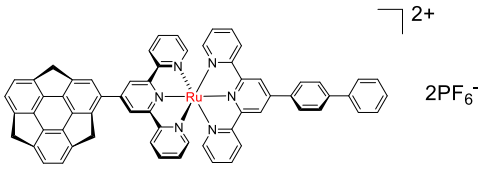

C4

To a solution of **SL2** (30.8 mg, 0.080 mmol) and $RuCl_3$•$3H_2O$ (16.6 mg, 0.080 mmol) in $CHCl_3$ (5mL) and EtOH (5 mL). The mixture was stirred at 80 °C for 24 h. After cooling to ambient temperature, the precipitates were filtered and washed with MeOH to afford **6** (33.8 mg, 0.066 mmol, 82%).[S3] After dryness under vacuum, it was applied to the synthesis of **C4** directly. To a flask containing a mixture of **6** (11.2 mg, 0.019 mmol) and **L1** (9.6 mg, 0.019 mmol), MeOH (4 mL), $CHCl_3$ (4 mL), and N-ethylmorpholine (6.5 mg, 0.057 mmol) were added. The mixture was stirred at 80 °C for 24 h. After cooling to ambient temperature, the solvent was evaporated in vacuo

and the residue was purified by column chromatography (Al_2O_3), eluting with a mixture of MeOH and CH_2Cl_2. The complex was counterion exchanged with NH_4PF_6 (18.5 mg, 0.114 mmol) to give **C4**, as a red precipitate (17.8 mg, 0.014 mmol, 71%).

C4: mp: 296 °C (dec.); ^{1}H NMR (400 MHz, Acetonitrile-d_3) δ 9.05 (s, 2H), 8.94 (s, 2H), 8.65 (d, J = 7.7 Hz, 2H), 8.58 (d, J = 8.0 Hz, 2H), 8.30 (d, J = 7.9 Hz, 2H), 8.03 (d, J = 8.1 Hz, 2H), 7.97 – 7.90 (m, 4H), 7.83 (d, J = 7.4 Hz, 2H), 7.56 (t, J = 7.7 Hz, 2H), 7.47 (t, J = 7.0 Hz, 1H), 7.42 (d, J = 4.3 Hz, 4H), 7.31 – 7.21 (m, 4H), 7.14 - 7.18 (m, 4H), 5.37 (d, J = 20.2 Hz, 1H), 4.93 (d, J = 19.9 Hz, 1H), 4.77 (d, J = 20.5 Hz, 1H), 3.81 (d, J = 15.8 Hz, 1H), 3.75 (d, J = 15.8 Hz, 1H), 3.56 (d, J = 19.8 Hz, 1H). MALDI-TOF MS (m/z): Calcd. for $[C_{63}H_{40}N_6Ru]^+$: 982.23. Found: 982.22. Anal. Calcd for $C_{63}H_{40}N_6RuF_{12}P_6$: C, 59.49; H, 3.17; N, 6.61. Found: C, 59.55; H, 3.14; N, 6.68.

[Ru(SL1)$_2$](PF6)$_2$ (SC1)

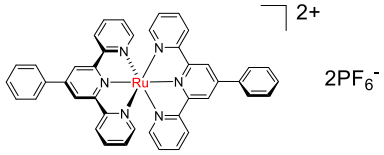

SC1

SL1 (8.0 mg, 0.026 mmol) was dissolved in EtOH/$CHCl_3$ (10 mL, v/v=1:1) and the mixture was degassed by N_2 bubbling (10 min). $RuCl_2(DMSO)_4$ (6.3 mg, 0.013 mmol) was added and the suspension was heated to 80 °C for 24 hours. The deep red solution was allowed to cool and NH_4PF_6 (25.4 mg, 0.16mmol) was added. A red solid immediately precipitated which was collected by filtration and subsequently washed with water (3×5 mL) and MeOH (3×5 mL, to aid drying). The solid material was washed down with acetonitrile. The solvent was removed in vacuo to yield the complex **SC2** as red solid (11.8 mg, 0.012 mmol, 90%).

SC1: mp: 216 °C (dec.); ^{1}H NMR (400 MHz, Acetonitrile-d_3) δ 9.02 (s, 4H), 8.66 (d, J = 8.1 Hz, 4H), 8.22 (d, J = 7.6 Hz, 4H), 7.95 (t, J = 7.9 Hz, 4H), 7.78 (t, J = 7.5 Hz, 5H), 7.70 (t, J = 7.2 Hz, 2H), 7.45 (d, J = 5.5 Hz, 4H), 7.19 (t, J = 6.7 Hz, 4H). MALDI-TOF MS (m/z): Calcd. for $[C_{42}H_{30}N_6Ru]^+$:

720.16. Found: 720.18.

[Ru(SL1)(SL2)](PF6)$_2$ (SC2)

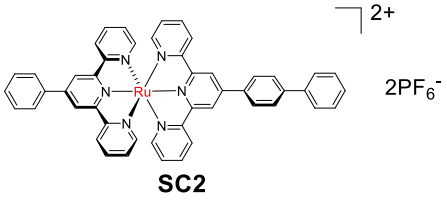

SC2

To a flask containing a mixture of **5** (10.0 mg, 0.019 mmol) and **SL2** (8.1 mg, 0.019 mmol), MeOH (4 mL), $CHCl_3$ (4 mL), and N-ethylmorpholine (6.5 mg, 0.057 mmol) were added. The mixture was stirred at 80 °C for 24 h. After cooling to ambient temperature, the solvent was evaporated in vacuo and the residue was purified by column chromatography (Al_2O_3), eluting with a mixture of MeOH and CH_2Cl_2. The complex was counterion exchanged with NH_4PF_6 (18.5 mg, 0.114 mmol) to give **SC2**, as a red precipitate (16.9 mg, 0.015 mmol, 82%).

SC2: mp: 233 °C (dec.); ^{1}H NMR (400 MHz, Acetonitrile-d_3) δ 9.07 (s, 2H), 9.02 (s, 2H), 8.68 (d, J = 9.8 Hz, 2H), 8.65 (d, J = 9.2 Hz, 2H), 8.32 (d, J = 8.0 Hz, 2H), 8.21 (d, J = 7.6 Hz, 2H), 8.06 (d, J = 7.8 Hz, 2H), 7.96 (t, J = 8.0 Hz, 4H), 7.86 (d, J = 7.6 Hz, 2H), 7.78 (t, J = 7.8 Hz, 2H), 7.69 (t, J = 7.7 Hz, 1H), 7.59 (t, J = 8.1 Hz, 2H), 7.51 (t, J = 7.7 Hz, 1H), 7.44 -7.46 (m, 4H), 7.19 (t, J = 8.0 Hz, 4H). MALDI-TOF MS (m/z): Calcd. for $[C_{48}H_{34}N_6Ru]^+$: 796.19. Found: 796.22.

[Ru(SL1) (SL3)](PF6)$_2$ (SC3)

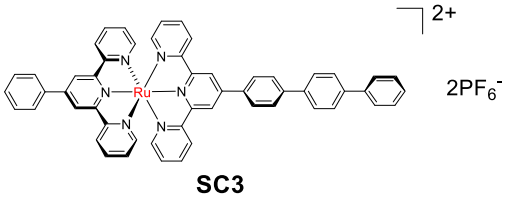

SC3

To a flask containing a mixture of **5** (10.0 mg, 0.019 mmol) and **SL3** (8.8 mg, 0.019 mmol), MeOH (4 mL), $CHCl_3$ (4 mL), and N-ethylmorpholine (6.5 mg, 0.057 mmol) were added. The mixture was stirred at 80 °C for 24 h. After cooling to ambient temperature, the solvent was evaporated in vacuo and the residue was purified by column chromatography (Al_2O_3), eluting

with a mixture of MeOH and CH_2Cl_2. The complex was counterion exchanged with NH_4PF_6 (18.5 mg, 0.114 mmol) to give **SC3**, as a red precipitate (17.9 mg, 0.015 mmol, 81%).

SC3: mp: 302 °C (dec.); ^{1}H NMR (400 MHz, Acetonitrile-d_3) δ 9.09 (s, 2H), 9.03 (s, 2H), 8.69 (d, *J* = 8.0 Hz, 2H), 8.66 (d, *J* = 8.2 Hz, 2H), 8.35 (d, *J* = 8.4 Hz, 2H), 8.22 (d, *J* = 7.4 Hz, 2H), 8.13 (d, *J* = 8.4 Hz, 2H), 7.98 (d, *J* = 7.2 Hz, 2H), 7.97 (t, *J* = 6.5 Hz, 4H), 7.87 (d, *J* = 8.3 Hz, 2H), 7.78 (d, *J* = 7.6 Hz, 2H), 7.77 (d, *J* = 7.6 Hz, 2H), 7.70 (t, *J* = 7.4 Hz, 1H), 7.54 (t, *J* = 7.6 Hz, 2H), 7.47 (d, *J* = 4.9 Hz, 2H), 7.45 (d, *J* = 4.9 Hz, 2H), 7.44 (t, *J* = 4.8 Hz, 1H), 7.20 (t, *J* = 6.6 Hz, 4H). MALDI-TOF MS (m/z): Calcd. for $[C_{54}H_{38}N_6Ru]^+$: 872.22. Found: 872.48.

^{1}H NMR and ^{13}C NMR charts of **L1**

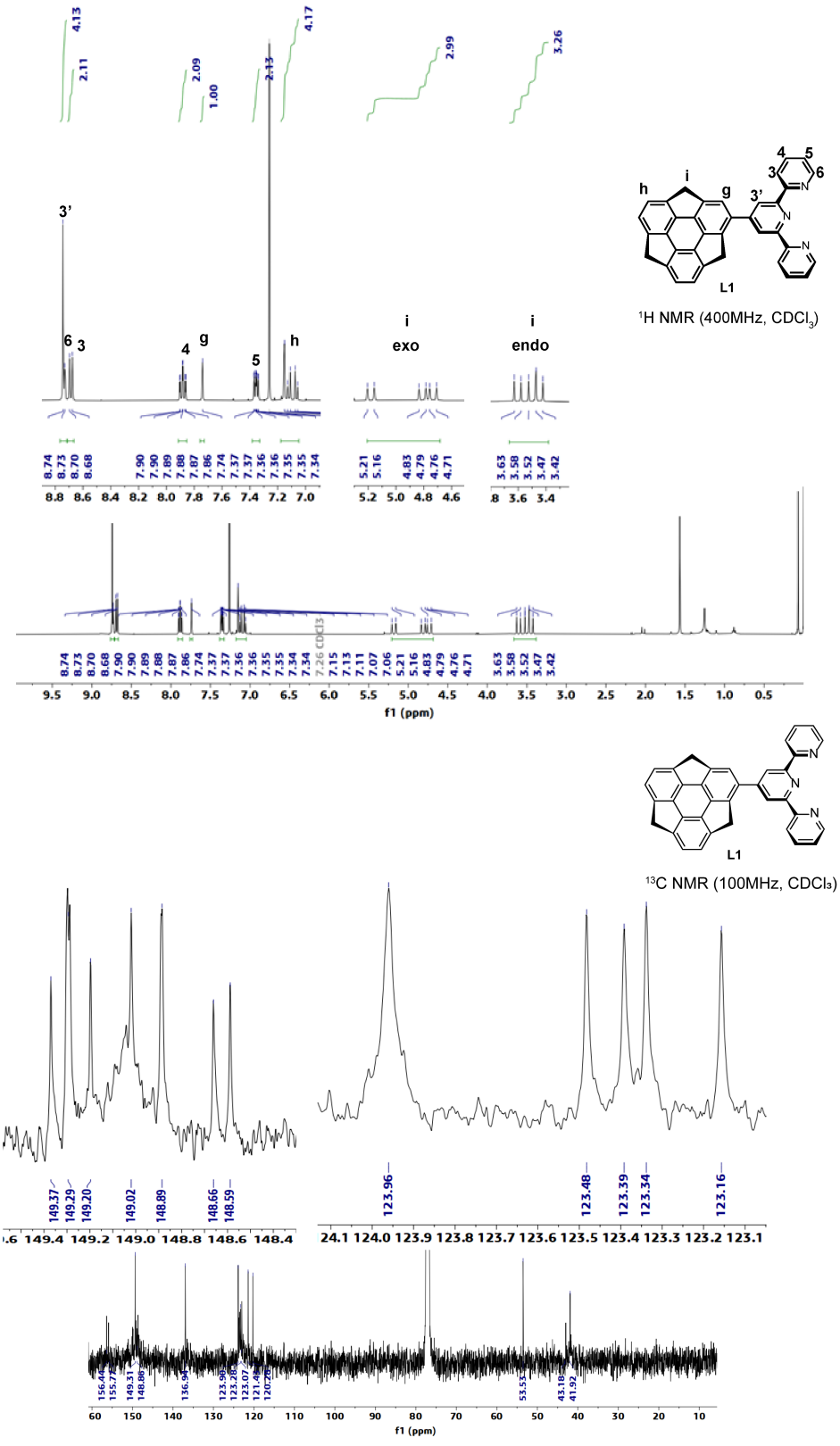

^{1}H NMR and ^{13}C NMR charts of **L2**

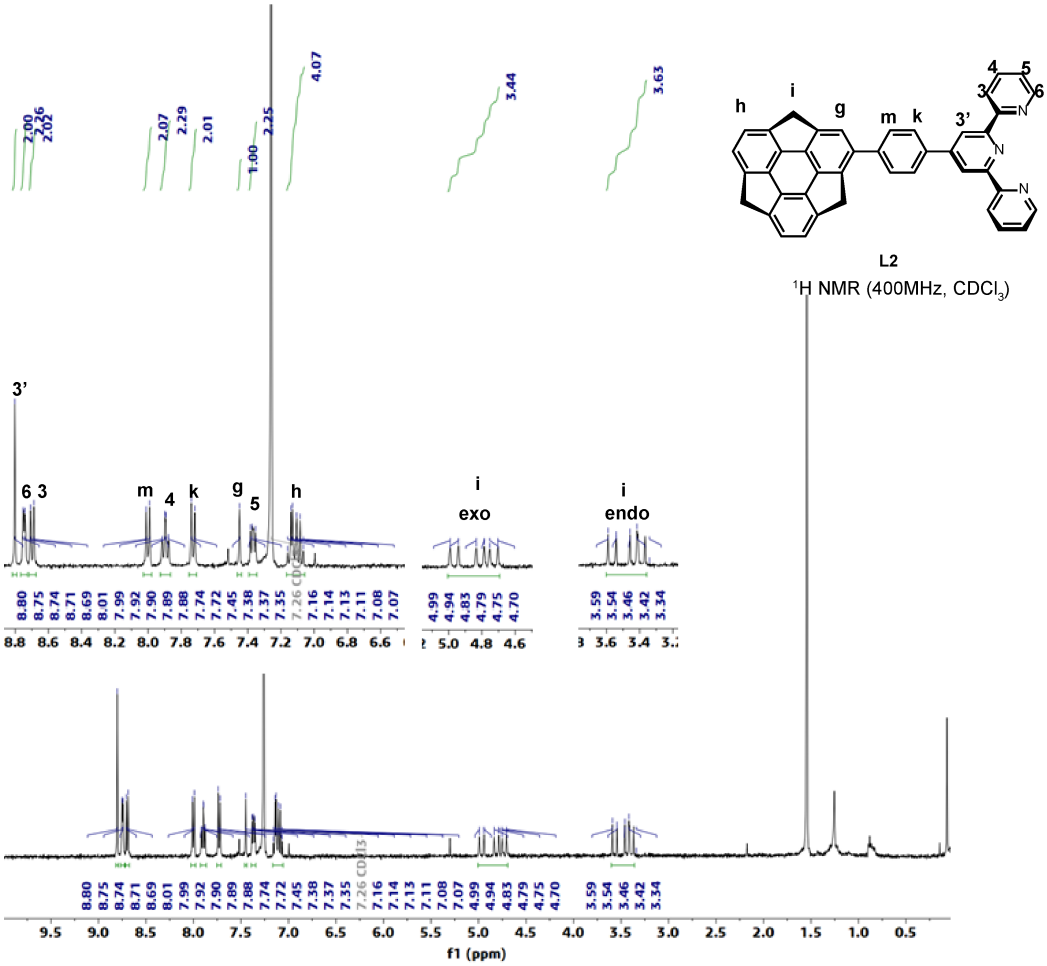

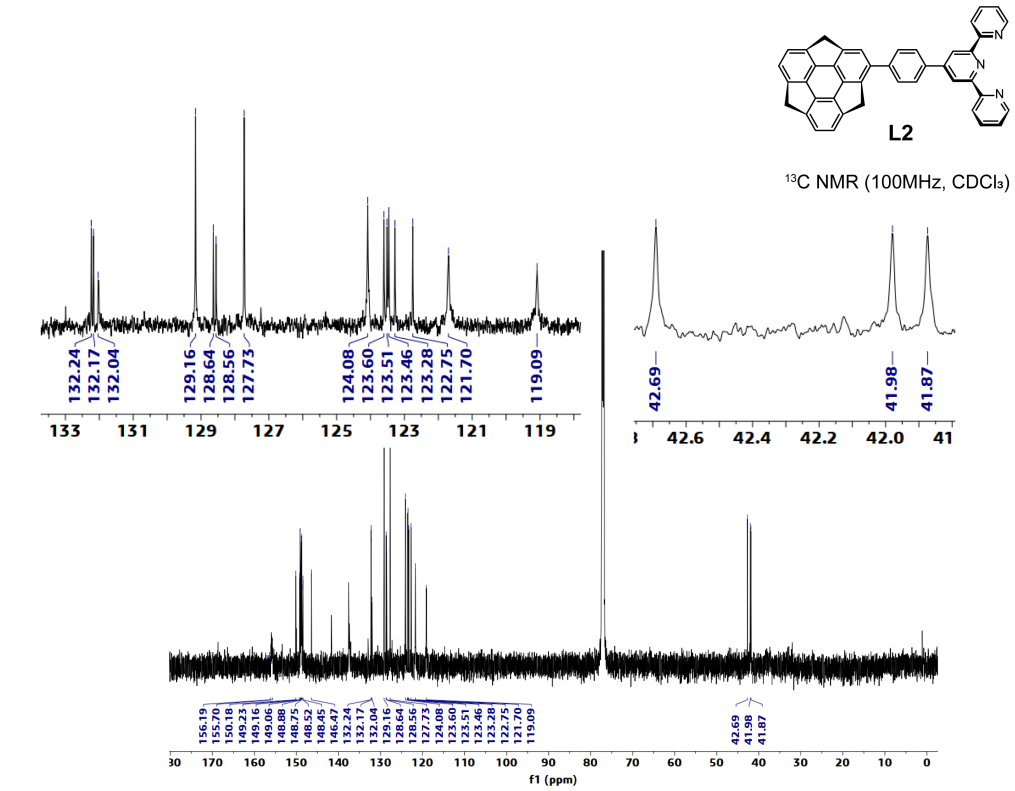

MALDI-TOF MS, ^{1}H NMR and COSY NMR charts of **C1**

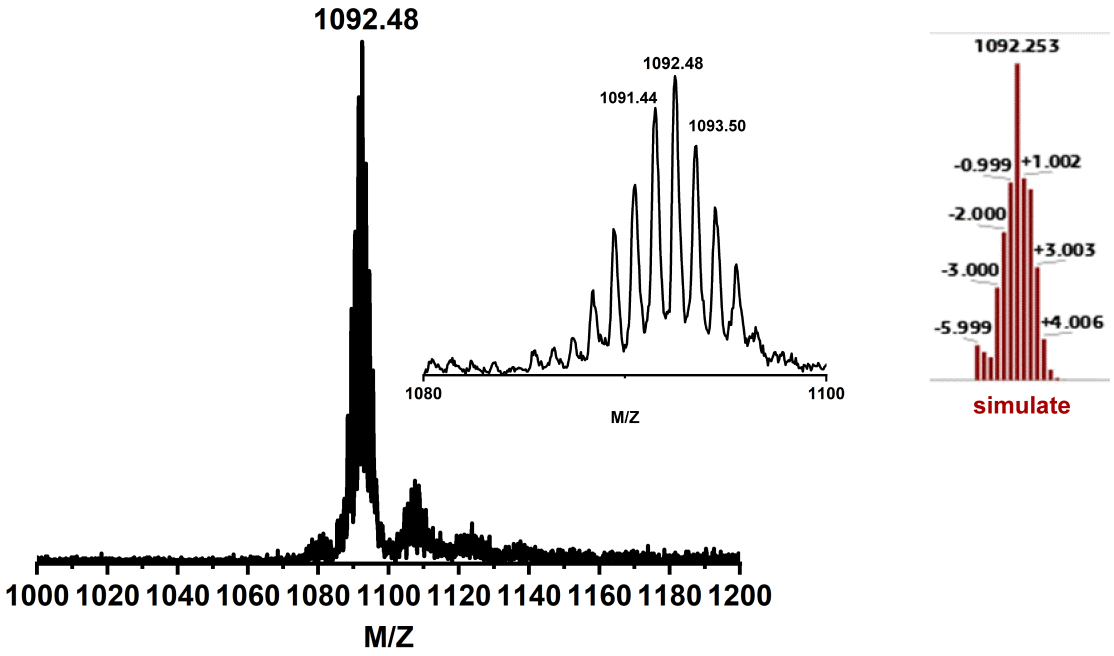
1092.48
1092.48
1091.44
1093.50
1080
1100
M/Z
1000 1020 1040 1060 1080 1100 1120 1140 1160 1180 1200
M/Z
1092.253
-0.999
+1.002
-2.000
+3.003
-3.000
+4.006
-5.999
simulate

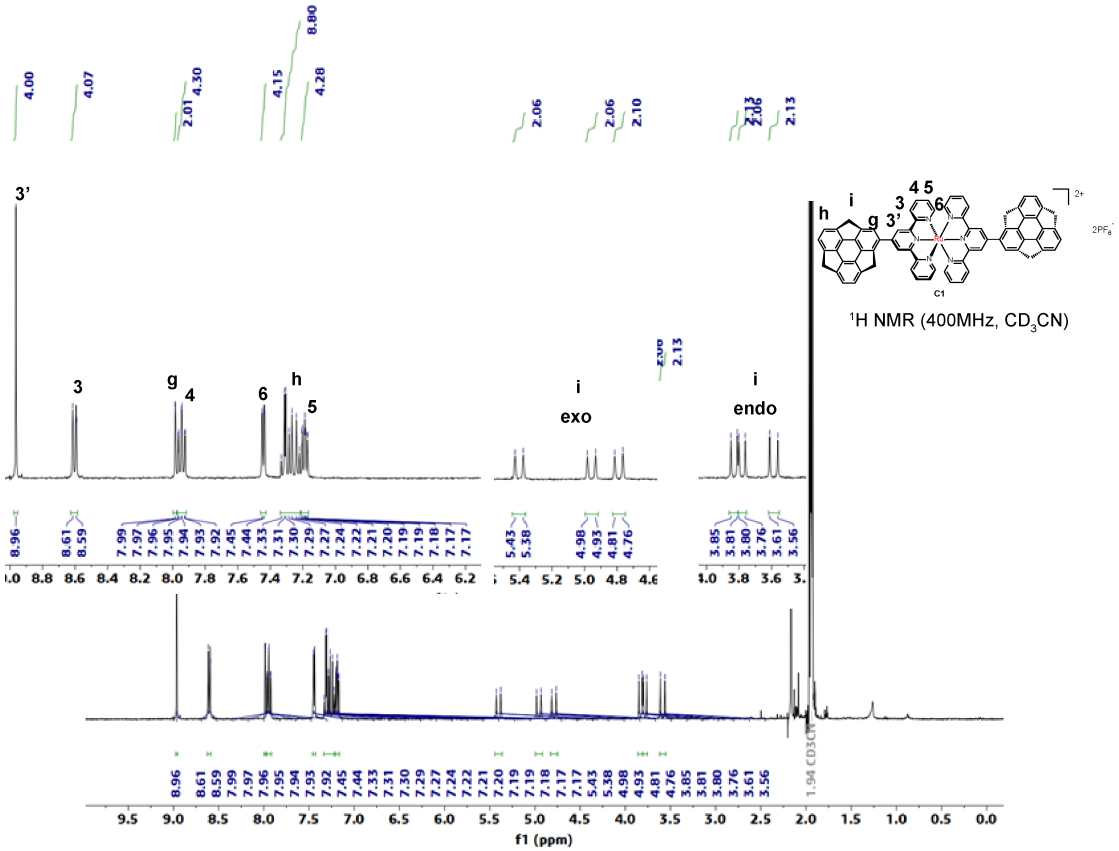
3'
3
g
4
6
h
5
i
exo
i
endo
h
i
g
3'
3
4 5
6
^{1}H NMR (400MHz, CD$_3$CN)
f1 (ppm)

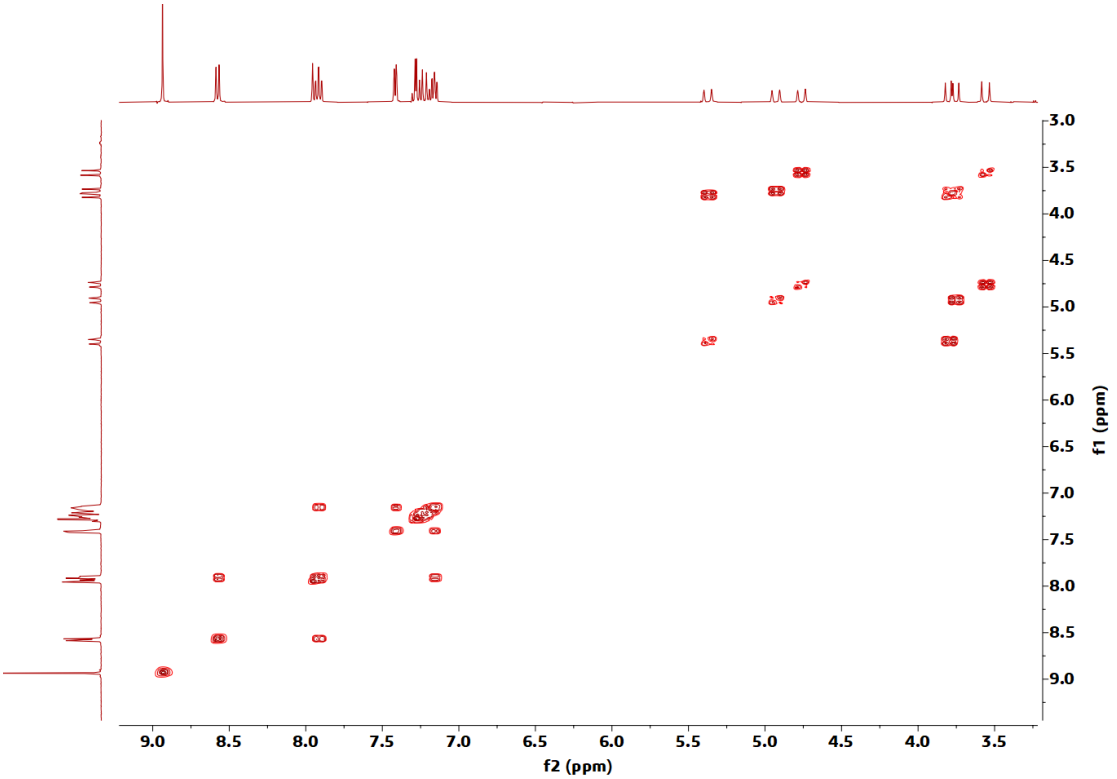

MALDI-TOF MS, ^{1}H NMR and COSY NMR charts of **C2**

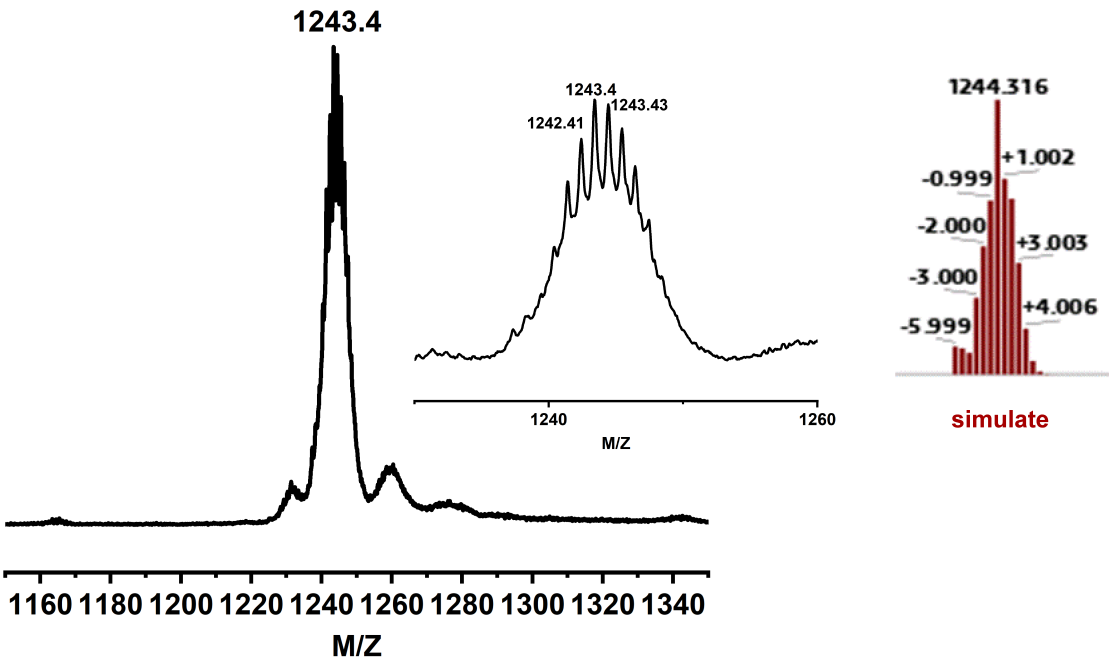

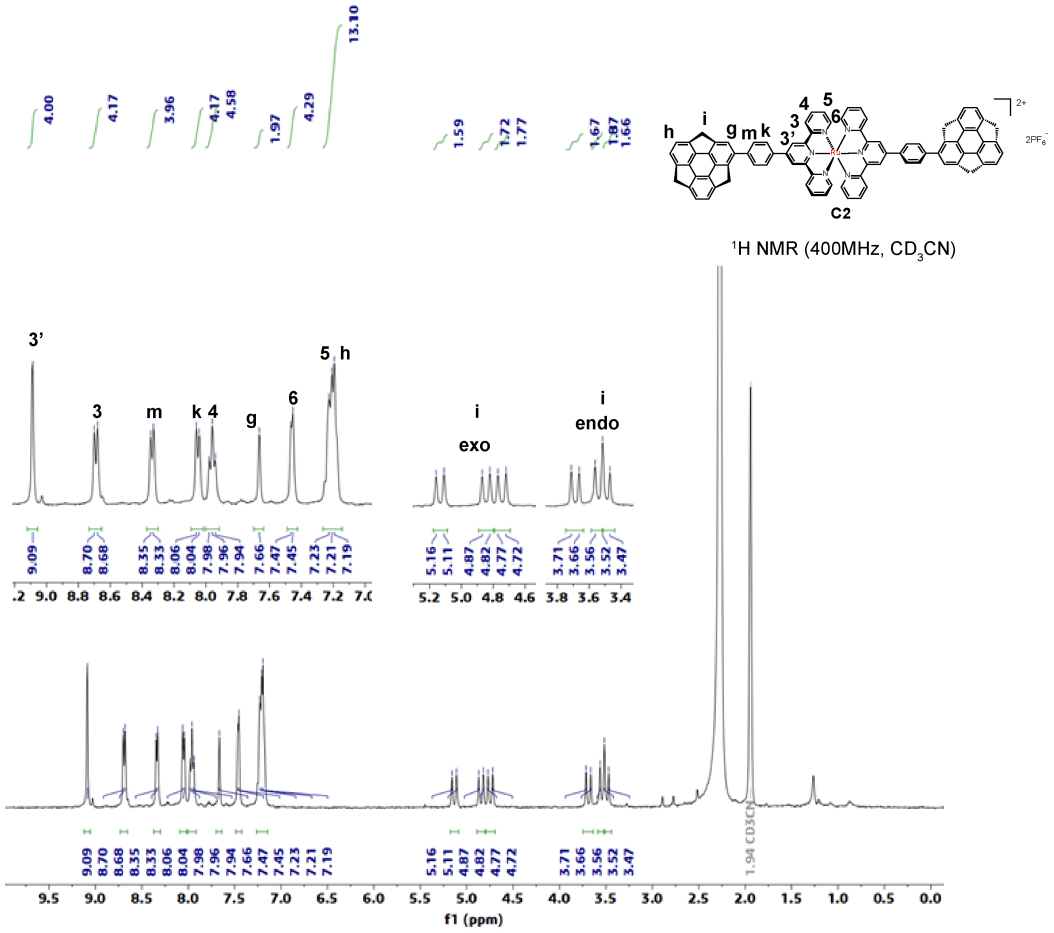
4.00
4.17
3.96
4.17
4.58
1.97
4.29
13.10
1.59
1.72
1.77
1.67
1.87
1.66
h
i
g
m
k
3
3'
4
5
6
C2
2PF6-
2+
1H NMR (400MHz, CD3CN)
3'
3
m
k
4
g
6
5
h
i
exo
i
endo
1.94 CD3CN
f1 (ppm)

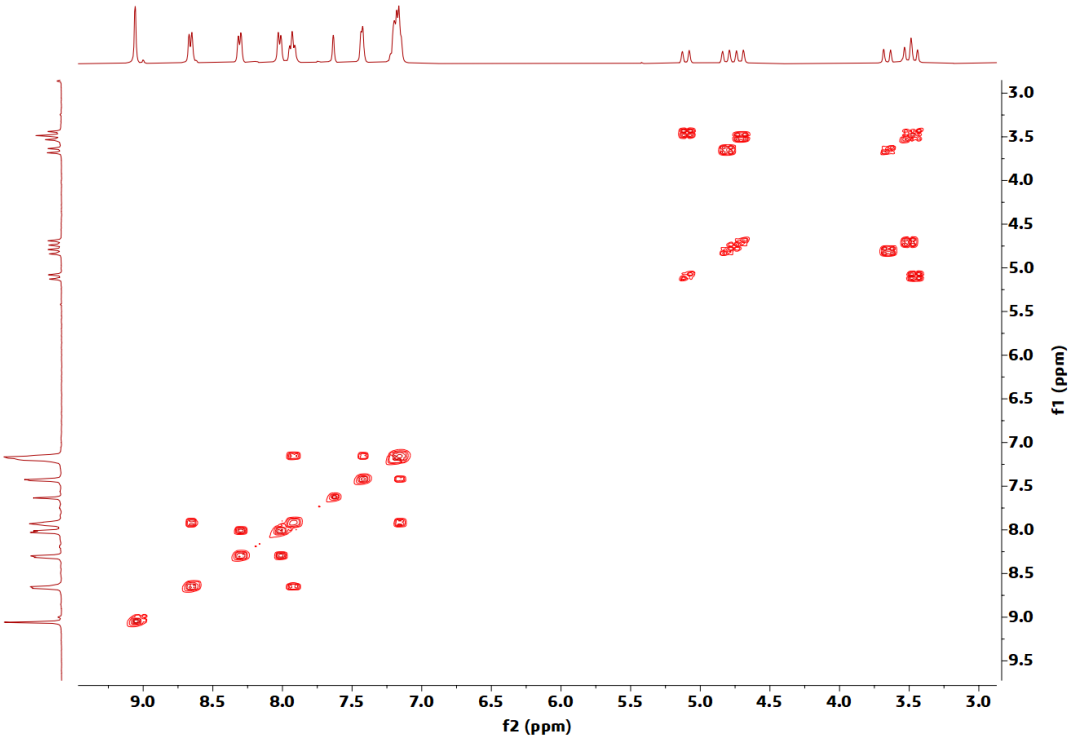
f2 (ppm)
f1 (ppm)

MALDI-TOF MS, ^{1}H NMR and COSY NMR charts of **C3**

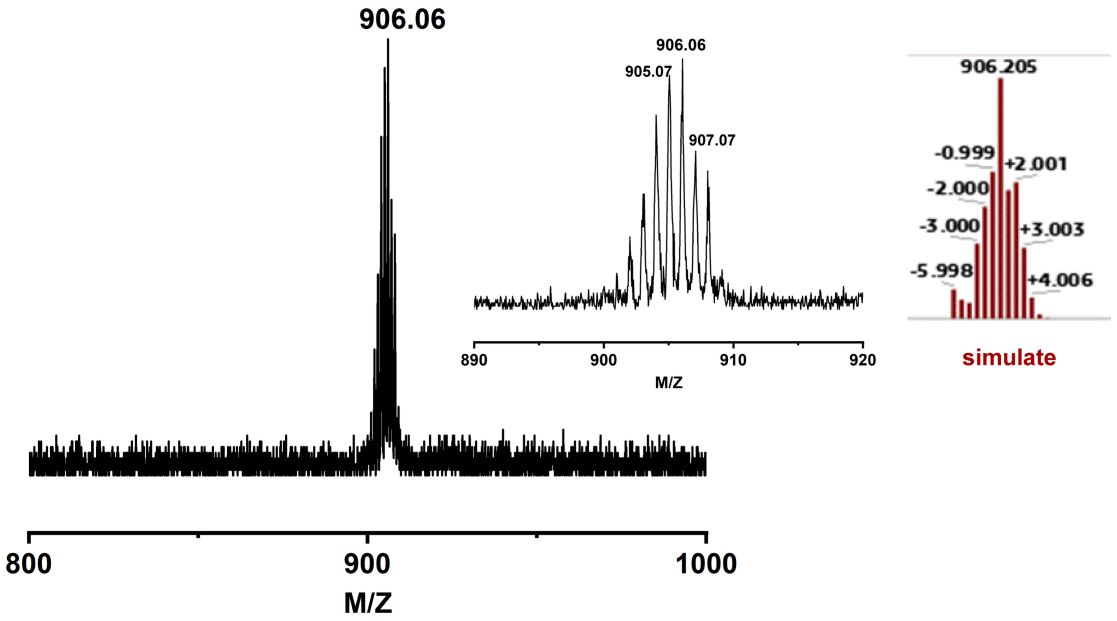

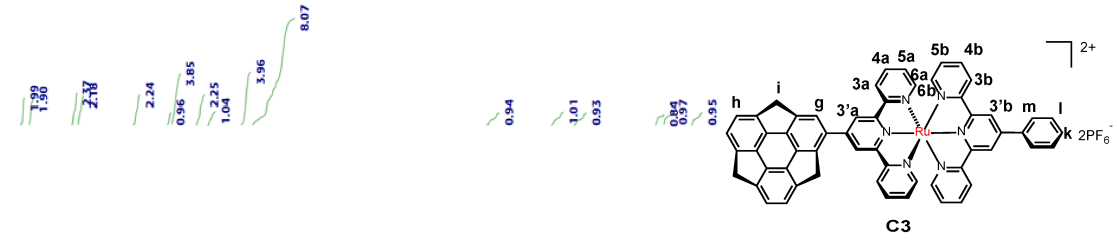

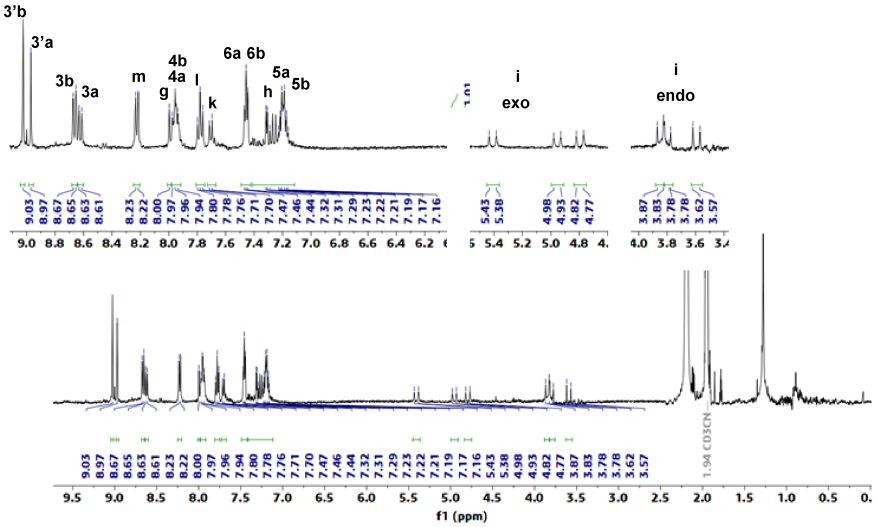

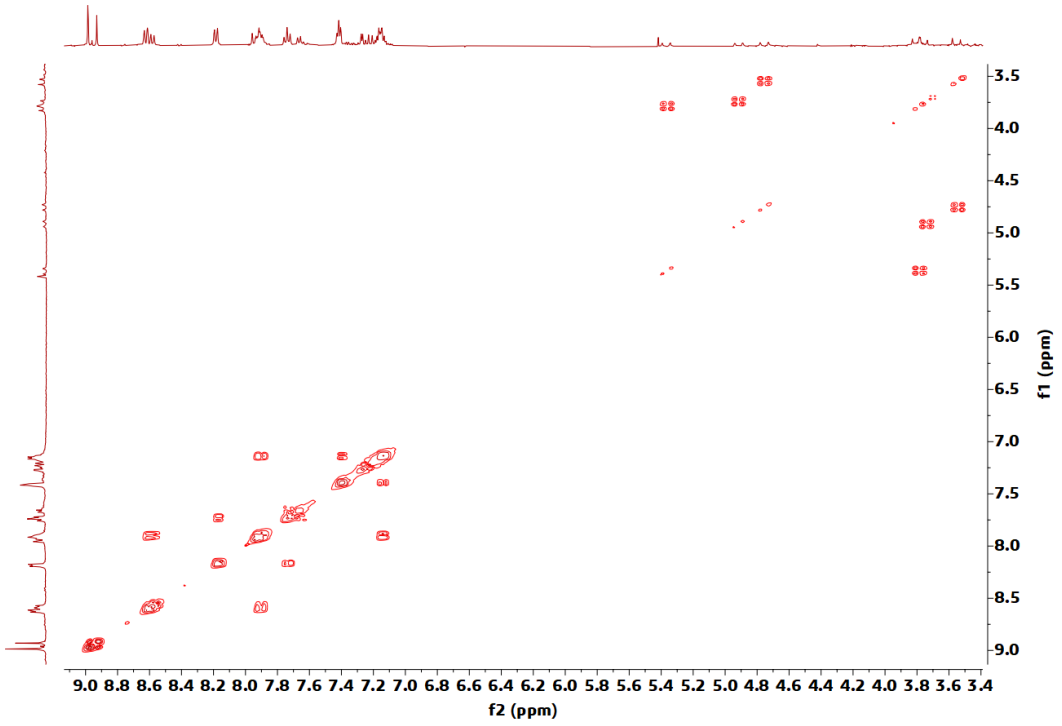
f1 (ppm)
f2 (ppm)

MALDI-TOF MS, ^{1}H NMR and COSY NMR charts of **C4**

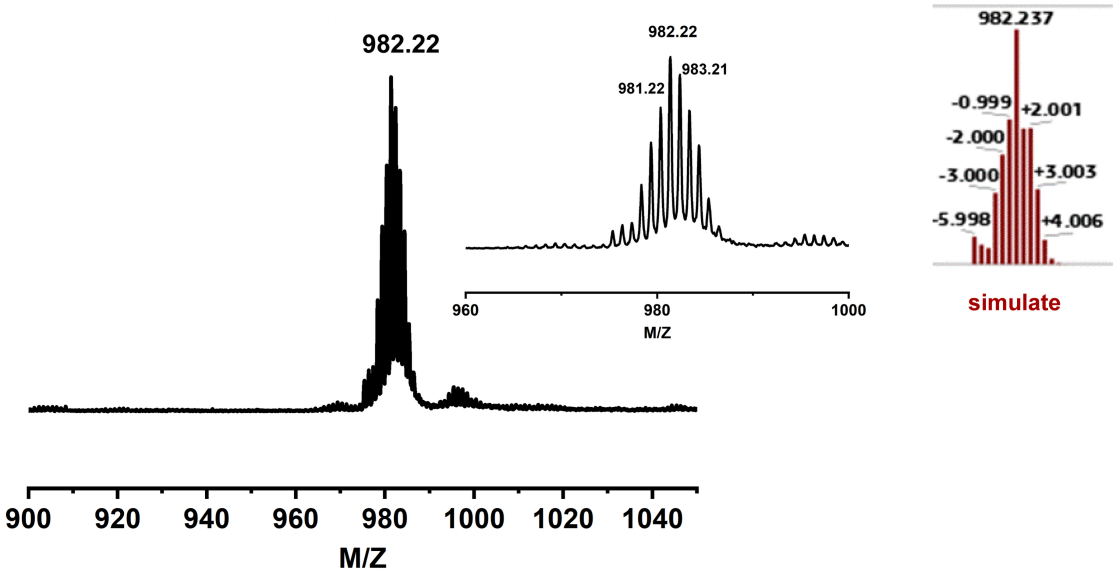

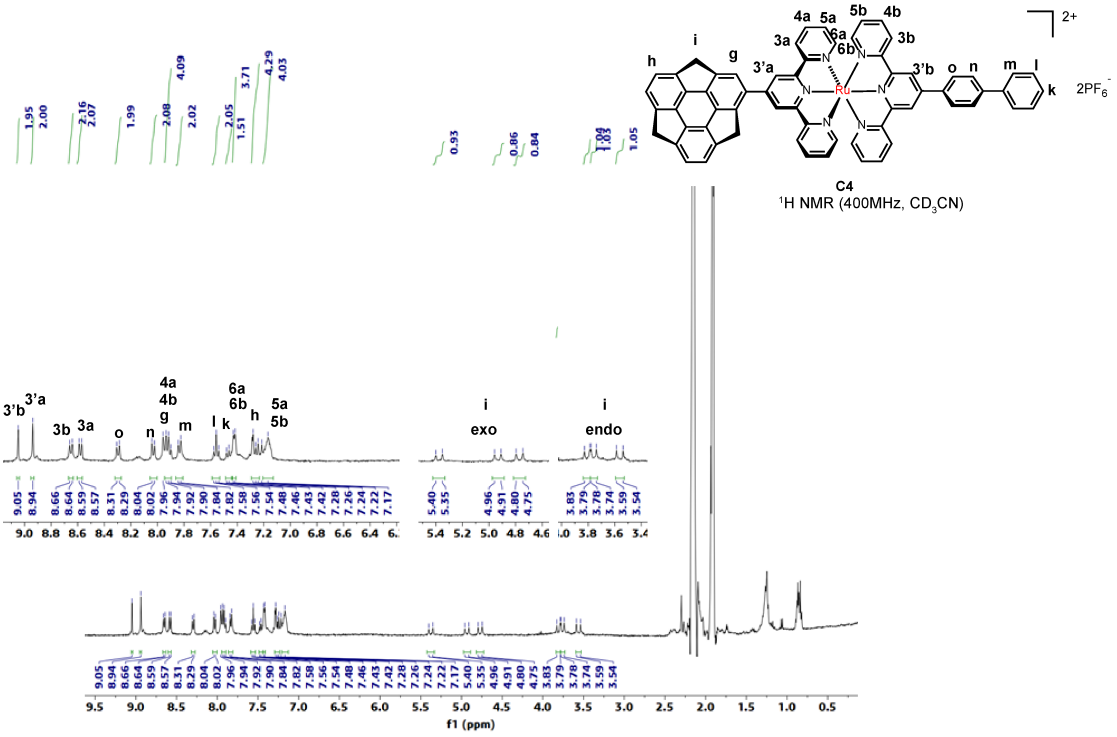

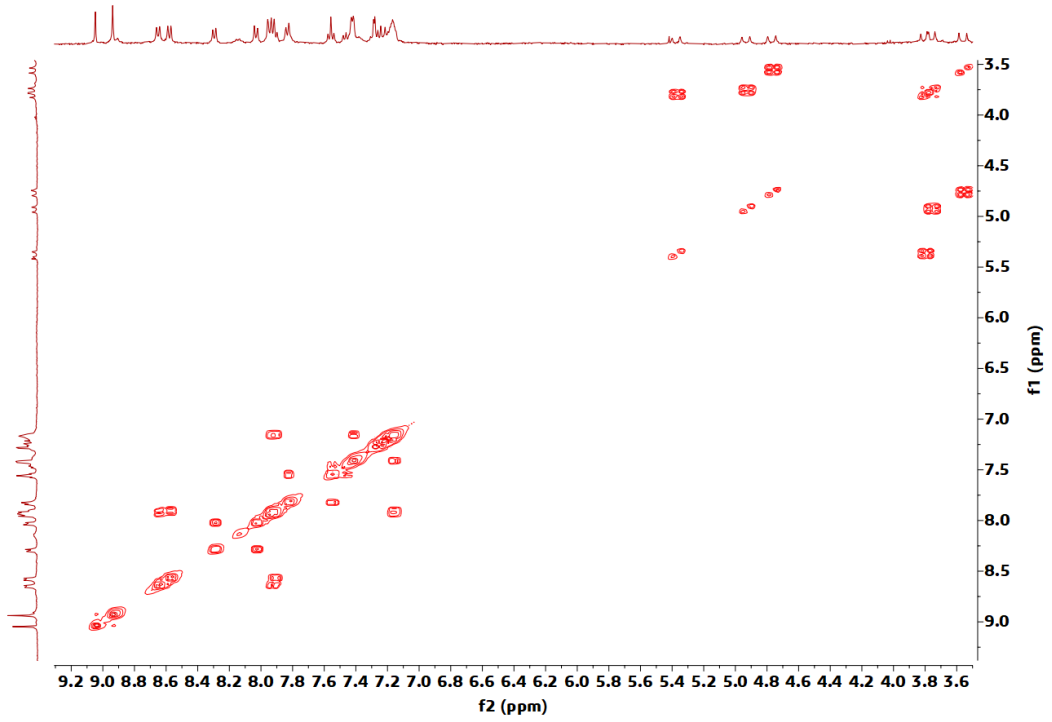
f1 (ppm)
3.5
4.0
4.5
5.0
5.5
6.0
6.5
7.0
7.5
8.0
8.5
9.0
9.2 9.0 8.8 8.6 8.4 8.2 8.0 7.8 7.6 7.4 7.2 7.0 6.8 6.6 6.4 6.2 6.0 5.8 5.6 5.4 5.2 5.0 4.8 4.6 4.4 4.2 4.0 3.8 3.6
f2 (ppm)

^{1}H NMR and COSY NMR charts of **SC2**

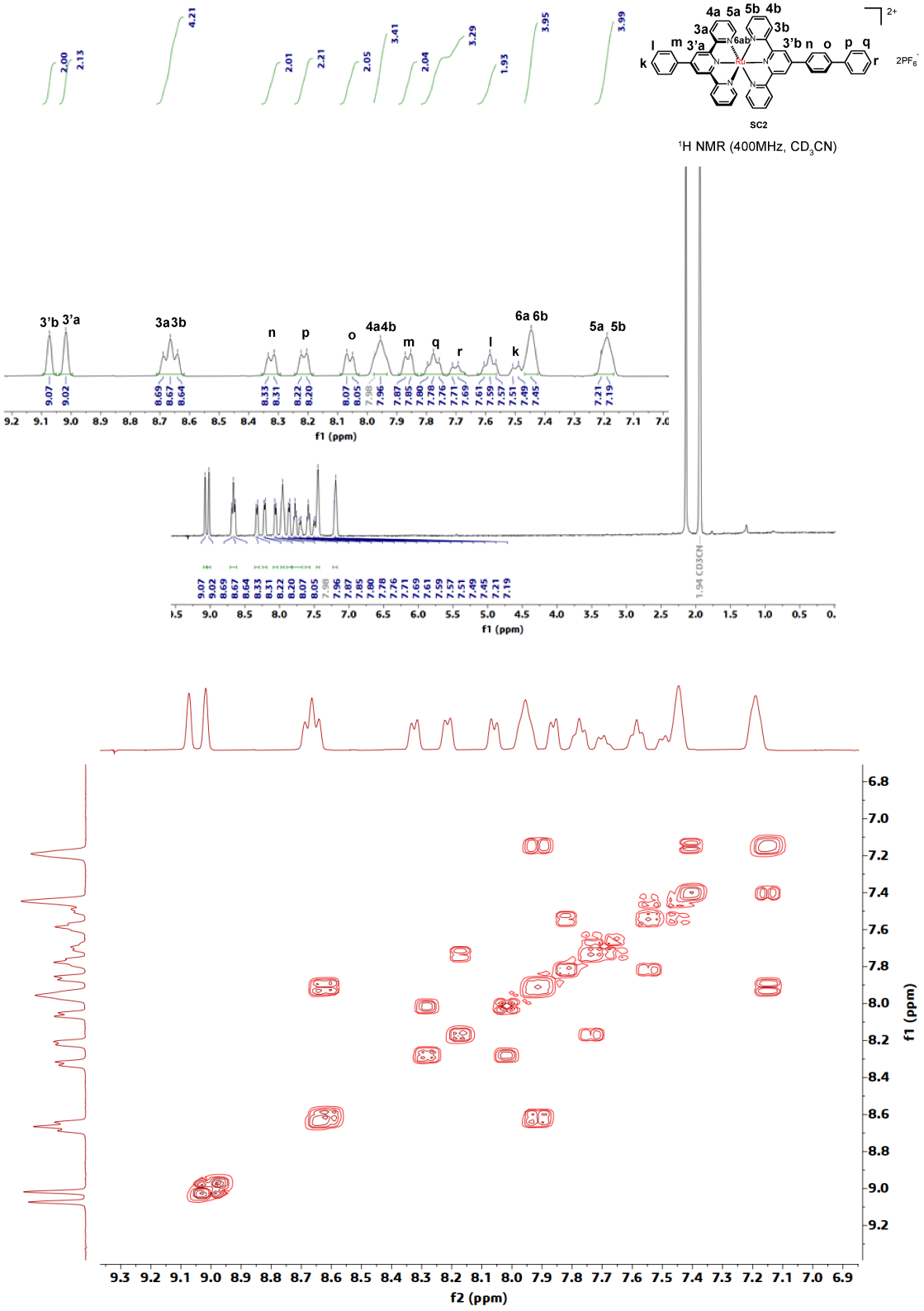

^{1}H NMR and COSY NMR charts of **SC3**

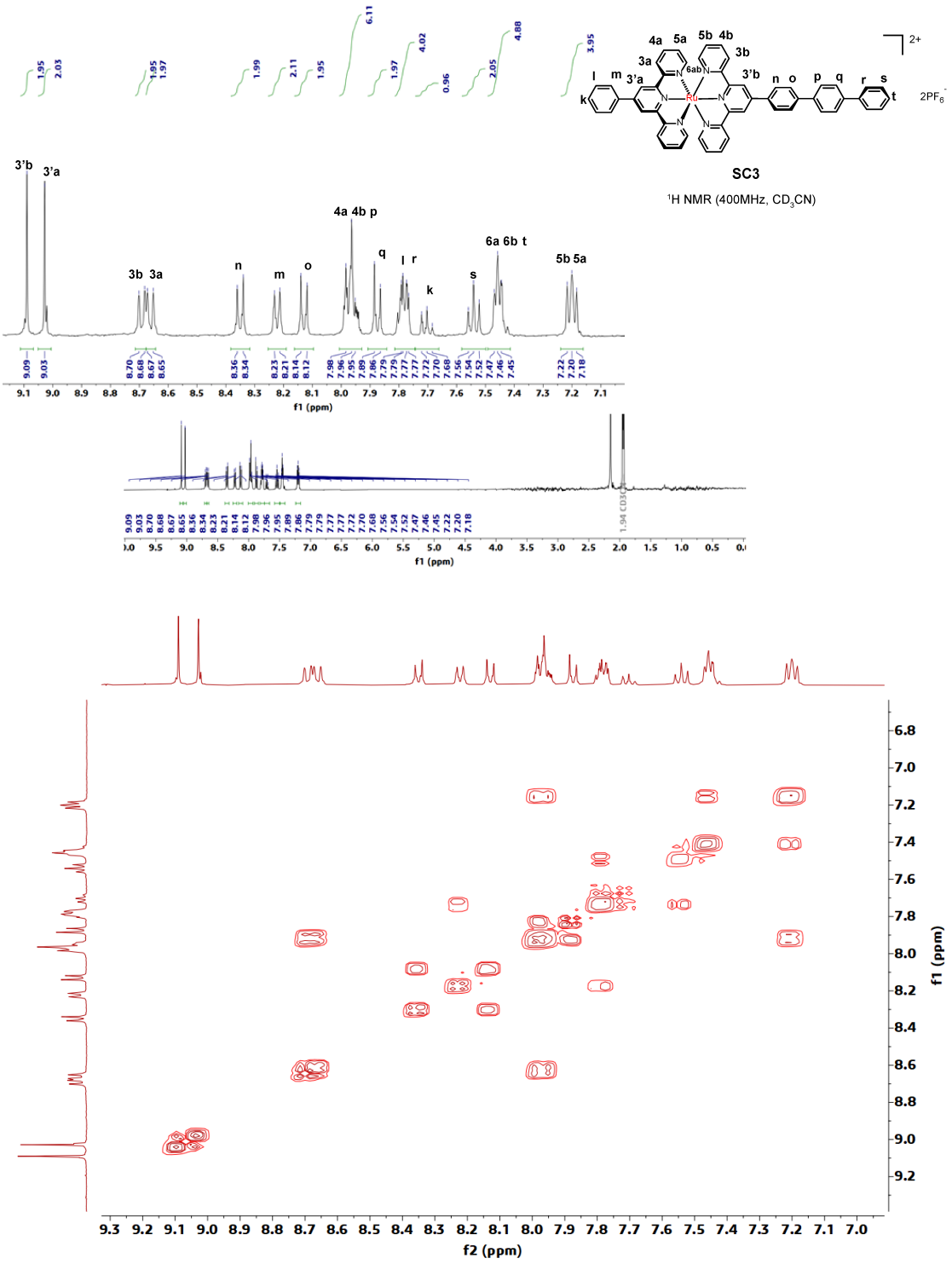

References

1. M. H. Keefe, K. D. Benkstein and J. T. Hupp, *Coord. Chem. Rev.*, 2000, **205**, 201.
2. N. H. Damrauer, G. Cerullo, A. Yeh, T. R. Boussie, C. V. Shank and J. K. McCusker, *Science*, 1997, **275**, 54.
3. P. G. Bomben, K. C. Robson, B. D. Koivisto and C. P. Berlinguette, *Coord. Chem. Rev.*, 2012, **256**, 1438.
4. J. P. Sauvage, J. P. Collin, J. C. Chambron, S. Guillerez, C. Coudret, V. Balzani, F. Barigelletti, L. De Cola and L. Flamigni, *Chem. Rev.*, 1994, **94**, 993.
5. H. Hofmeier and U. S. Schubert, *Chem. Soc. Rev.*, 2004, **33**, 373.
6. Y.-Q. Fang, N. J. Taylor, G. S. Hanan, F. Loiseau, R. Passalacqua, S. Campagna, H. Nierengarten and A. V. Dorsselaer, *J. Am. Chem. Soc.*, 2002, **124**, 7912.
7. D. Mondal, M. Bar, S. Mukherjee and S. Baitalik, *Inorg. Chem.*, 2016, **55**, 9707.
8. A. Graczyk, F. A. Murphy, D. Nolan, V. Fernández-Moreira, N. J. Lundin, C. M. Fitchett and S. M. Draper, *Dalton Trans.*, 2012, **41**, 7746.
9. D. Maity, S. Das, S. Mardanya and S. Baitalik, *Inorg. Chem.*, 2013, **52**, 6820.
10. S. Baitalik, X.-y. Wang and R. H. Schmehl, *J. Am. Chem. Soc.*, 2004, **126**, 16304.
11. P. Pal, S. Mukherjee, D. Maity and S. Baitalik, *Inorg. Chem.*, 2018, **57**, 5743.
12. S. Wadman, Y. van Leeuwen and R. Havenith, *Organometallics*, 2010, **29**, 1569.
13. G. J. Wilson, A. Launikonis, W. H. Sasse and A. W.-H. Mau, *J. Phys. Chem. A*, 1997, **101**, 4860.
14. D. S. Tyson, C. R. Luman, X. Zhou and F. N. Castellano, *Inorg. Chem.*, 2001, **40**, 4063.
15. L.-q. Song, J. Feng, X.-s. Wang, J.-h. Yu, Y.-j. Hou, P.-h. Xie, B.-w. Zhang, J.-f. Xiang, X.-c.

Ai and J.-p. Zhang, *Inorg. Chem.*, 2003, **42**, 3393.

16. T. E. Keyes, C. M. O'Connor, U. O'Dwyer, C. G. Coates, P. Callaghan, J. J. McGarvey and J. G. Vos, *J. Phys. Chem. A*, 1999, **103**, 8915.

17. E. C. Glazer, D. Magde and Y. Tor, *J. Am. Chem. Soc.*, 2007, **129**, 8544.

18. J. Wang, E. A. Medlycott, G. S. Hanan, F. Loiseau and S. Campagna, *Inorg. Chim. Acta*, 2007, **360**, 876.

19. R. Siebert, A. Winter, B. Dietzek, U. S. Schubert and J. Popp, *Macromol. Rapid Commun.*, 2010, **31**, 883.

20. R. Siebert, A. Winter, U. S. Schubert, B. Dietzek and J. Popp, *Phys. Chem. Chem. Phys.*, 2011, **13**, 1606.

21. H. Sakurai, T. Daiko and T. Hirao, *Science*, 2003, **301**, 1878.

22. H. Sakurai, T. Daiko, H. Sakane, T. Amaya and T. Hirao, *J. Am. Chem. Soc.*, 2005, **127**, 11580.

23. T. Amaya, H. Sakane, T. Muneishi and T. Hirao, *Chem. Commun.*, 2008, 765.

24. T. Amaya, S. Seki, T. Moriuchi, K. Nakamoto, T. Nakata, H. Sakane, A. Saeki, S. Tagawa and T. Hirao, *J. Am. Chem. Soc.*, 2009, **131**, 408.

25. M. Li, J. Wu, K. Sambe, Y. Yakiyama, T. Akutagawa, T. Kajitani, T. Fukushima, K. Matsuda and H. Sakurai, *Mater. Chem. Front.*, 2022, **6**, 1752.

26. H. Kojima, M. Nakagawa, R. Abe, F. Fujiwara, Y. Yakiyama, H. Sakurai and M. Nakamura, *Chem. Lett.*, 2018, **47**, 524.

27. Y. Shoji, T. Kajitani, F. Ishiwari, Q. Ding, H. Sato, H. Anetai, T. Akutagawa, H. Sakurai and T. Fukushima, *Chem. Sci.*, 2017, **8**, 8405.

28. D. Vijay, H. Sakurai, V. Subramanian and G. N. Sastry, *Phys. Chem. Chem. Phys.*, 2012, **14**,

3057.

29. S. N. Spisak, Z. Wei, N. J. O'Neil, A. Y. Rogachev, T. Amaya, T. Hirao and M. A. Petrukhina, *J. Am. Chem. Soc.*, 2015, **137**, 9768.

30. A. Kasprzak, A. Kowalczyk, A. Jagielska, B. Wagner, A. M. Nowicka and H. Sakurai, *Dalton Trans.*, 2020, **49**, 9965.

31. A. Kasprzak and H. Sakurai, *Chem. Commun.*, 2021, **57**, 343.

32. A. Kasprzak and H. Sakurai, *Dalton Trans.*, 2019, **48**, 17147.

33. B. B. Shrestha, S. Karanjit, G. Panda, S. Higashibayashi and H. Sakurai, *Chem. Lett.*, 2013, **42**, 386.

34. Z. Zhang, H. Wang, X. Wang, Y. Li, B. Song, O. Bolarinwa, R. A. Reese, T. Zhang, X.-Q. Wang and J. Cai, *J. Am. Chem. Soc.*, 2017, **139**, 8174.

35. T. Yoshihara, S. I. Druzhinin and K. A. Zachariasse, *J. Am. Chem. Soc.*, 2004, **126**, 8535.

36. A. N. Cammidge, V. H. Goddard, H. Gopee, N. L. Harrison, D. L. Hughes, C. J. Schubert, B. M. Sutton, G. L. Watts and A. J. Whitehead, *Org. Lett.*, 2006, **8**, 4071.

37. Z. Piontkowski and D. W. McCamant, *J. Am. Chem. Soc.*, 2018, **140**, 11046.

38. E. Villemin and O. Raccurt, *Coord. Chem. Rev.*, 2021, **435**, 213801.

39. M. J. Frisch, G. W. Trucks, H. B. Schlegel, G. E. Scuseria, M. A. Robb, J. R. Cheeseman, G. Scalmani, V. Barone, G. A. Petersson, H. Nakatsuji, X. Li, M. Caricato, A. V. Marenich, J. Bloino, B. G. Janesko, R. Gomperts, B. Mennucci, H. P. Hratchian, J. V. Ortiz, A. F. Izmaylov, J. L. Sonnenberg, Williams, F. Ding, F. Lipparini, F. Egidi, J. Goings, B. Peng, A. Petrone, T. Henderson, D. Ranasinghe, V. G. Zakrzewski, J. Gao, N. Rega, G. Zheng, W. Liang, M. Hada, M. Ehara, K. Toyota, R. Fukuda, J. Hasegawa, M. Ishida, T. Nakajima, Y. Honda, O. Kitao,

H. Nakai, T. Vreven, K. Throssell, J. A. Montgomery Jr., J. E. Peralta, F. Ogliaro, M. J. Bearpark, J. J. Heyd, E. N. Brothers, K. N. Kudin, V. N. Staroverov, T. A. Keith, R. Kobayashi, J. Normand, K. Raghavachari, A. P. Rendell, J. C. Burant, S. S. Iyengar, J. Tomasi, M. Cossi, J. M. Millam, M. Klene, C. Adamo, R. Cammi, J. W. Ochterski, R. L. Martin, K. Morokuma, O. Farkas, J. B. Foresman and D. J. Fox.*Journal*, 2016.

40. T. Lu and F. Chen, *J. Comput. Chem.*, 2012, **33**, 580.

Chapter 3. Derivatization of trioxosumanene by Lewis acid-mediated Suzuki-Miyaura coupling and an unprecedented ring opening

Section 1. Unique electronic features of trioxosumanene

Trioxosumanene (**1**) is a bowl-shaped aromatic ketone in which all three benzylic positions of sumanene are fully oxygenated (Figure 1).[1] The unique properties of **1** are represented by the strong electron-accepting ability to have the first reduction potentials at −0.92 V, and the second one at −1.43V (vs. Fc/Fc^+, Fc: ferrocene).[2] These values are more positive than boron-doped polycyclic aromatic hydrocarbon[3], fluorenone derivatives[4], and fullerene derivatives[5]. Another unique feature of **1** is that the ISC from the triplet state to S_0 was faster than that of the planar triplet ketones such as triplet fluorenone. This is caused by the larger SOC than the planar system due to curved structure.[6] These unique electronic features make **1** a promising material for the application to electron injection[7] and organic phosphorescent materials[8, 9].

In terms of the utilization of the molecular synthesis, **1** also has the potential to be a precursor for functionalized sumanenes by the modification of three carbonyl group by nucleophilic addition reactions. Indeed, the preparation of hexafluorosumanene[10] from **1** brought a new opportunity to utilize fluorosumanenes as Debye-type dielectric responsive materials.[11, 12] In contrast, the study of chemical modification of **1** at the aromatic periphery is scarce. Only one derivative having trioxosumanene moiety **1**, trimethyltrioxosumanene, is prepared by oxidation of trimethylsumanene.[13] The problem of the chemical modification of **1** lies in the poor reactivity at the aromatic periphery, especially against aromatic electrophilic substitutions due to its its electron-deficient character than the non-oxygenated sumanene.

Furthermore, the susceptibility of **1** against base significantly restricts the choice of the transformation methods. Here, the author propose new chemical modification method of **1** employing Lewis-acid mediated Suzuki−Miyaura coupling reaction via mono- brominated derivative, bromotrioxosumanene (**2**), to obtain various coupling products **3**-**7** (Figure 1). In addition, the author unexpectedly observed the pentagonal ring opening in the preparation of 2-hydroxyohenyl derivative **8** even at the room temperature within 1 min without any activation.

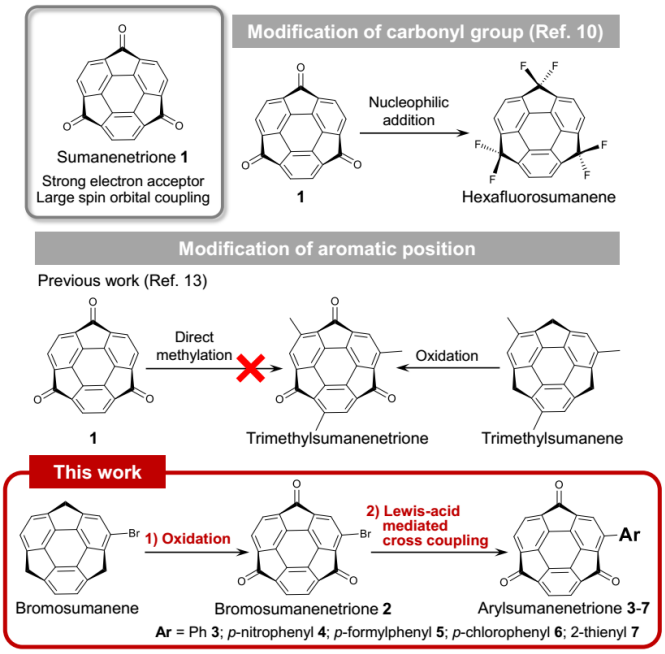

Figure 1. Modification of **1** at carbonyl group and aromatic periphery.

Section 2. Synthesis and properties of trioxosumanene derivatives

Bromotrioxosumanene **2** was prepared from previously reported bromosumanene [14] through Ru-mediated oxygenation in 43% yield (Scheme 1). First, phenylation of **2** by the Suzuki−Miyaura cross-coupling was investigated (Table 1). When the reaction was carried out under the general Suzuki−Miyaura coupling reaction condition using the combination of $Pd(PPh_3)_4$ and K_2CO_3 in the mixture of THF and water, **2** was immediately consumed to give

the complicated by-products mixture instead the desired coupling product, indicating **2** was unstable under basic K_2CO_3/H_2O conditions. Changing the base to CsF did not solve the problem. These results suggested that **2** is unstable under basic conditions. Therefore, the author tried several representative protocols using aryl borate, which does not require the addition of an external base. In Entry 3, the reaction was conducted with choline hydroxide (ChOH), an ionic liquid, which consists of a tertiary amine and hydroxide,[15] and potassium trifluoro(phenyl)borate instead of boronic acid.

Table 1 Optimization of the reaction conditions in Suzuki-Miyaura cross coupling**.**

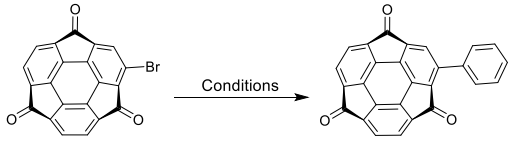

2 **3**

Entry	Organoborons	Conditions[a]	Yield of **3**
1	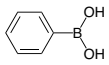 (120 mol%)	$Pd(PPh_3)_4$ (10 mol%) K_2CO_3 (100 mol%) THF/H_2O, 80 °C, 1 h	0
2	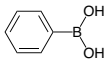 (120 mol%)	$Pd(PPh_3)_4$ (10 mol%) CsF (100 mol%) $toluene/H_2O$, 80 °C, 1 h	0
3	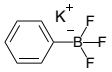 (120 mol%)	$Pd(OAc)_2$ (10 mol%) $ChOH/H_2O$, 100 °C, 1 h	0
4	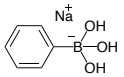 (100 mol%)	$PdCl_2(dppf)$ (10 mol%) toluene, reflux, 1 h	0
5	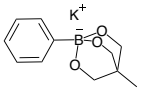 (100 mol%)	$Pd(OAc)_2$ (10 mol%) DMF, 80 °C, 1 h	0
6	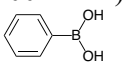 (120 mol%)	$PdCl_2(amphos)_2$ (2 mol%) $((tmeda)Zn(OH)(OTf))_3$ (150 mol%) THF, 80 °C, 1 h	89%

[a] **2** (0.050 mmol), solvent (2mL). [b] ChOH: choline hydroxide

However, it also turned out to be ineffective. The trial to use the combination of sodium phenyl boronate with toluene to perform the reaction under anhydrous and base-free conditions also resulted in no reaction (Entry 4).[16] Further entry using highly stable and

soluble potassium phenyltriolborate[17] under milder conditions and still did not give positive result (Entry 5). The author finally arrived at the recently reported Lewis acid-mediated Suzuki−Miyaura coupling reaction, which is applicable to the base-susceptible substrates.[18] When **2** was treated with phenylboronic acid in the presence of $PdCl_2(amphos)_2$ and $((tmeda)Zn(OH)(OTf))_3$ in THF at 80 °C for 1 h, the desired coupling product **3** was successfully obtained in 89% yield (Entry 6). This success of the coupling reaction motivated us to make a variety of derivatizations with several kinds of aromatic compounds to find that all the products **4**-**7** were obtained in good yields (Scheme 1).

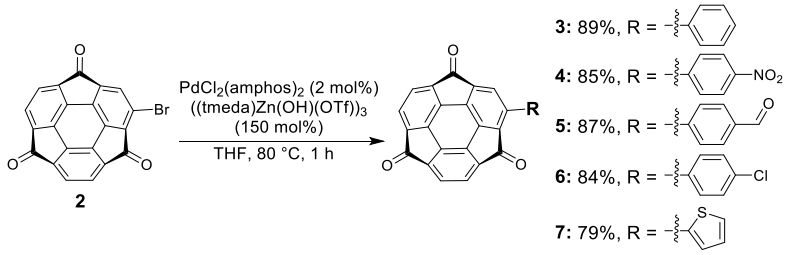

Scheme 1. Synthesis of **3**−**7**.

The UV-vis absorption and photoluminescence (PL) spectra of **3** to **7** in 10^{-5} M CH_2Cl_2 solution are shown in Figure 2. All the compounds showed two main absorption bands, one in the UV range of 250 nm to 400 nm and the other in the visible range of 450 nm to 650 nm (Figure. 2A). The longer wavelength peak of all the phenyl derivatives **3**-**6** appeared at nearly the same position to be 525 nm. More electron-donating thiophene-introduced **7** showed the clear red shift of the corresponding absorption peak to reach 580 nm. DFT calculation performed at B3LYP/6-311G(d,p) level of theory revealed that, in all cases, the highest occupied molecular orbital (HOMO) was distributed over the entire molecular backbone. In contrast, the lowest unoccupied molecular orbital (LUMO) was distributed exclusively on the

trioxosumanene moiety (Figure. 3), indicating that the absorption bands in the visible region were derived from the charge transfer from the substituent to trioxosumanene moiety.

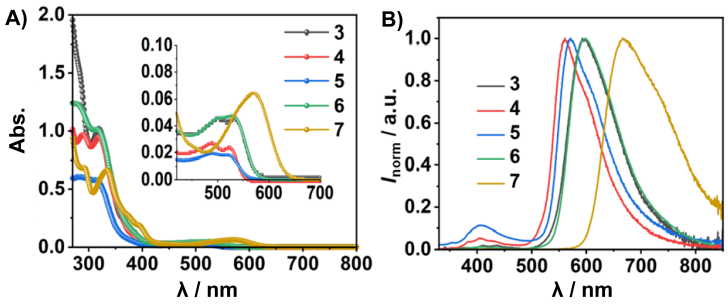

Figure 2. (a) UV−vis absorption spectra and (b) emission spectra (λex = 320 nm) of **3**−**7** in CH_2Cl_2 (1.0×10^{-5} M).

The time-dependent density functional theory (TD-DFT) calculation performed at B3LYP/6-311G(d,p) level of theory well explained this assumption. The calculated UV–vis absorption spectra corresponding electron–hole distributions exhibit significant charge separation, consistent with an intramolecular charge-transfer excited state. (Figure. 4 and 5). Notably, even the nitrophenyl group, typically recognized as a strong electron-accepting unit, worked as the donor moiety in this system. This clearly demonstrated the extraordinal electron-accepting ability of **1**.

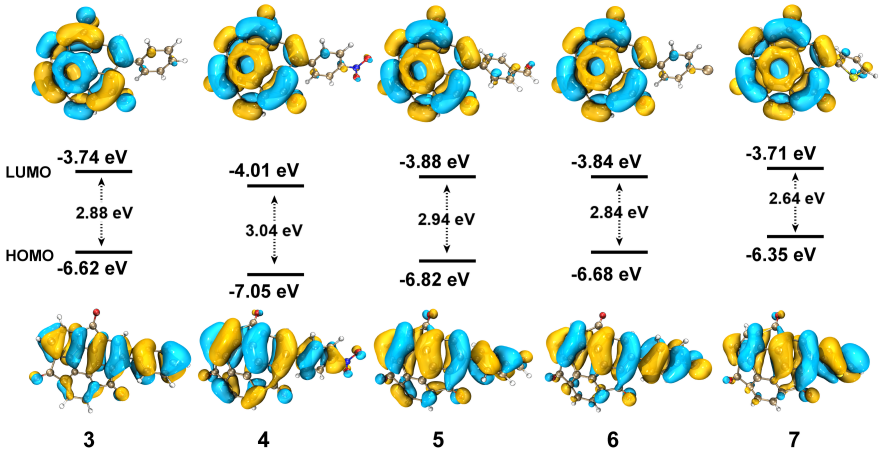

Figure 3. HOMO and LUMO of **3**−**7** obtained by DFT calculation performed at B3LYP/6-311G(d,p) level of theory.

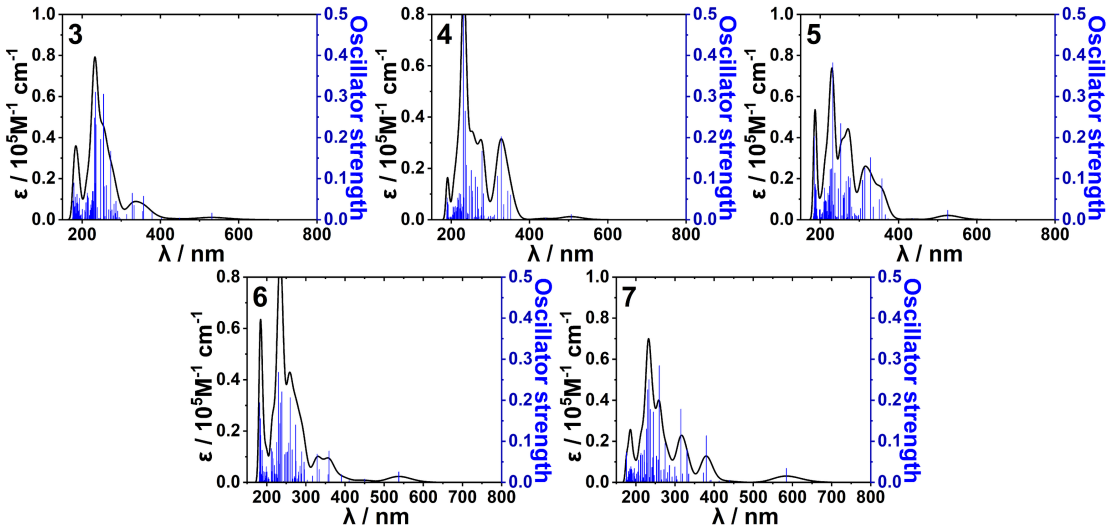

Figure 4. Simulated UV-vis spectra of **3**-**7**.

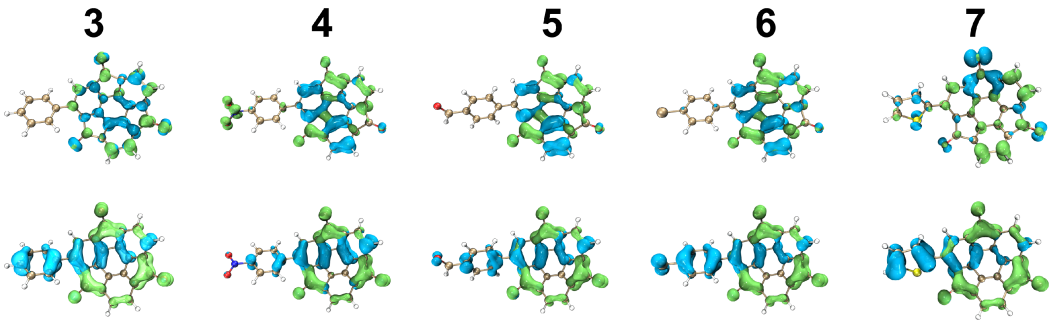

Figure 5. The distribution of hole (blue) and electron (green) of **3**-**7** at absorption 380 nm (top) and 550 nm (bottom).

In the case of emission spectra, two peaks were observed in **3** to **7**, one at 410 nm with weak intensity and the other ranging from 560 to 668 nm (Figure. 3B). The latter band showed red shift as the electron-donating ability of the substituent increased. Such HOMO and LUMO orientation indicated that the luminescence at 410 nm came from the locally-excited (LE) state of trioxosumanene moiety.[19] In comparison, the luminescence from 560 to 668 nm was thought to be from a charge-transfer state. The HOMO and LUMO energy gap decreased with

the electron-donating thiophene group in **7** through the increment of HOMO level, consistent with the experimental UV absorption and PL spectra.

Among the coupling products, **7** showed significant positive solvatoluminochromism as a function of permittivity of organic solvent (Figure. 6). Changing the solvent from hexane to acetonitrile caused almost 100 nm red shift of the emission at the visible to NIR region, indicating a significant intermolecular charge transfer (ICT) nature in the excited state. The Lippert-Mataga plot[20, 21] of **7** referring to the Stokes shift $\Delta\nu$ and the solvent polarizability Δf revealed that **7** shows two-section lines with an inflection point. In low polarity solvents, **7** exhibited a significant dipole moment change ($\Delta\mu$ is 11.22 D). However, in high polarity solvents, the dipole moment changes of **7** were much smaller than in the case of less polar solvents ($\Delta\mu$ is 1.21 D, Table S2, ESI). This phenomenon of **7** exhibiting both charge transfer and local excited properties is probably caused by the hybridization of the LE and CT states.[22, 23]

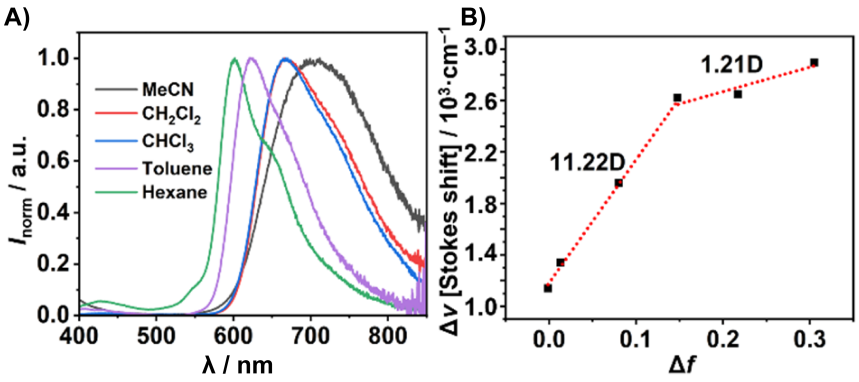

Figure 6. A) PL spectra (λ_{ex} = 320 nm) of **7** in four types of solvents (c =10^{-5} M). B) Linear fitting of Lipert-Mataga plots of **7**.

Section 3. Unexpected ring-opening reaction

Following the optical measurement results of electron-donating thiophene-introduced **7**, further preparation of 2-hydroxyphenyl derivative **8**, which was expected to be a valuable ligand for the complexation with metal ions was investigated.[24-27] The reaction was performed under the same conditions using 2-hydroxyphenylboronic acid. The crude ^{1}H NMR spectrum proved the formation of the desired product **8**. However, it was found that **8** was unexpectedly unstable to be converted to another product during the purification process. In particular, the use of MeOH gave an identifiable and isolable product **9**. When the percentage of methanol to THF was increased to 90%, the reaction took place even within one minute to give **9** in 47% yield (Figure 7A). Although the data quality was insufficient, single crystal X-ray analysis results also supported the characterized structure, in which the adjacent pentagonal ring of the substituent opened to produce a more planar molecular skeleton (Figure 7B). Generally, the corresponding ring opening reaction from the planar fluorenone to biphenyl carboxylic acid requires much more harsh conditions with a strong base (i.e., 270-300 °C under a molten state of sodium hydroxide and potassium hydroxide conditions).[28] In contrast, the current reaction of **8** proceeds even at room temperature without the addition of acid or base, indicating that the strain release effect probably worked as a driving force for the ring-opening reaction.[29, 30] Since the C−C bond cleavage proceeded exclusively at the adjacent position to the 2-hydroxyphenyl group, its participation to the reaction mechanism was strongly expected. A possible reaction pass of the ring-opening with a supportive proposition of DFT calculation is initiated by the formation of hemiketal intermediates generated by the nucleophilic addition of MeOH to the carbonyl carbon (Figure 8). Further C−C bond cleavage

was probably caused via intramolecular proto-deacylation-like mechanism, which was assisted by forming a hydrogen-bonded six-membered ring structure.

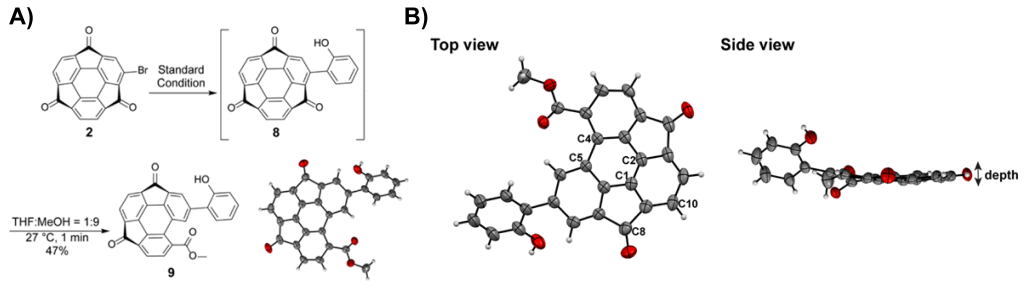

Figure 7. A) Unexpected ring opening from **8** and thermal displacement ellipsoid plot of **9** in a crystal structure. B) Thermal displacement ellipsoid plot of **9** in a crystal structure with 50% probability. The bond length of C1 to C2 is 1.340 Å and C4 to C5 is 1.512 Å, the depths of **9** at C10 and C8 are 0.331 and 0.232 Å, respectively.

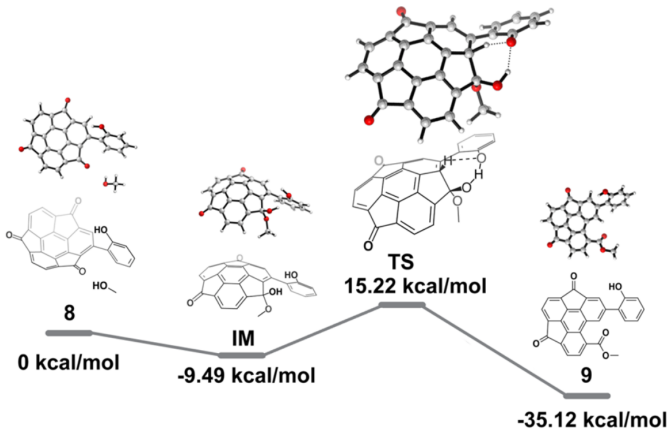

Figure 8. Computed free energy profile for the ring opening reaction of **8** to **9** at B3LYP/def2-TZVP level in SMD (methanol) solvent model.

Section 4. Summary

In summary, the author overcame the inherent difficulty of chemical modification of **1** using the Lewis-acid mediated Suzuki−Miyaura coupling reaction via bromotrioxosumanene to obtain various coupling products. The optical properties of the products revealed that the

trioxosumanene moiety has significant electron acceptability. Even at room temperature, the high strain of the bowl caused the ring-opening reaction on 2-hydroxyphenyl-substituted trioxosumanene at the adjacent pentagonal ring to occur without activation. This study opens a new way for the rational use of trioxosumanene as a new type of curved-π electron-acceptor. Further investigation via fine energy gap tuning by appropriate electron donor introduction will afford a great opportunity for the potential application of trioxosumanene in organic optoelectronic devices.

Experimental section

Instrumentations and chemicals

All the chemical reagents and solvents were commercially purchased and purified according to the standard methods, if necessary. Air- and moisture-sensitive reactions were carried out using commercially available anhydrous solvents under inert atmosphere of nitrogen. Unless otherwise noted. ^{1}H and ^{13}C NMR spectra were recorded on a JEOL JNM-ECS400 and Bruker AVANCE III 600 spectrometers. Chemical shift (δ) are expressed relative to the resonances of the residual non-deuterated solvent for ^{1}H ($CDCl_3$: $^{1}H(\delta)$ = 7.26 ppm, THF-d_8: $^{1}H(\delta)$ = 3.58, 1.72 ppm, DMSO-d_6: $^{1}H(\delta)$ = 2.50 ppm) and for ^{13}C ($CDCl_3$: $^{13}C(\delta)$ = 77.0 ppm, THF-d_8: $^{13}C(\delta)$ = 67.21, 25.31 ppm). High resolution mass spectra (HRMS) were measured using electron impact (EI) methods on JEOL JMS-777V spectrometer. Recycling preparative high-performance liquid chromatography (HPLC) was performed by a LC-908W (Japan Analytical Industry Co., Ltd.) with high-resolution gel permeation chromatography (GPC) column (Japan Analytical Industry Co., Ltd., JAIGEL-1H and 2H) with $CHCl_3$ as an eluent. The preparative TLC (PTLC) purification was conducted using Wako gel B-5F PTLC plates. Flash column chromatography was prepared using Kanto Silica gel 60N (neutral, spherical, 40-50 μm) and performed with a Yamazen preparative medium pressure liquid chromatography system. UV-vis spectra were recorded on a JASCO V-670 spectrophotometer. Steady-state emission spectra were recorded on a JASCO FP-6500DS spectrometer. Melting points were determined on an Optimelt MPA100 automated melting point apparatus (Stanford Research Systems, Inc.), and expressed without correction. Infrared (IR) absorption spectra were measured by attenuated total reflection (ATR) method on a JASCO FT/IR-4100 Fourier

transform IR spectrometer equipped with a JASCO ATR PRO ONE single reflection ATR optical attachment and a diamond crystal plate.

Lippert Mataga plot

The Stokes shift was determined as the difference in wavenumber between the lowest energy absorption and the highest energy florescence band. Estimates of these values obtained experimentally using the Lippert-Mataga equation.[31]

$$\Delta v = \left[2\left(\mu_{\mathrm{e}} - \mu_{\mathrm{g}}\right)^2 / hca^3\right]\Delta f + v^0$$

$$\Delta f = [(\varepsilon - 1)/(2\varepsilon + 1)] - [(n^2 - 1)/(2n^2 + 1)]$$

Where Δv is Stokes shift, the superscript "^{0}" indicates the absence of solvent, μ_g and μ_e are dipole moments in the ground state and the excited state, respectively. *h* is the Planck constant, c represents the light speed in vacuum, *a* is Onsager cavity radius, here the value gets from gaussian calculation. ε and *n* are solvent dielectric constant and refractive index respectively.

Table 2. The parameter used to calculate dipole moment change ($\Delta\mu = \mu_{\mathrm{e}} - \mu_{\mathrm{g}}$).

Onsager cavity radius (Å)	Solvents	$\boldsymbol{\Delta v}$	$\boldsymbol{\Delta f}$
5.98	MeCN	2893	0.305
	CH_2Cl_2	2650	0.217
	$CHCl_3$	2620	0.148
	Toluene/CH_2Cl_2 (1:1)	1965	0.080
	Toluene	1341	0.013
	Hexane	1139	0.001

Single crystal X-ray analysis of 9

Slow evaporation using THF solution of **9** at 20 °C afforded single crystals of **9** as red platelets.

The diffraction data for **9** was recorded on a XtaLAB Synergy with a Cu-target (λ = 1.54184 Å) equipped with a Rigaku HyPix-6000HE as the detector at 150 K in house. The diffraction images were processed by using CrysAlisPro.[32] Initial structure was obtained by direct methods (SHELXT-2018/2)[33] and refined by full-matrix least squares calculations on $F2$ (SHELXL-2018/3)[34] using the Olex2[35] program package.

2: $2(C_{28}H_{14}O_5)2(C_4H_8O)$, monoclinic, space group $P2_1/n$ (No. 14), a = 6.97530(10) Å, b = 30.7394(6) Å, c = 22.7853(5) Å, β = 97.729(2)°, V = 4841.16(16) Å^3, ρ_{calcd} = 1.379 g/cm^3, Z = 4, 8614 unique reflections out of 9783 with $I > 2\sigma(I)$, 689 parameters, 3.479°<θ<74.375°, R_1 = 0.1308, wR_2 = 0.4001, GOF = 1.799. CCDC 2232816.

Computational Experiments

All density functional theory (DFT) and time-dependent density functional theory (TDDFT) calculations were performed with Gaussian 16 software package.[36] Geometry optimizations were carried out at the B3LYP level of theory with the 6-311G(d,p) basis set for all atoms. Vibrational frequencies were computed at the B3LYP(D3)/def2-TZVP level of theory with SMD (methanol) to evaluate its zero-point vibrational energy (ZPVE) and thermal corrections at 298 K, and to check whether each optimized structure is an energy minimum or a transition state. Solvation energy corrections were calculated using the SMD model with methanol as the solvent. Multiwfn 3.8 was used to analyze the wave functions.[37] The 3D diagrams of computed species were generated using CYLView.

Synthetic procedure and characterization data

2-bromo-1H-tricyclopenta[def,jkl,pqr]triphenylene-1,4,7-trione (2)

To a CH_2Cl_2 (11 mL) solution of bromosumanene (34.4 mg, 0.10 mmol) in 30 mL round-bottomed flask was added pyridine (1.2 mL, 15.25 mmol), $RuCl_3 \cdot nH_2O$ (85 mg, 0.33 mmol), and a 70% aqueous solution of *t*-BuOOH (1.0 mL, 7.78 mmol) at room temperature. The reaction mixture was warmed to 35 °C. After being stirred for 24 h. The reaction mixture was diluted by CH_2Cl_2 at rt, filtered through silica pad, and evaporated. The residue was purified by PTLC (CH_2Cl_2) to give bromotrioxosumanene **2** (16.6 mg, 43% yield) as an orange solid.

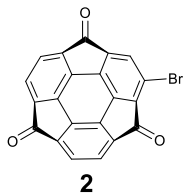

2

2: mp: 267 °C (dec.); TLC: R_f = 0.45 (CH_2Cl_2); ^{1}H NMR (400 MHz, $CDCl_3$) δ (ppm) 7.52 (s, 1H), 7.49 (d, J = 7.4 Hz, 1H), 7.47 (d, J = 7.4 Hz, 1H), 7.46 (d, J = 7.4 Hz, 1H), 7.43 (d, J = 7.3 Hz, 1H); ^{13}C NMR (100 MHz, Chloroform-*d*) δ (ppm) 187.95, 186.95, 185.65, 150.30, 149.82, 149.67, 149.38, 147.83, 147.04, 144.73, 143.87, 143.55, 143.40, 143.37, 140.32, 131.21, 127.21, 127.15, 127.01, 126.78, 121.35. IR (ATR): ν 2974, 2952, 1720, 1636, 1562, 1390, 1366, 1329, 1293, 1266, 1195, 1178, 1073, 947, 857, 842, 774, 734, 723, 697 cm^{-1}; HRMS (EI) *m*/*z* Calcd. for $C_{21}H_5BrO_3$ [M^+]: 383.9422, found 383.9410.

Synthesis of trioxosumanene derivatives **3-7.** To a test tube equipped with a magnetic stir bar was added **2** (0.050 mmol, 1 equiv), organo boronic acid (0.060 mmol, 1.2 equiv), $PdCl_2(amphos)_2$ (0.7 mg, 0.5 μmol, 0.02 equiv), ((tmeda)Zn(OH)(OTf))$_3$ (0.075 mmol/Zn, 1.5 equiv/Zn), and THF (2.0 mL). The reaction mixture was stirred for 1 h at 80 °C and then cooled to room temperature. The mixture was extracted with DCM (ca. 20 mL × 3). The combined organic extract was dried over Na_2SO_4, filtered, and concentrated under reduced

pressure. The residue was purified by PTLC (CH_2Cl_2) to give the corresponding products. Further purification was conducted with GPC by using $CHCl_3$ as an eluent.

2-phenyl-1H-tricyclopenta[def,jkl,pqr]triphenylene-1,4,7-trione (3)

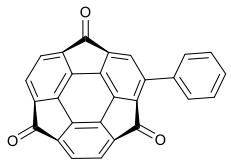

3

3: mp: 312 °C (dec.); TLC: R_f = 0.65 (CH_2Cl_2); ^{1}H NMR (600 MHz, Chloroform-*d*) δ (ppm) 7.63 (s, 1H), 7.63 (m, 2H), 7.49 (m, 3H), 7.45 (d, J = 7.6 Hz, 1H), 7.42 (d, J = 7.4 Hz, 1H), 7.40 (d, J = 7.4 Hz, 1H), 7.35 (d, J = 7.3 Hz, 1H); ^{13}C NMR (100 MHz, Chloroform-*d*) δ (ppm) 188.54, 188.38, 186.91, 150.32, 150.15, 149.92, 149.27, 149.18, 147.42, 144.58, 144.29, 143.97, 143.91, 143.71, 143.44, 138.36, 135.69, 130.06, 129.98, 128.62, 127.18, 126.77, 126.62, 126.48, 126.37. IR (ATR): v 3057, 2961, 2923, 2852, 1717, 1633, 1562, 1450, 1397, 1343, 1262, 1176, 1071, 1027, 950, 908, 853, 742, 729, 693 cm^{-1}; HRMS (EI) *m*/*z* Calcd. for $C_{27}H_{10}O_3$ [M^+]: 382.0630, found 382.0622.

2-(4-nitrophenyl)-1H-tricyclopenta[def,jkl,pqr]triphenylene-1,4,7-trione (4)

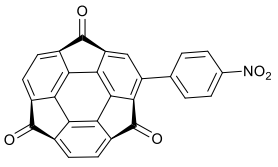

4

4: mp: 344 °C (dec.); TLC: R_f = 0.65 (CH_2Cl_2); ^{1}H NMR (600 MHz, Chloroform-*d*) δ (ppm) 8.35 (d, J = 8.2 Hz, 2H), 7.79 (d, J = 8.3 Hz, 2H), 7.62 (s, 1H), 7.49 (d, J = 7.5 Hz, 1H), 7.46 (d, J = 7.6 Hz, 1H), 7.44 (d, J = 7.6 Hz, 1H), 7.39 (d, J = 7.6 Hz, 1H); ^{13}C NMR (100 MHz, Chloroform-*d*) δ (ppm) 188.08, 187.87, 186.74, 150.05, 149.98, 149.68, 149.50, 149.20, 148.59, 148.50, 143.95, 143.90, 143.88, 143.78, 143.73, 143.64, 141.81, 141.28, 139.05, 130.84, 127.02, 126.99, 126.84, 126.73, 123.84. IR (ATR): v 2959, 2923, 2851, 1718, 1518, 1346, 1259, 1087, 1015, 947, 855, 795, 742, 731, 693 cm^{-1}; HRMS (EI) *m*/*z* Calcd. for $C_{27}H_9NO_5$ [M^+]: 427.0481, found 427.0475.

4-(1,4,7-trioxo-4,7-dihydro-1H-tricyclopenta[def,jkl,pqr]triphenylen-2-yl)benzaldehyde (5)

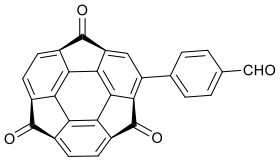

5

5: mp: 323 °C (dec.). TLC: R_f = 0.20 (CH_2Cl_2). ^{1}H NMR (600 MHz, Chloroform-*d*) δ 10.10 (s, 1H), 8.01 (d, *J* = 7.8 Hz, 2H), 7.80 (d, *J* = 7.8 Hz, 2H), 7.65 (s, 1H), 7.47 (d, *J* = 7.5 Hz, 1H), 7.45 (d, *J* = 7.5 Hz, 1H), 7.43 (d, *J* = 7.3 Hz, 1H), 7.38 (d, 7.3 Hz, 1H). ^{13}C NMR (100 MHz, $CDCl_3$) δ (ppm) 191.81, 188.24, 188.05, 186.80, 150.13, 149.96, 149.83, 149.44, 149.21, 148.19, 144.01, 143.90, 143.84, 143.79, 143.58, 142.60, 141.41, 138.90, 136.97, 130.63, 129.86, 127.02, 126.94, 126.87, 126.80, 126.72. IR (ATR): *v* 2955, 2922, 2853, 1717, 1632, 1640, 1567, 1460, 1447, 1396, 1369, 1342, 1285, 1260, 1226, 1196, 1177, 1110, 1053, 1018, 950, 845, 743, 727 cm^{-1}. HRMS (EI) m/z Calcd. for [$C_{28}H_{10}O_4^+$] (M^+): 410.0579, found 410.0583.

2-(4-chlorophenyl)-1H-tricyclopenta[def,jkl,pqr]triphenylene-1,4,7-trione (6)

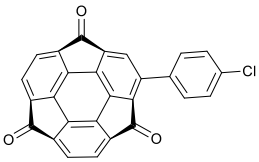

6

6: mp: 333 °C (dec.). TLC: R_f = 0.55 (CH_2Cl_2). ^{1}H NMR (600 MHz, Chloroform-*d*) δ 7.58 (s, 1H), 7.57 (d, *J* = 8.5 Hz, 2H), 7.46 (d, *J* = 8.4 Hz, 2H), 7.45 (d, *J* = 7.7 Hz, 1H), 7.42 (d, *J* = 7.7 Hz, 1H), 7.41 (d, *J* = 7.6 Hz, 1H), 7.37 (d, *J* = 7.6 Hz, 1H). ^{13}C NMR (151 MHz, Chloroform-*d*) δ (ppm) 188.39, 188.19, 186.86, 150.28, 150.04, 149.93, 149.30, 149.13, 147.61, 144.17, 143.91, 143.87, 143.83, 143.50, 143.07, 138.32, 136.37, 134.05, 131.21, 128.93, 126.84, 126.79, 126.72, 126.60, 126.51. IR (ATR): *v* 2956, 2922, 2853, 1716, 1625, 1591, 1485, 1377, 1260, 1177, 1091, 1041, 1013, 947, 854, 831, 745, 731, 696 cm^{-1}. HRMS (EI) m/z Calcd. for [$C_{27}H_9ClO_3^+$] (M^+): 416.0240, found 416.0248.

2-(thiophen-2-yl)-1H-tricyclopenta[def,jkl,pqr]triphenylene-1,4,7-trione (7)

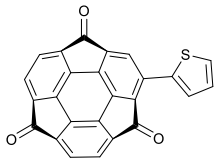

7

7: mp: 345 °C (dec.). TLC: R_f = 0.45 (CH_2Cl_2). ^{1}H NMR (600 MHz, Chloroform-*d*) δ 8.03 (d, *J* = 3.7 Hz, 1H), 7.70 (s, 1H), 7.50 (d, *J* = 4.9 Hz, 1H), 7.45 (d, *J* = 7.9 Hz, 1H), 7.43 (d, *J* = 7.9 Hz, 1H), 7.42 (d, *J* = 7.5 Hz, 1H), 7.40 (d, *J* = 7.4 Hz, 1H), 7.23 (dd, *J* = 4.9, 3.7 Hz, 1H). ^{13}C NMR (151 MHz, Chloroform-*d*) δ (ppm) 188.54, 188.06, 186.70, 151.09, 150.28, 150.12, 149.78, 148.98, 148.74, 148.52, 146.08, 143.98, 143.86, 143.33, 138.85, 137.01, 136.13, 132.57, 129.07, 128.70, 126.86, 126.75, 126.52, 126.48,126.15. IR (ATR): *v* 2953, 2923, 2852, 1717, 1558, 1420, 1283, 1261, 1196, 1177, 1126, 1049, 949, 844, 791, 744, 725, 693 cm^{-1}. HRMS (EI) m/z Calcd. for [$C_{25}H_8O_3S^+$] (M^+): 388.0194, found 388.0189.

2-(2-hydroxyphenyl)-1H-tricyclopenta[def,jkl,pqr]triphenylene-1,4,7-trione (8)

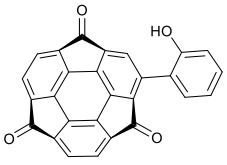

8

8: TLC: R_f = 0.15 (CH_2Cl_2).^{1}H NMR (400 MHz, DMSO-d_6) δ (ppm) 9.84 (s, 1H), 7.60 (s, 1H), 7.49 (d, *J* = 7.5 Hz, 1H), 7.44 (d, *J* = 7.5 Hz, 2H), 7.37 (d, *J* = 7.2 Hz, 1H), 7.31 (dd, *J* = 7.6, 1.8 Hz, 1H), 7.27 (ddd, *J* = 7.6, 7.6, 1.8 Hz, 1H), 6.95 (dd, *J* = 7.7, 1.3 Hz, 1H), 6.87 (ddd, *J* = 7.6, 7.6, 1.3 Hz, 1H). IR (ATR): *v* 2959, 2920, 2853, 1719, 1456, 1274, 1187, 1123, 1070, 1037, 938, 854, 827, 798, 742 cm^{-1}. HRMS (EI) m/z Calcd. for [$C_{27}H_{10}O_4^+$] (M^+): 398.0579, found 398.0561.

Preparation of ring-opened compound **9.** To a test tube equipped with a magnetic stir bar was added crude **8** (10.0 mg, 0.025 mmol) in a 10 mL mixture of THF/MeOH (1:9) solution at 27 °C. After 1 minute of stirring, the reaction mixture color changed from red to yellow. After the removal of solvent under the reduced pressure, the residue was washed with chloroform and then was purified by PTLC (THF:CH_2Cl_2=1:19) to give **9** (5.1 mg, 47% yield) as an orange solid.

Methyl-6-(2-hydroxyphenyl)-1,8-dioxo-1,8-dihydrodicyclopenta[def,jkl]triphen-ylene-4-

carboxylate (9)

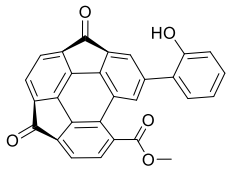

9

9: mp: 223 °C (dec.). TLC: R_f = 0.45 (THF:CH_2Cl_2=1:19). ^{1}H NMR (600 MHz, THF-d_8) δ 8.82 (s, 1H), 8.60 (s, 1H), 8.11 (s, 1H), 8.07 (d, *J* = 7.5 Hz, 1H), 7.86 (d, *J* = 7.3 Hz, 1H), 7.77 (d, *J* = 7.2 Hz, 1H), 7.75 (d, *J* = 7.0 Hz, 1H), 7.43 (dd, *J* = 7.5, 1.6 Hz, 1H), 7.21 (td, *J* = 7.5, 1.8 Hz, 1H), 6.97 (td, *J* = 7.4, 0.9 Hz, 1H), 6.92 (dd, *J* = 8.1, 0.8 Hz, 1H), 4.05 (s, 3H). ^{13}C NMR (151 MHz, THF-d_8) δ 191.39, 190.83, 169.14, 155.66, 142.99, 140.14, 138.75, 138.42, 137.48, 136.93, 136.58, 136.20, 135.68, 134.88, 133.43, 131.97, 130.08, 129.72, 129.69, 127.65, 126.77, 126.52, 126.22, 125.48, 124.05, 121.01, 117.11, 53.23. IR (ATR): *v* 3423, 2953, 2928, 2856, 1714, 1632, 1601, 1453, 1369, 1337, 1267, 1185, 1101, 1036, 907, 857, 808, 755, 727 cm^{-1}. HRMS (EI) m/z Calcd. for [$C_{28}H_{14}O_5^+$] (M^+): 430.0841, found 430.0855.

^{1}H and ^{13}C NMR spectra of **2**

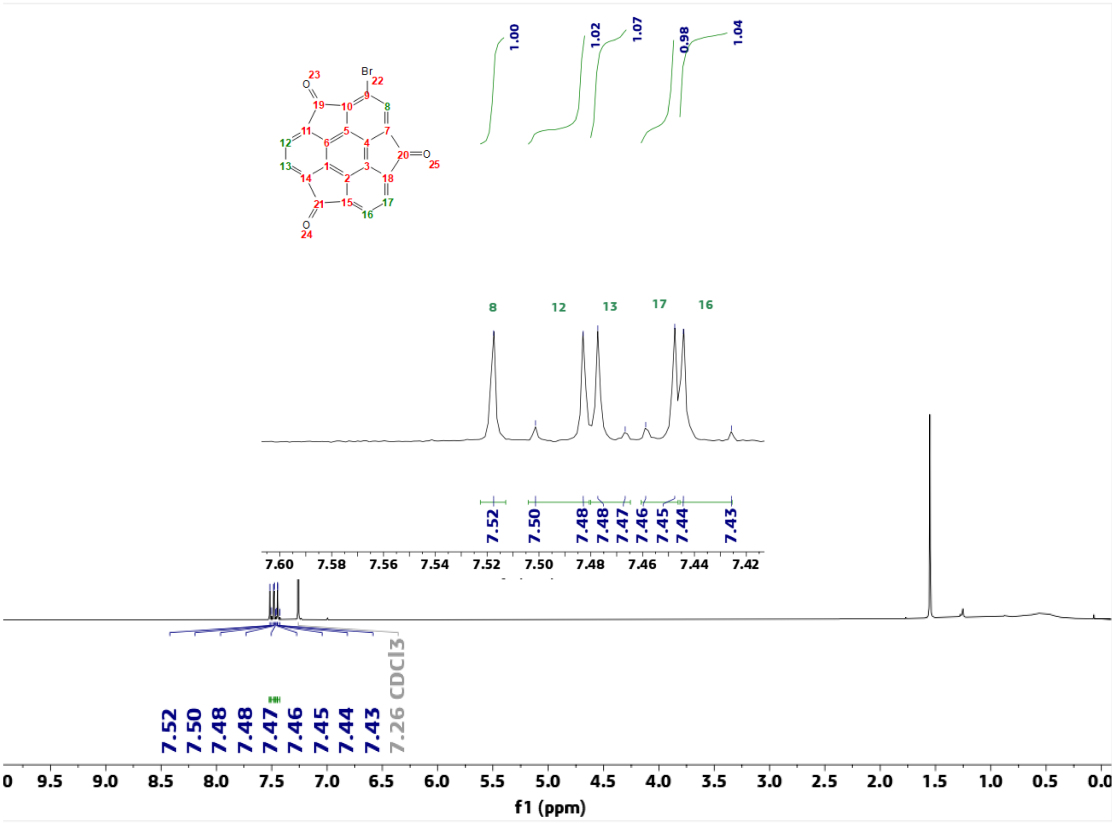

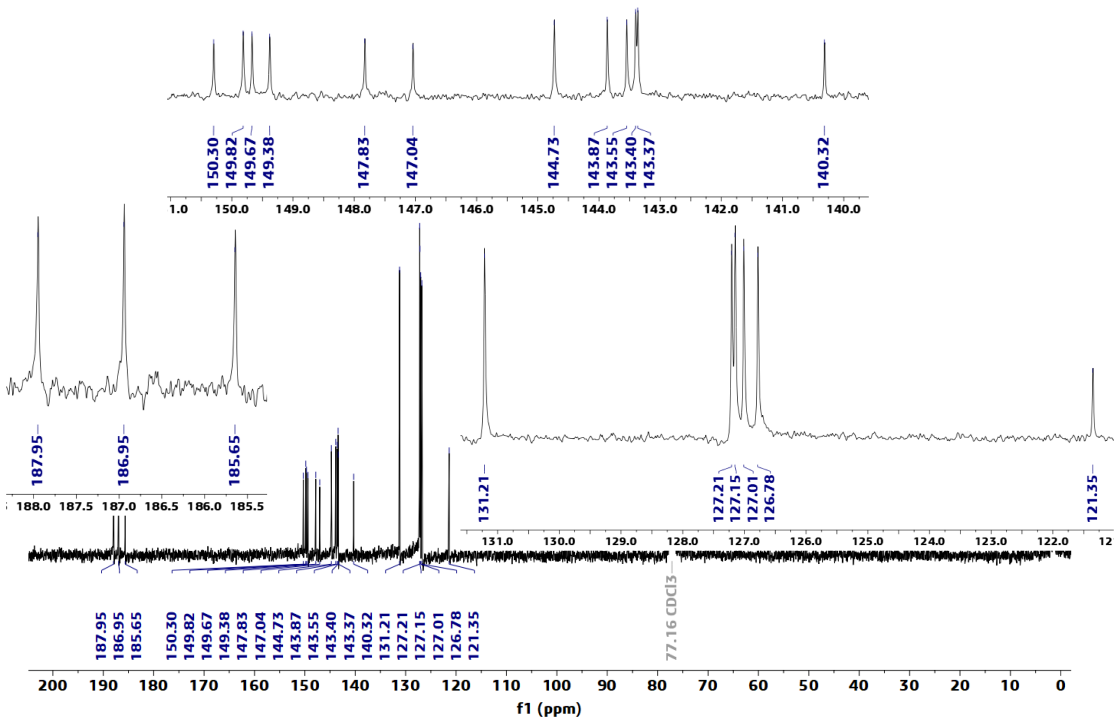

^{1}H and ^{13}C NMR spectra of **3**

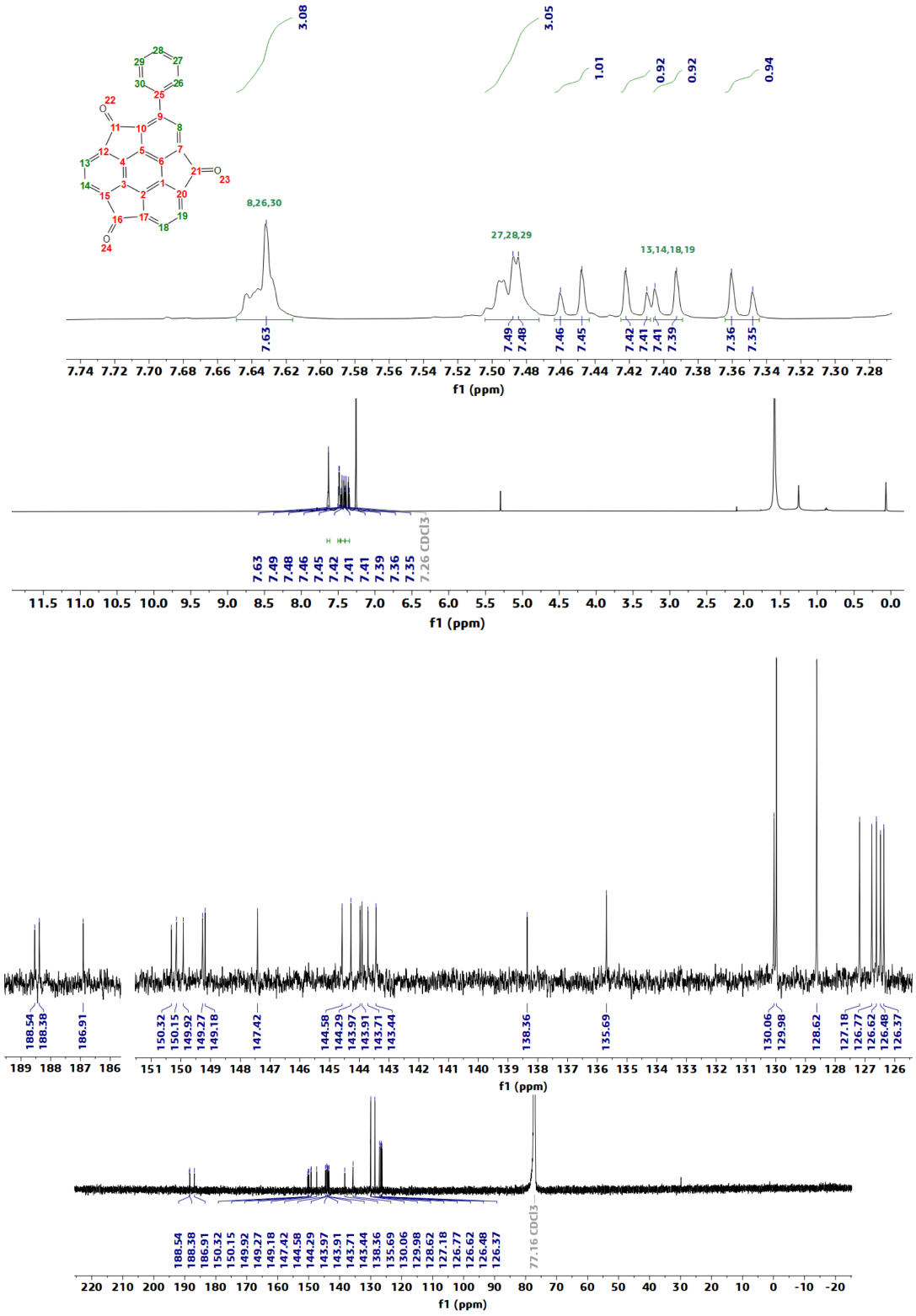

^{1}H and ^{13}C NMR spectra of **4**

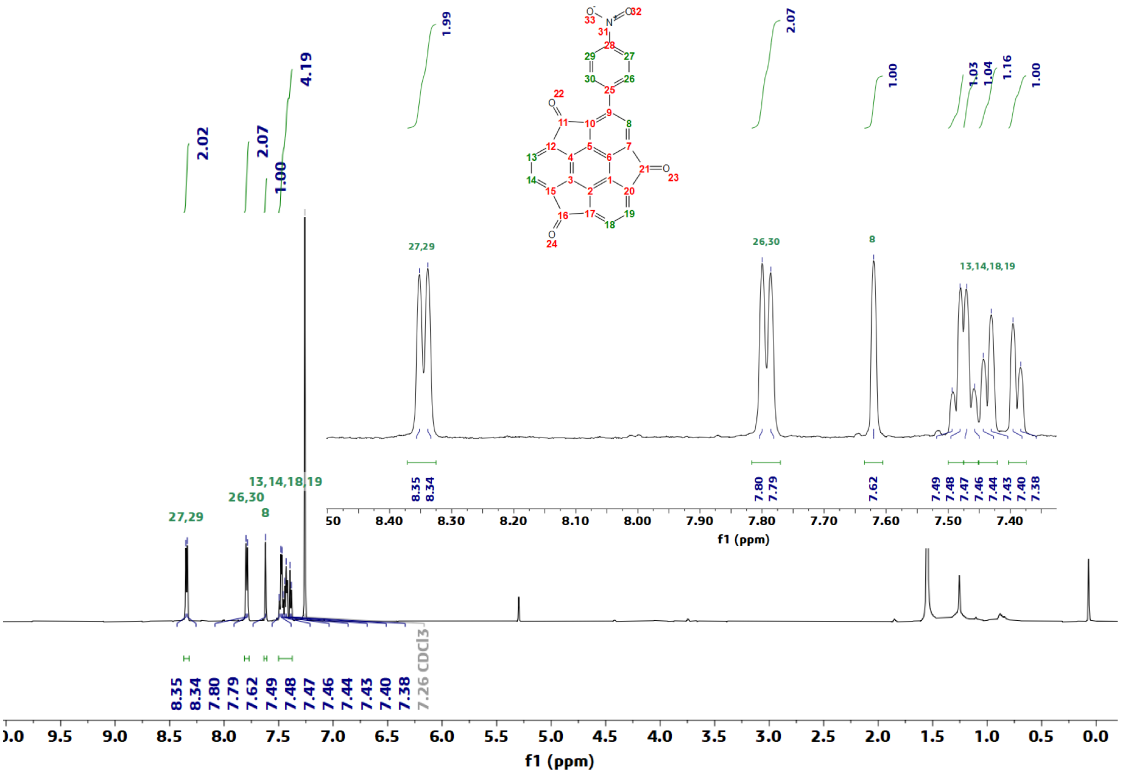

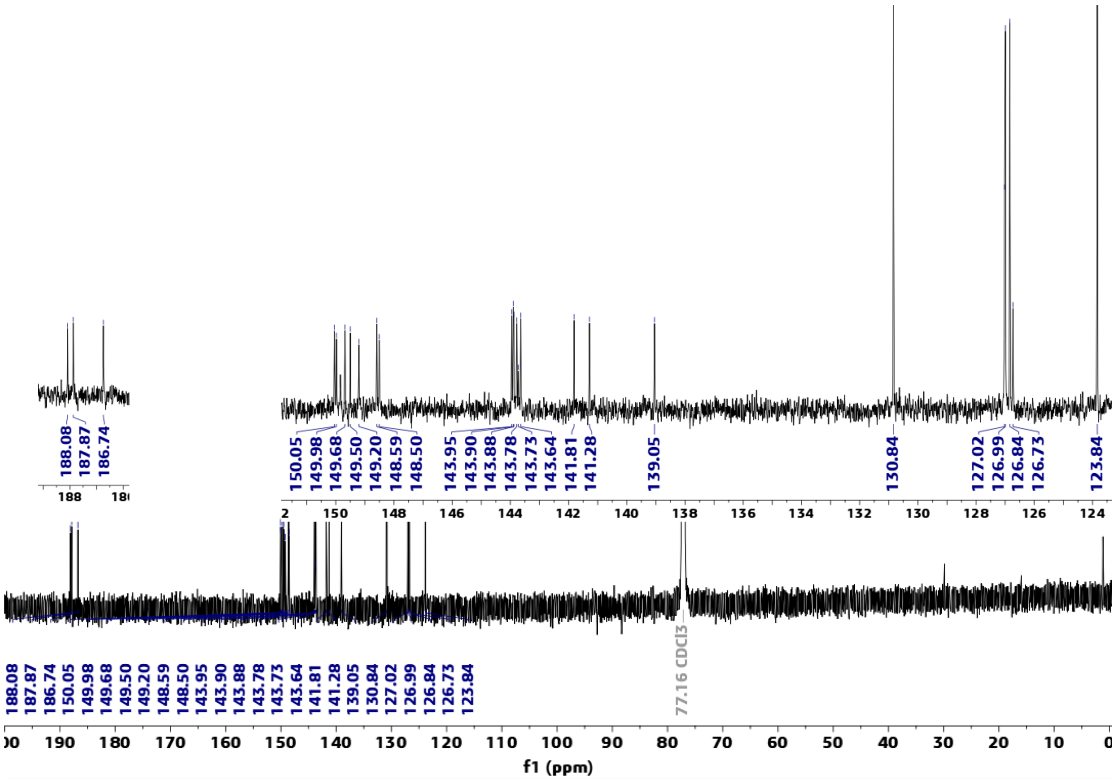

^{1}H and ^{13}C spectra of **5**

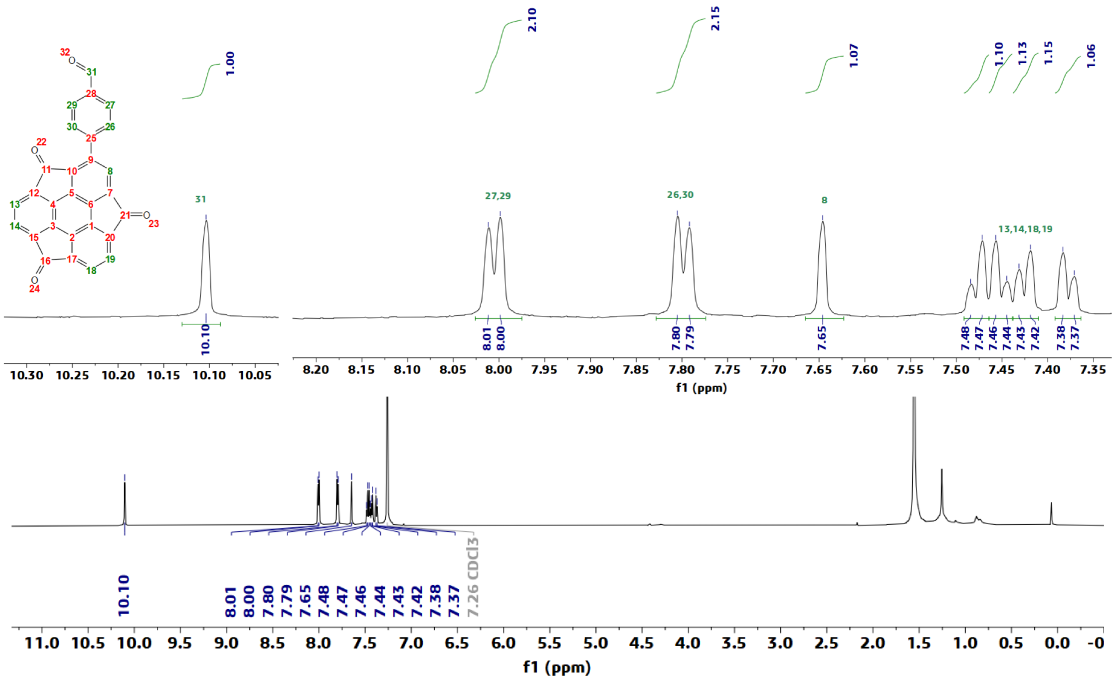

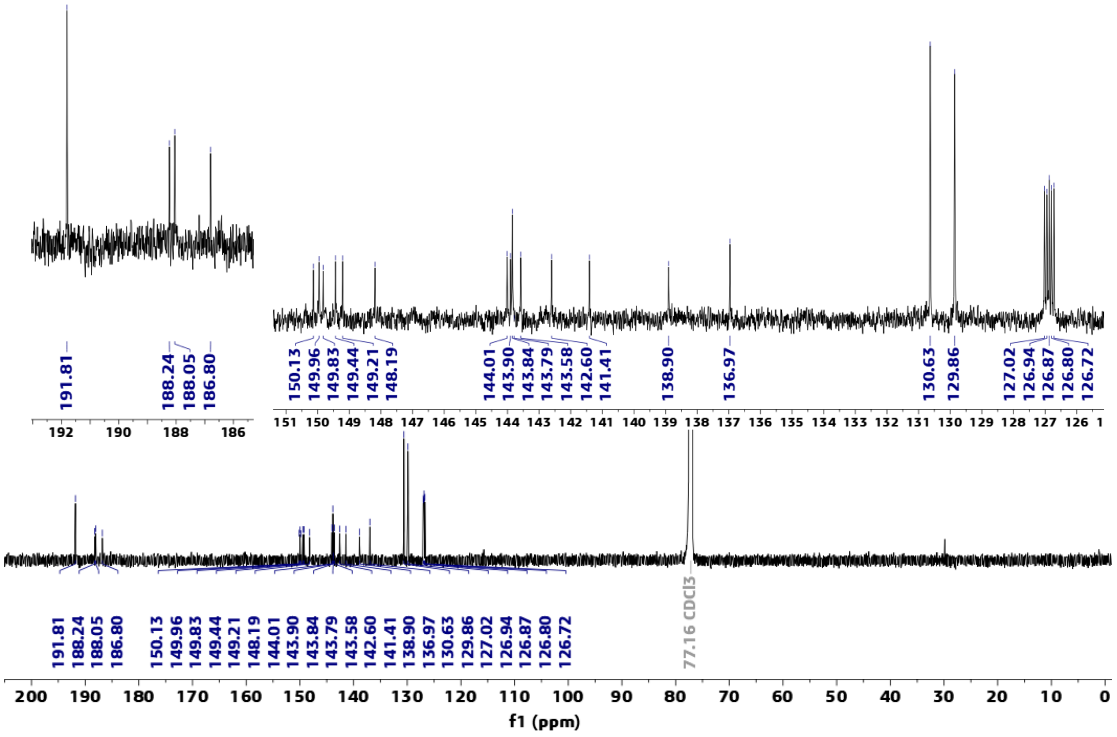

^{1}H and ^{13}C NMR spectra of **6**

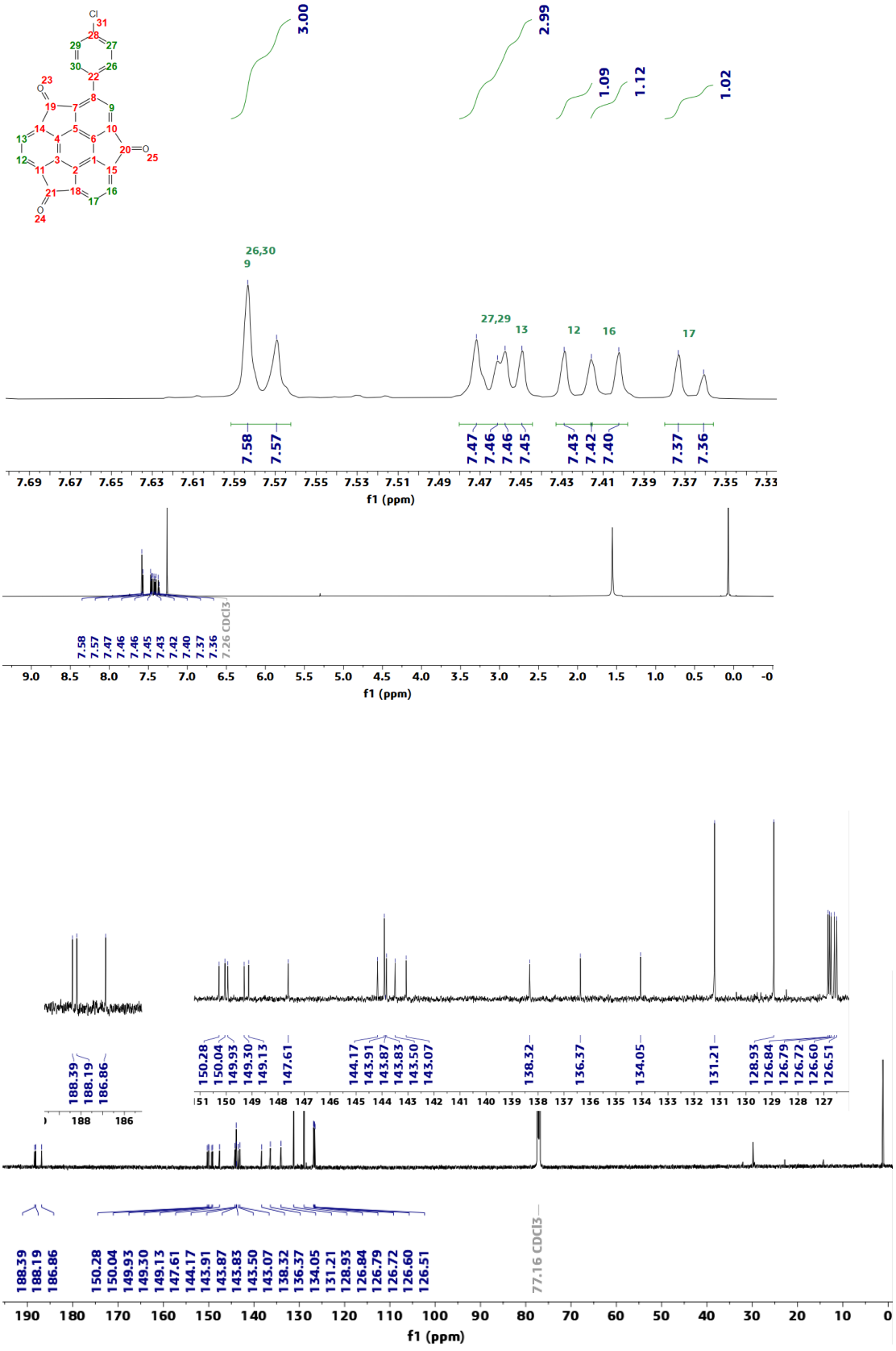

^{1}H and ^{13}C NMR spectra of **7**

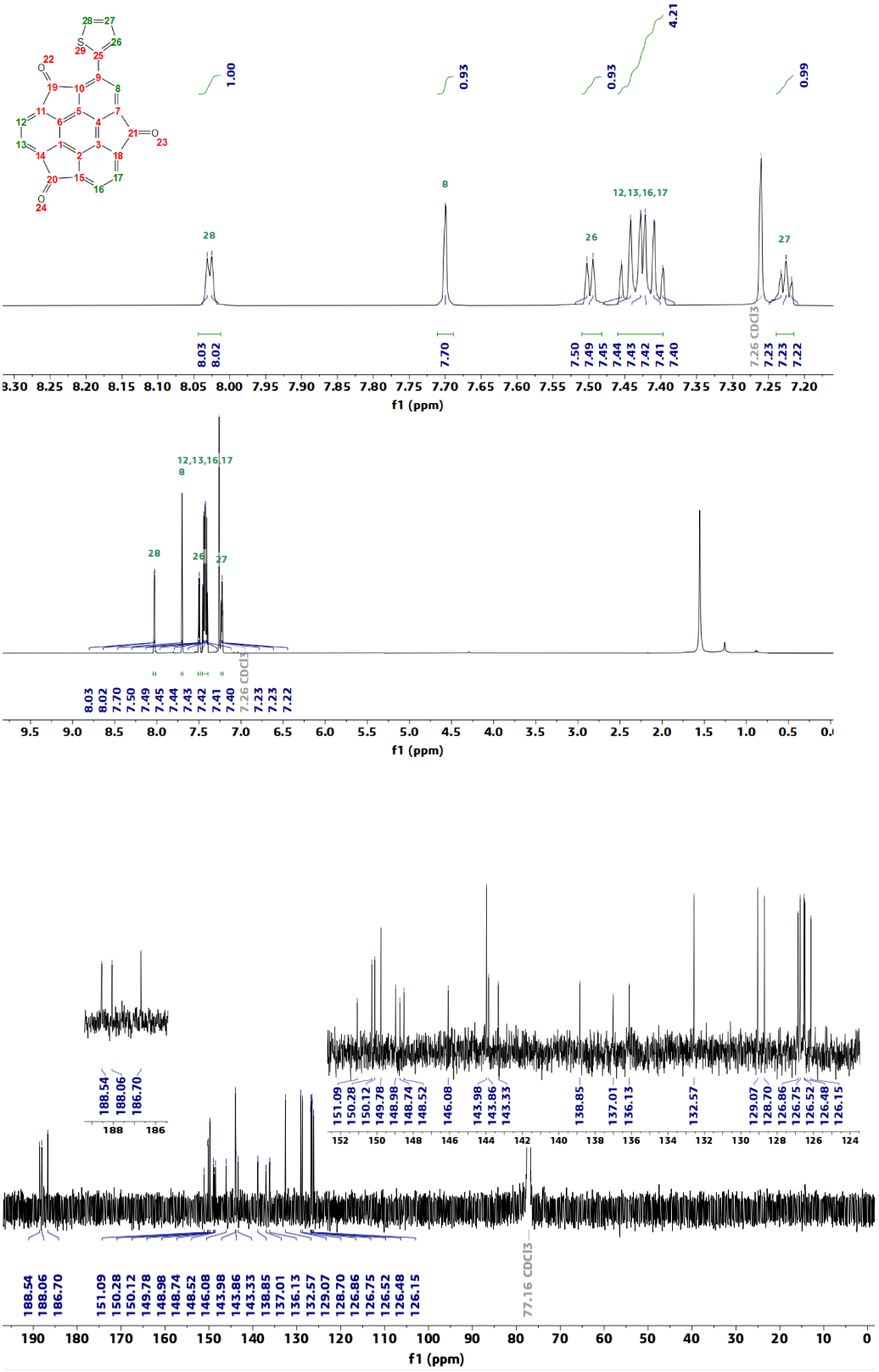

^{1}H and ^{13}C NMR spectra of **8**

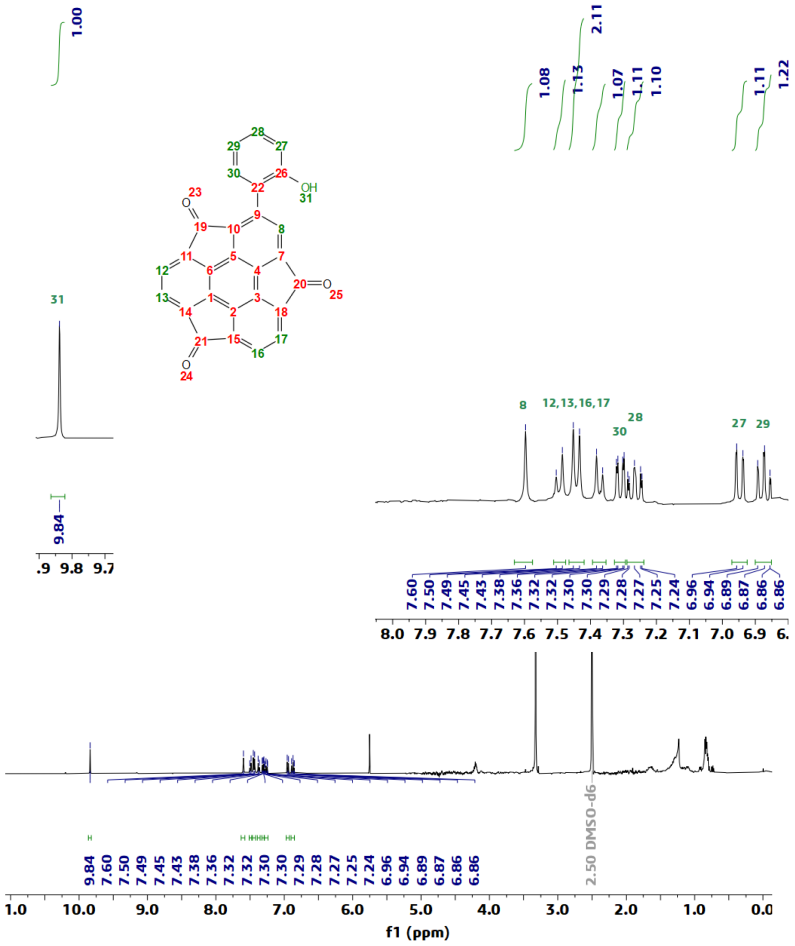

COSY NMR spectrum of **8**

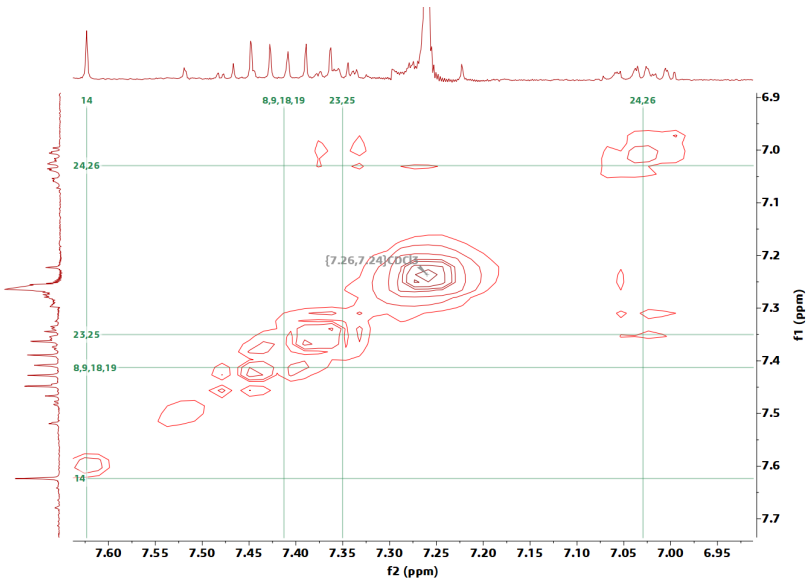

^{1}H and ^{13}C NMR spectrum of **9**

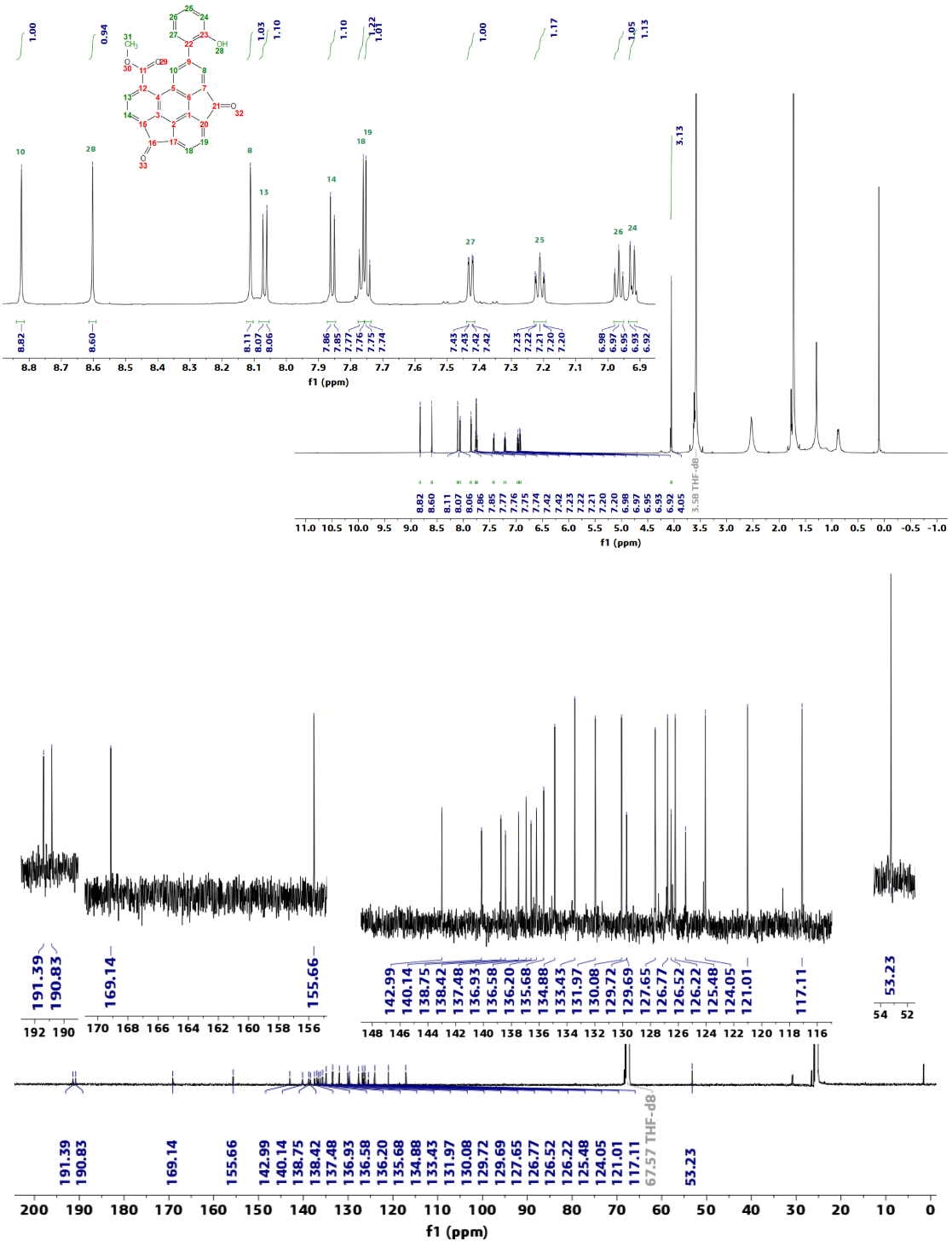

References

1. T. Amaya, M. Hifumi, M. Okada, Y. Shimizu, T. Moriuchi, K. Segawa, Y. Ando and T. Hirao, *J. Org. Chem.*, 2011, **76**, 8049.
2. S. Higashibayashi, B. B. Shrestha, Y. Morita, M. Ehara, K. Ohkubo, S. Fukuzumi and H. Sakurai, *Chem. Lett.*, 2014, **43**, 1297.
3. C. Mutzel, J. M. Farrell, K. Shoyama and F. Wurthner, *Angew Chem Int Ed Engl*, 2022, **61**, e202115746.
4. N. A. Kukhta, D. Volyniuk, J. V. Grazulevicius and G. Sini, *J. Mater. Chem. C*, 2018, **6**, 1679.
5. D. A. Heredia, A. M. Durantini, J. E. Durantini and E. N. Durantini, *J. Photochem. Photobiol., C*, 2022, **51**.
6. K. Kanahara, M. D. M. R. Badal, S. Hatano, M. Abe, S. Higashibayashi, N. Takashina and H. Sakurai, *Bull. Chem. Soc. Jpn.*, 2015, **88**, 1612.
7. S. E. Koops, B. C. O'Regan, P. R. Barnes and J. R. Durrant, *J. Am. Chem. Soc.*, 2009, **131**, 4808.
8. H. F. Higginbotham, M. Okazaki, P. de Silva, S. Minakata, Y. Takeda and P. Data, *ACS Appl. Mater. Interfaces*, 2021, **13**, 2899.
9. T. Hosono, N. O. Decarli, P. Z. Crocomo, T. Goya, L. E. de Sousa, N. Tohnai, S. Minakata, P. de Silva, P. Data and Y. Takeda, *J. Mater. Chem. C*, 2022, **10**, 4905.
10. B. M. Schmidt, B. Topolinski, S. Higashibayashi, T. Kojima, M. Kawano, D. Lentz and H. Sakurai, *Chem.–Eur. J*, 2013, **19**, 3282.
11. M. Li, J. Wu, K. Sambe, Y. Yakiyama, T. Akutagawa, T. Kajitani, T. Fukushima, K. Matsuda and H. Sakurai, *Mater. Chem. Front.*, 2022, **6**, 1752.
12. M. Li, X. Chen, Y. Yakiyama, J. Wu, T. Akutagawa and H. Sakurai, *Chem. Commun.*, 2022,

58, 8950.

13. R. Tsuruoka, S. Higashibayashi, T. Ishikawa, S. Toyota and H. Sakurai, *Chem. Lett.*, 2010, **39**, 646.
14. T. Amaya, S. Seki, T. Moriuchi, K. Nakamoto, T. Nakata, H. Sakane, A. Saeki, S. Tagawa and T. Hirao, *J. Am. Chem. Soc.*, 2009, **131**, 408.
15. S. R. Joo, G. T. Kwon and S. H. Kim, *Asian J. Org. Chem.*, 2020, **9**, 584.
16. A. N. Cammidge, V. H. M. Goddard, H. Gopee, N. L. Harrison, D. L. Hughes, C. J. Schubert, B. M. Sutton, G. L. Watts and A. J. Whitehead, *Org. Lett.*, 2006, **8**, 4071.
17. Y. Yamamoto, M. Takizawa, X.-Q. Yu and N. Miyaura, *Angew. Chem.*, 2008, **120**, 942.
18. T. Niwa, Y. Uetake, M. Isoda, T. Takimoto, M. Nakaoka, D. Hashizume, H. Sakurai and T. Hosoya, *Nat. Catal.*, 2021, **4**, 1080.
19. Y. Morita, S. Nakao, S. Haesuwannakij, S. Higashibayashi and H. Sakurai, *Chem. Commun.*, 2012, **48**, 9050.
20. E. v. Lippert, *Z. Elektrochem. Ber. Bunsenges. Phys. Chem.*, 1957, **61**, 962.
21. N. Mataga, Y. Kaifu and M. Koizumi, *Bull. Chem. Soc. Jpn.*, 1956, **29**, 465.
22. Y. Gao, S. Zhang, Y. Pan, L. Yao, H. Liu, Y. Guo, Q. Gu, B. Yang and Y. Ma, *Phys. Chem. Chem. Phys.*, 2016, **18**, 24176.
23. S. Zhang, L. Yao, Q. Peng, W. Li, Y. Pan, R. Xiao, Y. Gao, C. Gu, Z. Wang and P. Lu, *Adv. Funct. Mater.*, 2015, **25**, 1755.
24. A. Kasprzak, A. Kowalczyk, A. Jagielska, B. Wagner, A. M. Nowicka and H. Sakurai, *Dalton Trans*, 2020, **49**, 9965.
25. A. Kasprzak and H. Sakurai, *Dalton Trans.*, 2019, **48**, 17147.
26. A. Kasprzak and H. Sakurai, *Chem Commun (Camb)*, 2021, **57**, 343.

27. A. Kasprzak, A. Tobolska, H. Sakurai and W. Wroblewski, *Dalton Trans.*, 2022, **51**, 468.

28. E. R. Andrews, R. W. Fleming, J. M. Grisar, J. C. Kihm, D. L. Wenstrup and G. D. Mayer, *J. Med. Chem.*, 1974, **17**, 882.

29. L. Ge, C. Zhang, C. Pan, D. X. Wang, D. Y. Liu, Z. Q. Li, P. Shen, L. Tian and C. Feng, *Nat. Commun.*, 2022, **13**, 5938.

30. J. Turkowska, J. Durka and D. Gryko, *Chem. Commun.*, 2020, **56**, 5718.

31. B. Bagchi, D. W. Oxtoby and G. R. Fleming, *Chem. Phys.*, 1984, **86**, 257.

32. O. Rigaku and P. CrysAlis, *Yarnton, England*, 2015.

33. G. M. Sheldrick, *Acta Crystallogr. A*, 2015, **71**, 3.

34. G. Sheldrick, *Sect. C: Struct. Chem.*, 2015, **71**, 3.

35. O. Dolomanov, L. Bourhis, R. Gildea, J. Howard and H. Puschmann, *J. Appl. Cryst*, 2009, **42**, 339.

36. M. J. Frisch, G. W. Trucks, H. B. Schlegel, G. E. Scuseria, M. A. Robb, J. R. Cheeseman, G. Scalmani, V. Barone, G. A. Petersson, H. Nakatsuji, X. Li, M. Caricato, A. V. Marenich, J. Bloino, B. G. Janesko, R. Gomperts, B. Mennucci, H. P. Hratchian, J. V. Ortiz, A. F. Izmaylov, J. L. Sonnenberg, Williams, F. Ding, F. Lipparini, F. Egidi, J. Goings, B. Peng, A. Petrone, T. Henderson, D. Ranasinghe, V. G. Zakrzewski, J. Gao, N. Rega, G. Zheng, W. Liang, M. Hada, M. Ehara, K. Toyota, R. Fukuda, J. Hasegawa, M. Ishida, T. Nakajima, Y. Honda, O. Kitao, H. Nakai, T. Vreven, K. Throssell, J. A. Montgomery Jr., J. E. Peralta, F. Ogliaro, M. J. Bearpark, J. J. Heyd, E. N. Brothers, K. N. Kudin, V. N. Staroverov, T. A. Keith, R. Kobayashi, J. Normand, K. Raghavachari, A. P. Rendell, J. C. Burant, S. S. Iyengar, J. Tomasi, M. Cossi, J. M. Millam, M. Klene, C. Adamo, R. Cammi, J. W. Ochterski, R. L. Martin, K. Morokuma, O. Farkas, J. B. Foresman and D. J. Fox.*Journal*, 2016.

37. T. Lu and F. Chen, *J. Comput. Chem.*, 2012, **33**, 580.

Chapter 4. High quantum yield NIR emission via charge transfer states in Buckybowl-TPA based D–A systems

Section 1. Design strategies and functional significance of NIR dyes

Near-infrared (NIR) dyes have garnered significant attention due to their vast array of applications in solar cells,[1] organic light-emitting diodes (OLEDs),[2] organic field-effect transistors (OFETs),[3] and various biochemical fields.[4] Beyond optoelectronics, NIR dyes have proven highly effective in tissue imaging and photopharmacology, owing to the minimal absorption and autofluorescence of biological tissues in the NIR range (700–1000 nm).[5, 6] The design strategy for organic NIR dyes typically revolves around the Donor-π-Acceptor (D-π-A) paradigm, which facilitates intramolecular charge transfer (ICT) by modulating the frontier orbital energies−destabilizing the HOMO of the donor and stabilizing the LUMO of the acceptor−to precisely tune the energy gap between the ground and excited states.[7] Numerous factors influence the photophysical behavior of such systems, including the nature and arrangement of electron-rich and electron-deficient chromophores, the functionalization and conjugation style of linkers bridging donor and acceptor units, their spatial distance, and environmental conditions. The efficiency and dynamics of charge transfer are largely governed by electronic coupling and solvent polarity: stronger electronic coupling promotes orbital overlap and enhances CT character, while polar solvents stabilize the CT state via dielectric screening, increasing the population of CT species.

Over the years, various π-conjugated charge transfer molecules and polymers have been developed for NIR applications such as LEDs and in vivo imaging. These materials often employ well-known strong electron acceptors, including benzothiadiazole (BT),[8]

benzobisthiadiazole (BBT),[9] thiadiazoloquinoxaline (TQ),[10] triazolobenzothiadiazole (BTT),[11] diketopyrrolopyrrole (DPP),[12] thienopyrroledione (TPD),[13] and boron-dipyrromethene (BODIPY).[14] However, achieving strong NIR emission typically requires complex architectures involving multiple donor components, which can complicate synthesis and limit practical applications.

In chapter 3, trioxosumanene (**TOS**), promising multistep electron acceptor due to its exceptional electron-withdrawing capability, with reduction potentials surpassing those of fullerene derivatives (Figure 1).[15, 16] Interestingly, **TOS** displays such pronounced electron-accepting properties that even strongly electron-deficient groups like nitrophenyl can function as donors when paired with it.[17] Additionally, as a typical $\pi\pi^*$ triplet molecule, **TOS** exhibits rapid intersystem crossing (ISC) from the triplet state to the ground state (S_0), facilitated by a large spin-orbit coupling (SOC) due to its curved, non-planar structure.[18] These unique features make **TOS** highly attractive for applications in electron injection and the development of organic phosphorescent materials.

In this chapter, the author presents the design and synthesis of **TPA-TOS**, a **TOS**-based donor-acceptor NIR dye with a distinctive molecular architecture (Figure 1). Featuring the bulky triphenylamine (**TPA**) group as the donor and **TOS** as the acceptor, the system achieves efficient intramolecular charge transfer (ICT), resulting in a narrowed bandgap and weak absorption extending into the NIR range up to 850 nm. Remarkably, **TPA-TOS** demonstrated an impressive quantum yield exceeding 60% in non-polar solvents such as hexane, with strong NIR emission spanning the 650–850 nm range. Femtosecond transient absorption spectroscopy (fsTA), electron spin resonance (ESR), and density functional theory (DFT) calculations suggest that the emission arises from thermally

activated delayed fluorescence (TADF) and room-temperature phosphorescence (RTP), accompanied by partial charge separation. Furthermore, **TPA-TOS** exhibited distinct solvent dependency, showing negligible emission in polar solvents like acetonitrile (MeCN). With its unique mechanism and simplified donor-acceptor architecture, **TPA-TOS** paves the way for the development of efficient NIR dyes and highlights the tremendous potential of bowl-shaped molecular frameworks for advanced optoelectronic and biomedical applications.

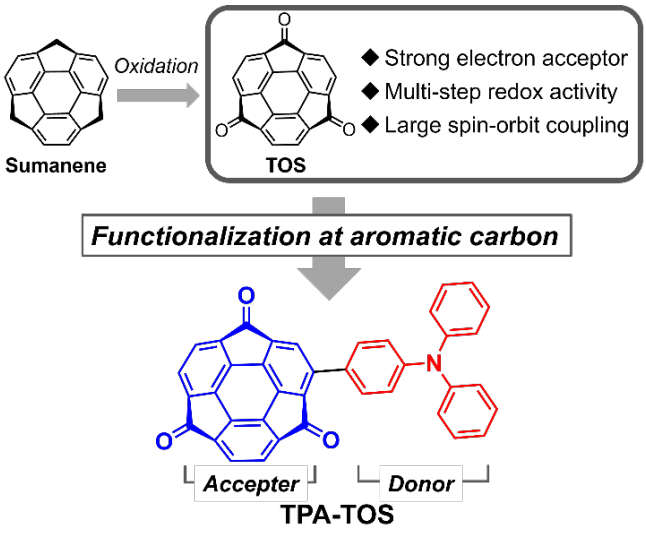

Figure 1. The features and the schematic drawing of **TPA-TOS**

Section 2. Synthesis and characterization of TPA-TOS

Figure. 2A illustrates the synthetic route to **TPA-TOS**. Bromotrioxosumanene (**TOS-Br**) was found to be a versatile precursor for obtaining various **TOS** derivatives[17] via an acidic Suzuki-Miyaura coupling reaction,[19] which avoids the basic conditions, under which the sumanene skeleton is relatively unstable. Resulting **TPA-TOS** was obtained as a dark-green solid and its structure was characterized by high-resolution mass spectrometry (HRMS) and ^{1}H and ^{13}C NMR spectroscopy.

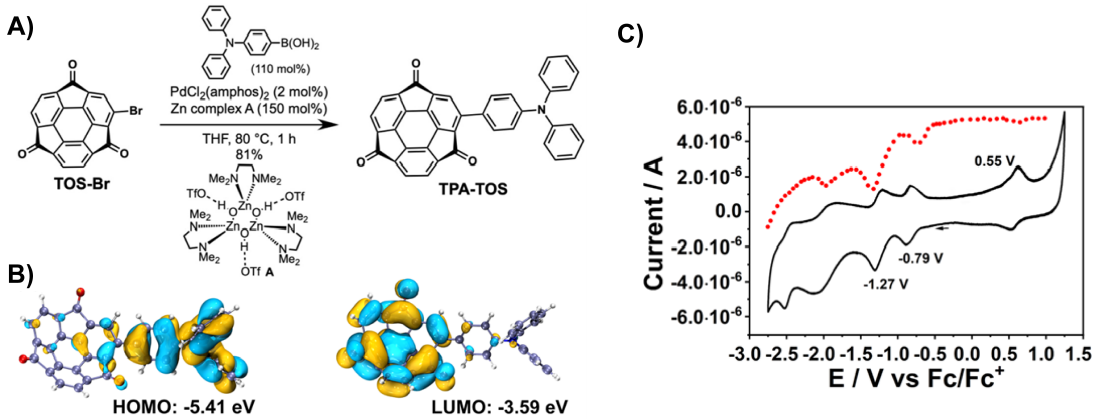

Figure 2. Basic properties of **TPA-TOS**. (A) Synthetic procedure of **TPA-TOS**. (B) HOMO and LUMO distribution of **TAP-TOS** calculated at B3LYP/6-311+G(d,p) level. (C) Redox properties evaluated by cyclic voltammetry (solid black line) and differential pulse voltammetry (red dotted line) of 1 mM of **TPA-TOS** (10^{-3} M, vs. Fc/Fc+) in 0.1 M Bu_4NClO_4 in MeCN electrolyte at the scan rate of 100 mV/s

Although TPA-TOS had strong electron- accepting and electron-donating groups, resulting in a low HOMO-LUMO gap (1.809 eV at B3LYP/6-311+G(d,p)), it was stable under air and underwent only partial decomposition even at 400 °C. Interestingly, TPA-TOS was soluble not only in polar solvents such as MeCN and EtOH, but also in non-polar solvents such as hexane. This was probably attributed to the curved structure of TOS moiety, in which partial dipole generates along the out of the plane direction of the bowl. Such carbon rich molecular skeleton with polarity realized the amphiphilic nature of TPA-TOS. Tremendous amounts of trials to get single crystals of TPA-TOS did not work to afford high quality crystal enough for single crystal X-ray diffraction analysis. Probably large TPA moiety disturbed the effective stacking formation of TOS moiety, giving only small low-quality crystals. Based on the author previous studies, once the bowl-shaped molecule transforms into a quasi-planar configuration, it readily forms high-quality single crystals suitable for structure determination

by single-crystal X-ray diffraction.[17]

The electronic properties of TPA-TOS were next investigated. Density functional theory (DFT) calculations revealed that the HOMO was primarily localized on the TPA moiety, while the LUMO resided on the TOS skeleton, with slight orbital overlaps within each segment (Figure. 2B). Cyclic voltammetry (CV) and differential pulse voltammetry (DPV) measurements in MeCN containing 0.1 M of Bu_4NClO_4 as an electrolyte under a nitrogen atmosphere exhibited two distinct reversible reduction peaks at −0.79 V and −1.27 V at a scan rate of 10 mV/s (Figure. 2C). This implied a strong electron-accepting ability of TPA-TOS reaching C_{60} as confirmed in TOS (−0.92 V and −1.43 V in THF).[15, 19] Meanwhile, the observed oxidation peak of TPA-TOS at +0.55 V indicated the slightly lower donating ability of the TPA part on TPA-TOS than the unmodified TPA (+0.58 V in MeCN)[20] due to the conjugation with electron-accepting TOS. Both HOMO and LUMO energy level were calculated from the onset potentials (E_{onset}) to be −4.0 and −5.5 eV, respectively.[21] These values were in good agreement with the DFT-calculated values.

Section 3. Spectroscopic analyses

To gain insight into the fundamental optical properties of **TPA-TOS**, both absorption and fluorescence spectra were measured (Figure 3AB, Table 1). The acceptor unit, **TOS**, exhibited short-wavelength absorption in the UV region, characterized by an absorption coefficient (ε) of 1.0×10^4 $M^{-1}cm^{-1}$ at 300 nm (Table 1). In contrast, **TPA-TOS** displayed distinct and intense absorption bands between 300–450 nm (ε = 7.6×10^4 $M^{-1}cm^{-1}$ at 300 nm in acetonitrile), along with a prominent absorption band spanning 600–800 nm (ε = 1.2×10^4 $M^{-1}cm^{-1}$ at 685 nm in MeCN).

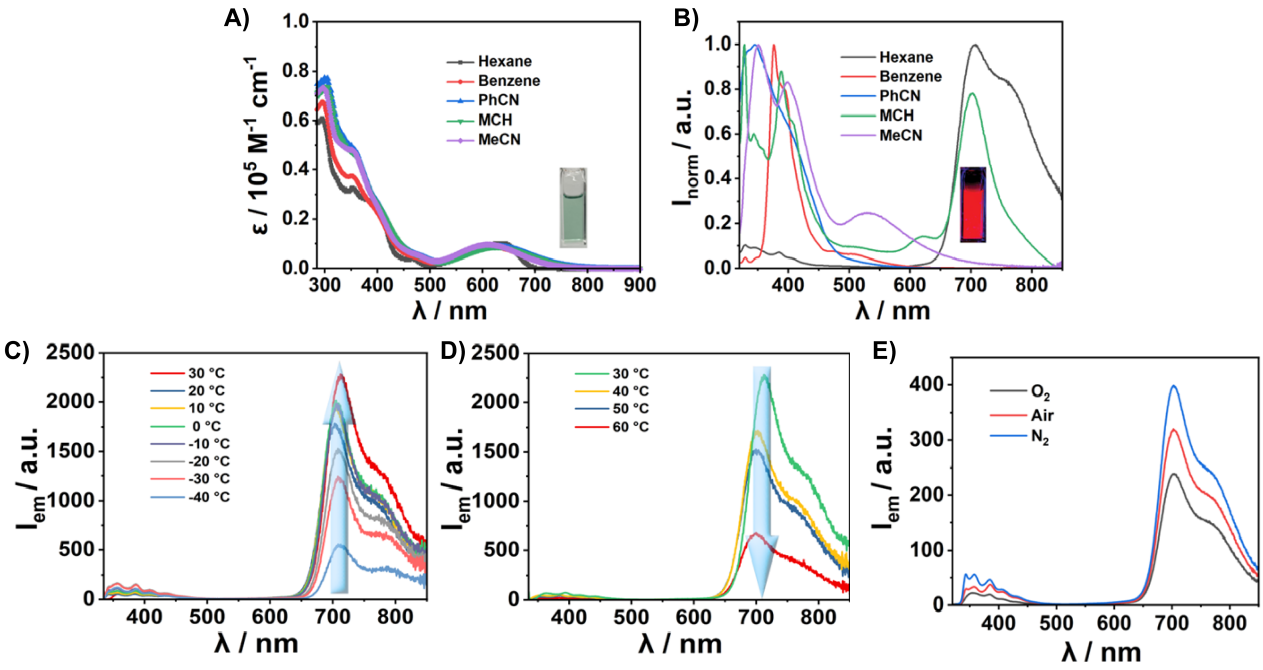

Figure 3. Optical properties of TPA-TOS. (A) UV−vis-NIR absorption spectra of **TPA-TOS** in various solvents (c = 1.0 × 10^{-5} M). The inset photo was taken under general room light. (B) Photoluminescence spectra (λ_{ex} = 300 nm) of **TPA-TOS** in diluted solutions (c = 1.0 × 10^{-5} M). The inset photo was taken under a UV lamp (365 nm) in hexane at dark. Intensity is normalized at the wave length with the highest peak intensity. (C-D) Temperature-dependent photoluminescence spectra (λ_{ex} = 300 nm) of **TPA-TOS** (c = 1.0 x 10^{-5} M) in hexane (C) from −40 °C to 30 °C and (D) from 30 °C to 60 °C. (E) Effect of outer atmosphere on long wavelength emission of **TPA-TOS** at 300 K. PhCN: benzonitril, MCH: methylcyclohexane.

Computational results showed excellent agreement with the experimental data, indicating that the 600–800 nm absorption arises from charge transfer (CT) transitions between the donor (**TPA**) and the acceptor (**TOS**), while the 300–450 nm band corresponds to hybridized local excitation (π–π* transition) (Figure 4). The photoluminescence (PL) spectrum of **TPA-TOS** in polar solvents closely resembled that of **TOS**, with a principal emission peak at 350–450

nm attributable to local excitation (LE) from the TOS moiety and a weak, broad peak around 590 nm.

Table 1. Photophysical properties of **TOS** and **TPA-TOS** in various solvents (c = 1.0 × 10^{-5} M) at 300 K.

	Solvents	l_{abs} [nm] (ε [10^4·M^{-1}·cm^{-1}])	l_{em} [nm][a] (Ψ_{em})
	Hexane	296 (6.1), 643 (1.2)	703 (0.66, 0.34[b])
	Benzene	292 (6.7), 652 (1.2)	393 (0.05)
	PhCN	302 (7.1), 653 (1.2)	354 (0.02)
TPA-TOS	MCH	301 (7.5), 652 (1.2)	355 (0.12), 703(0.07)
	MeCN	300(7.6), 662 (1.2)	355 (0.01)
	Zeonex[c]	304, 665	739 (0.74)
	PMMA[c]	300, 644	732 (0.32)
TOS	DCM	228 (5.8), 300 (1.1)	330 (0.02)

[a]λ_{ex} = 300 nm in N_2. [b]Tested under an O_2 atmosphere. [C]0.5 wt%.

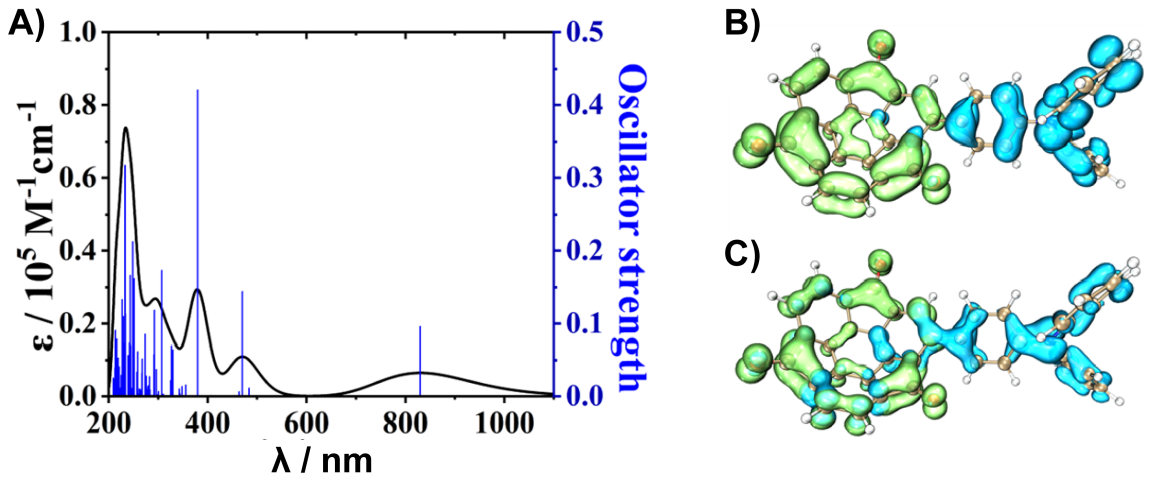

Figure 4. A) Simulated UV-vis spectrum of **TPA-TOS**. Isosurfaces of hole and electron distribution of **TPA-TOS** corresponding to B) 600-800 nm ($S_0 \rightarrow S_1$) and C) 300 nm ($S_0 \rightarrow S_{52}$) absorptions calculated at B3LYP/6-311G** level of theory. The blue and green isosurfaces indicate hole and electron distributions, respectively.

However, in nonpolar hexane, the intensity of the 350–400 nm emission diminishes significantly while a pronounced NIR emission emerges at 703 nm, accompanied by a

shoulder peak at ~780 nm upon excitation at 300 nm. The same NIR emission was observed under 650 nm excitation, confirming that this emission originates from the CT state, specifically TPA^{+}-TOS^{-}, formed following photoexcitation (Figure 5AB). The excitation spectrum demonstrated that TPA-TOS absorbs across nearly the entire visible range, enabling efficient NIR emission (Figure 5C). Relative to the weak emissive nature of TOS alone (Φ_{em}: 0.02 at 330 nm),[18] TPA-TOS exhibits a significantly enhanced fluorescence quantum yield of 0.66 at 703 nm in hexane under an N_2 atmosphere. Additionally, its NIR emission capability is robust in PMMA and Zeonex films, achieving Φ_{em} values of 0.32 and 0.74, respectively (Figure 5D).

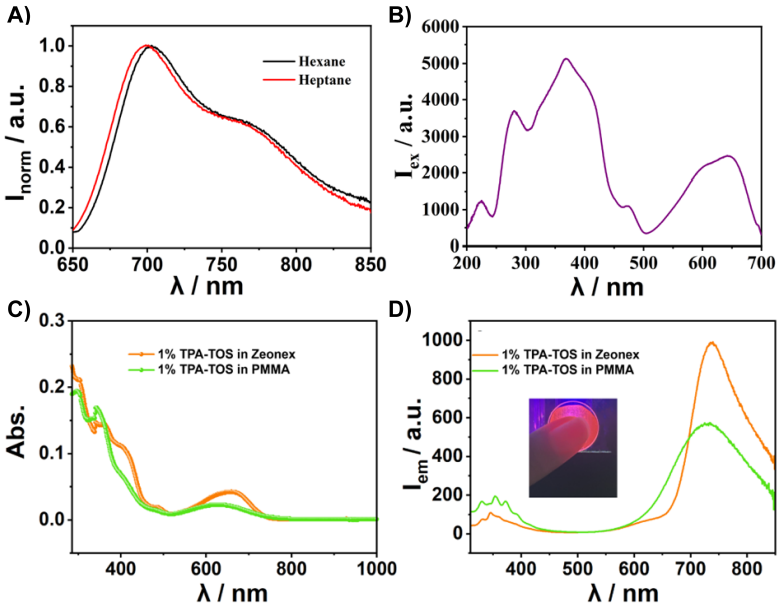

Figure 5. A) PL spectra (l_{ex} = 650 nm) of **TPA-TOS** in nonpolar solvents (c = 1.0 × 10^{-5} M) at 300 K. B) Excitation spectra (l_{em} = 750 nm) of **TPA-TOS** in hexane at 300 K (c = 1.0 × 10^{-5} M). C) UV−vis-NIR absorption spectra and D) PL spectra (l_{ex} = 300 nm) of **TPA-TOS** (0.5 wt%) in doped PMMA and Zeonex film at 300 K. The inset image was 0.5 wt% **TPA-TOS** Zeonex film taken under UV lamp (l_{ex} = 365 nm) irradiation.

To elucidate the origin of this strong NIR emission, various external factors influencing emission properties were investigated. Temperature-dependent PL measurements revealed a rise in emission intensity as the temperature increased from −40 °C to 30 °C, followed by a noticeable decline at temperatures exceeding 30 °C (Figure 3CD). This temperature-dependent behaviour is characteristic of systems where triplet states play a significant role in the emission process.[22-24] Atmospheric effects further verified the contribution of triplet states to the NIR emission of **TPA-TOS** (Figure 3E). Phosphorescence at 749 nm was observed both in 2-methyltetrahydrofuran glass at 77 K and in Zeonex film, which overlapped with the lower-energy portion of the emission spectrum (Figure 6). Collectively, these findings suggest that the observed NIR emission arises from both singlet (^{1}[**TPA$^+$-TOS$^-$**], ^{1}CT) and triplet (^{3}[**TPA$^+$-TOS$^-$**], ^{3}CT) components. Importantly, the energy gap between ^{1}CT and ^{3}CT (ΔE_{ST}) was calculated to be <0.01 eV (Figure 6), implying efficient thermally activated delayed fluorescence (TADF) coupled with room-temperature phosphorescence (RTP), which is mainly reported in the solid state systems [25-27] and the solution-based ones are still rare.[28, 29] This small ΔE_{ST} results from the effective spatial separation of the HOMO and LUMO within the **TPA-TOS** system, underscoring the unique photophysical properties of TADF incorporating RTP in nonpolar environments like hexane.

To investigate possible aggregation-induced effects, the author measured the photoluminescence (PL) spectra in solution at different concentrations ranging from 10^{-6} to 10^{-3} M. As shown in the experimental spectra (Figure 6D), the emission intensity decreases with increasing concentration, indicating that the molecule exhibits aggregation-induced quenching (AIQ) behaviour. However, the absence of any change in the emission peak

position suggests that the aggregated state of this molecule is non-emissive.

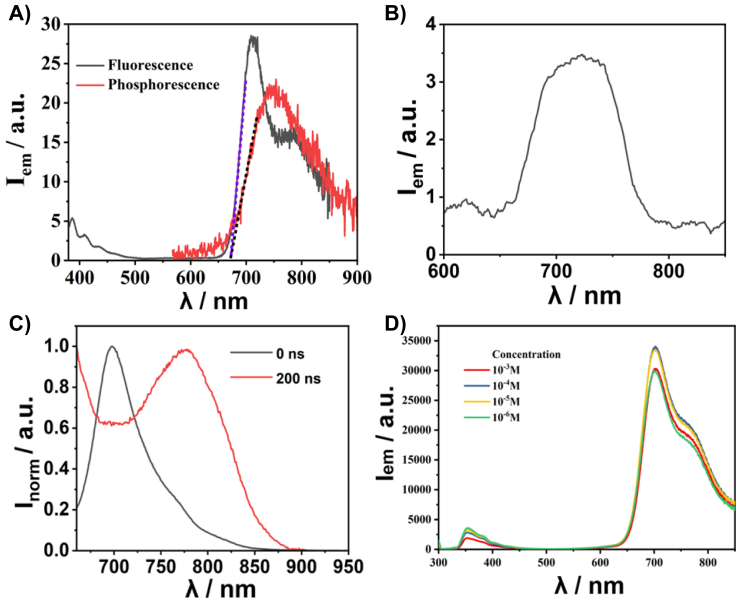

Figure 6. A) Emission spectrum of **TPA-TOS** (c = 110^{-3} M, l_{ex} = 300 nm) in 2Me-THF glass at 77 K. B) Phosphorescence spectrum of **TPA-TOS**-doped zeonex film (l_{ex} = 300 nm) at 300 K. C) Delayed emission spectra of **TPA-TOS** collected 200 ns after excitation at 650 nm in hexane (c = 1.0 x 10^{-5} M). D) Emission spectra of **TPA-TOS** with different concentration in hexane.

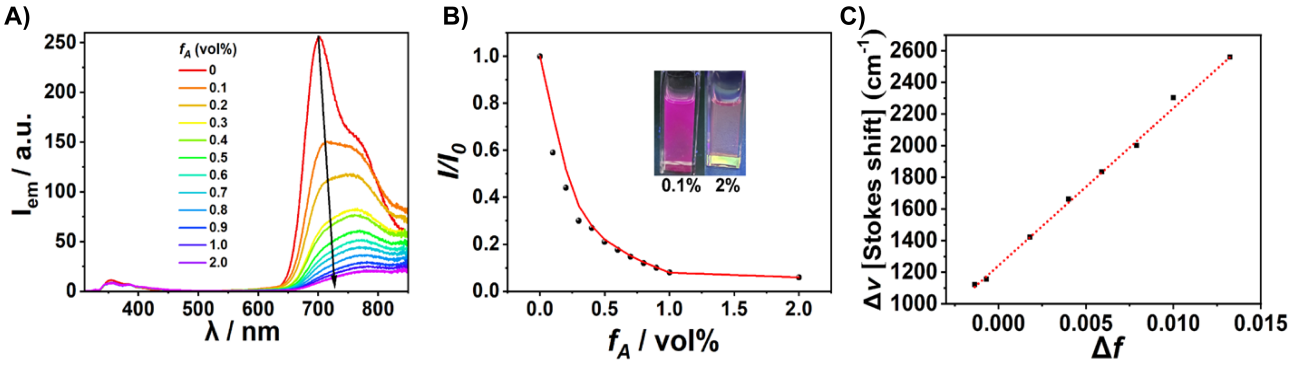

Figure 7. Emission spectra of TPA-TOS with the increase of volume fraction of MeCN in hexane (f_A). λ_{ex} = 300 nm, c = 1 × 10^{-5} M. A) Emission intensity change against f_A. B) I/I_0 values versus f_A of MeCN. Here, I_0 and I are the emission intensity in pure hexane and each hexane/MeCN mixture,

respectively. Inset image shows the emission change depending on the f_A value under 365 nm UV light. C) The Lippert–Mataga plot for TPA-TOS.

As above discussion revealed the solvent dependency in the emission property of **TPA-TOS**, the author measured the fluorescence spectra of **TPA-TOS** using a series of hexane–acetonitrile mixtures with varying polarity. It showed significant positive solvatofluorochromism as a function of the solvent permittivity (Figure 7). A linear correlation between Stokes shift and Lippert-Mataga solvent polarizability revealed that the dipole moment at the excited state (μ_e) reached 54 Debye (33 Debye by DFT calculation at B3LYP/6-311G**), which is significantly larger than the ground-state dipole moment μ_g (3.41 Debye). This finding supported the formation of CT structure at the excited state with a large dipole moment.

Moreover, the fluorescence intensity of **TPA-TOS** decreased with increasing solvent polarity, indicating that polar solvents accelerate non-radiative deactivation of the CT species involved in delayed fluorescence.

Section 4. Transient absorption and time-resolved spectroscopy

To investigate the solvent-dependent photo-relaxation dynamics of **TPA-TOS**, femtosecond transient absorption (fsTA) measurements were performed in nonpolar hexane and polar acetonitrile (MeCN) (Figure 8, Table 2**)**. Upon excitation at 343 nm, the fsTA maps during the initial 2 ps appeared similar in both solvents. Specifically, ultrafast spectral changes were observed, which are attributable to the localized excited (LE) state absorption originating from the **TPA** and **TOS** skeletons. This assignment aligns well with previously reported transient absorption (TA) spectra of **TOS**[18] and photoexcited **TPA**[30]. Meanwhile, a broad absorption component around 700 nm, corresponding to

charge transfer (CT) absorption associated with the formation of **TPA^{+}-TOS^{-}**, emerged in both solvents, indicating that fast CT processes occur even in nonpolar hexane.

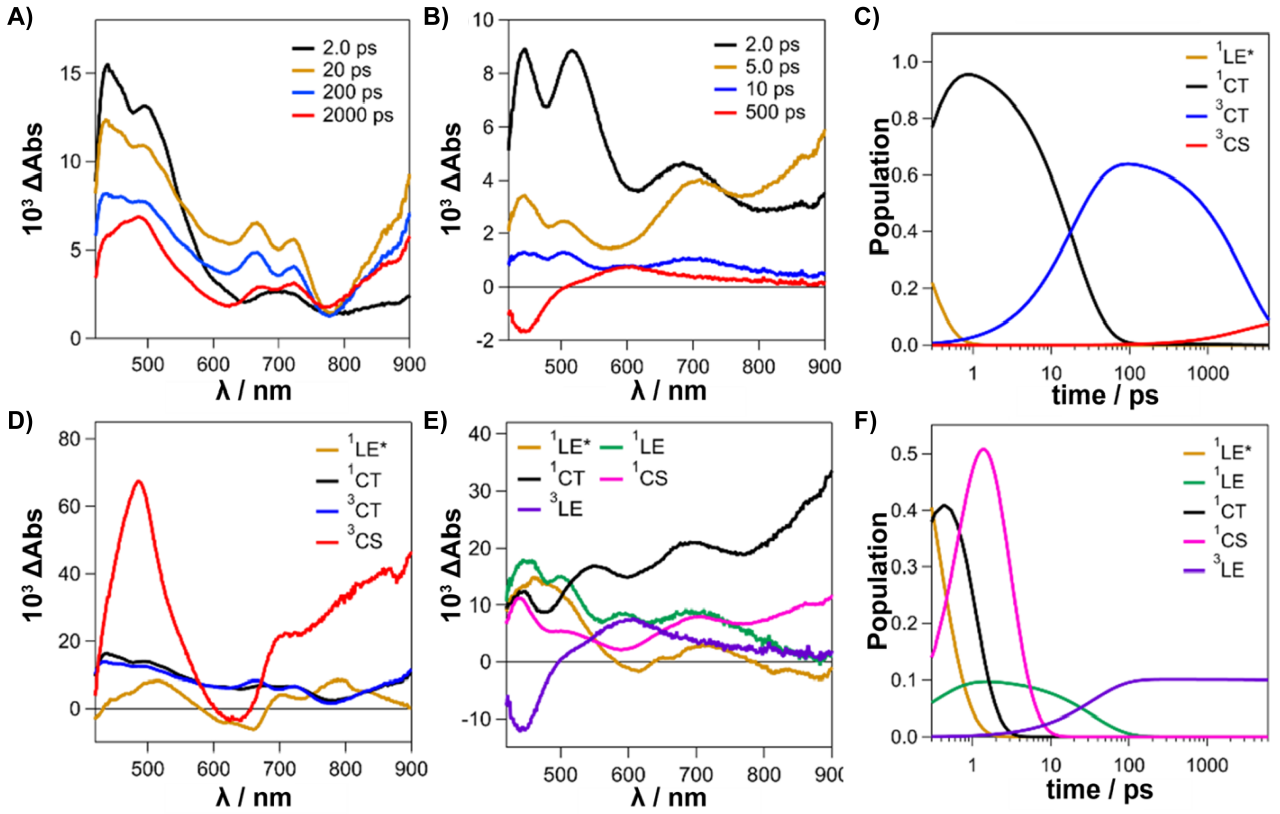

Figure 8. Dynamic optical properties of TPA-TOS. (A,B) fsTA spectra of **TPA-TOS**. (D,E) The species-associated spectra. (C,F) Time profiles of population change of each excited species. (ACD): obtained in hexane and (BEF): obtained in MeCN.

Table 2. Lifetime of each excited species

Solvent	^{1}LE*	^{1}LE	^{1}CT	^{3}CT	^{1}CS	^{3}CS	^{3}LE
Hexane	<410 fs	-	19 ps	2.9 ns	-	> 6 ns	-
MeCN	<410 fs	550 fs	1.9 ps	-	34 ps	-	> 6 ns

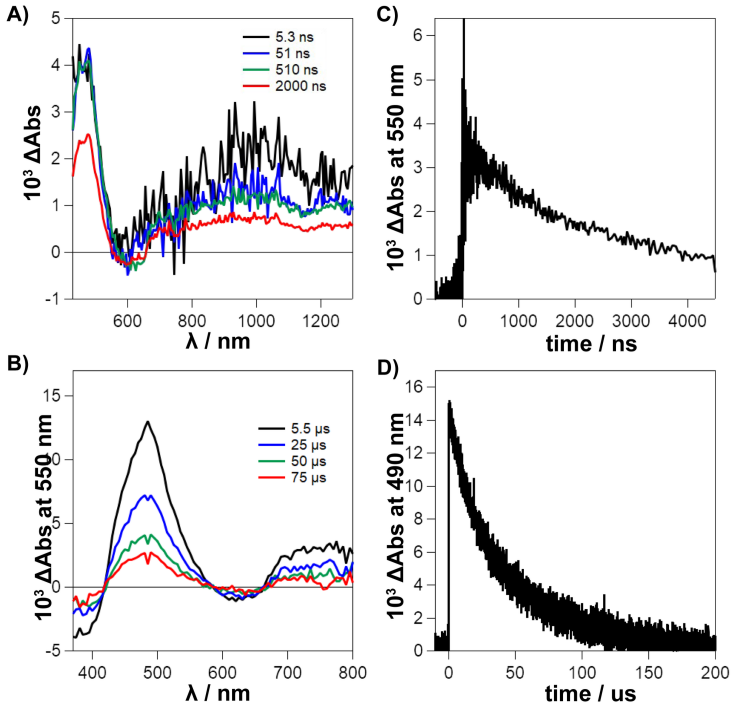

Figure 9. Picosecond (a) and nanosecond (b) transient absorption spectra and corresponding time profiles (c) and (d) of **TPA-TOS** in deaerated hexane after laser excitation at 355 nm (c =10^{-3} M).

At longer timescales—after 5 ps in MeCN and 20 ps in hexane—a new absorption band emerged in the near-infrared (NIR) region beyond 900 nm, which extended past 1000 nm as confirmed by picosecond transient absorption (psTA) measurements (Figure 9). This long-wavelength absorption exceeding 1000 nm closely resembles the characteristic absorption of the **TOS** radical anion (**TOS**$^{\bullet-}$, 1040 nm).[15] Simultaneously, the characteristic dual absorption band of the **TPA** radical cation (**TPA**$^{\bullet+}$) appeared at 650–750 nm, corroborating previous reports on **TPA**$^{\bullet+}$ absorption spectra.[31] Taken together, these findings strongly support the generation of a charge-separated (CS) state, specifically **TPA**$^{\bullet+}$**-TOS**$^{\bullet-}$, in both hexane and MeCN. These solvent-independent CS state dynamics and their distinct spectral fingerprints provide direct insight into the photophysical behaviors underlying **TPA-TOS**, establishing its ability to undergo efficient charge separation and radical formation across a wide range of solvent polarities. To further confirm the formation of the CS state, electron spin

resonance (ESR) measurements were conducted, which provided evidence for the generation of triplet radical species [^{3}(**TPA$^{\bullet+}$-TOS$^{\bullet-}$**)] (^{3}CS) (Figure 10A). Upon photoirradiation of a hexane solution of **TPA-TOS** at 123 K with 365 nm UV light, an ESR signal was detected at g = 2.0049, along with a distinct zero-field splitting pattern−a hallmark of triplet state formation. This observation unequivocally confirmed the presence of the ^{3}CS species. The zero-field splitting parameter (D) was determined from the fine structure of the ESR spectrum to be 116 G (11.6 mT), which was much smaller than the reported D value of the ^{3}CT species of carbazole-based small D-A system, reflecting the longer spin-spin distance than the case of ^{3}CT state.[32] From this parameter, the distance (r) between the two unpaired electrons was calculated to be 6.2 Å,[33] consistent with previously reported spin-spin distances in similar triplet radical ion pairs. This calculated distance aligns well with the structural characteristics of the **TPA$^+$-TOS$^-$** ^{3}CS species, further supporting its assignment as a triplet charge-separated state (Figure 10B). These ESR findings provide direct evidence for the involvement of the triplet CS state in the photophysical processes of **TPA-TOS**.

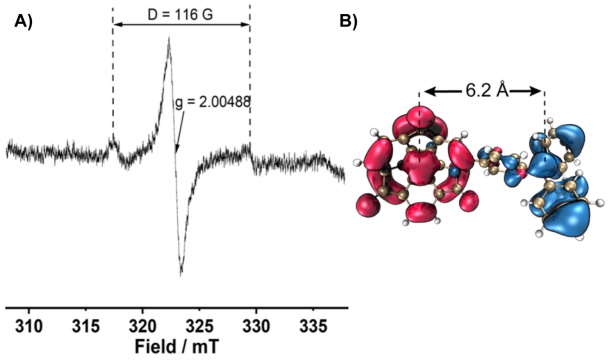

Figure 10. Radical ion pair of TPA-TOS. A) ESR spectrum of **TPA-TOS** (5 × 10^{-4} M) in deaerated hexane after 365 nm photoirradiation at 123 K. B) Scheme of radical ion pair distance. Spin density plot of was calculated as ^{3}(**TPA$^{\bullet+}$-TOS$^{\bullet-}$**) at UB3LYP/6-311+(d,p).

A more detailed analysis revealed a striking difference in the fate of the photo-relaxation process depending on the solvent polarity. In nonpolar hexane, the charge-separated (CS) states exhibited lifetimes ranging from several thousand picoseconds to hundreds of microseconds, indicating that the relaxation pathway involved intersystem crossing (ISC) and reverse intersystem crossing (RISC) processes between the ^{1}CT and ^{3}CT states. In contrast, in polar MeCN, all excited states of **TPA-TOS** rapidly relaxed within 10 ps, ultimately producing a weak broad absorption band around 600 nm after 500 ps, likely attributable to the previously reported triplet state of **TOS**.[18] This rapid decay process in MeCN, lacking ^{1}CT emission, suggests a competition between two relaxation pathways: one leading to the ^{3}LE state via the ^{1}LE state, and the other proceeding to the ^{1}CS state through fast electron transfer from the **TPA** to the **TOS** moiety of the ^{1}CT species. Based on these assumptions, the best-fitting results revealed the involvement of ^{1}LE, ^{3}LE, ^{1}CT, and ^{1}CS states in the MeCN solution, while additional states−^{3}CT and ^{3}CS−were found to contribute to the hexane solution. The proposed emission mechanisms, depending on the solvent system, are summarized in Figure 11. The results further clarified key rate dynamics. In hexane, the ISC rate from the ^{1}CT to ^{3}CT state (k_{3CT}: 3.53×10^{10} s^{-1}) was higher than the fluorescence rate from the ^{1}CT state (k_{LUM}^1: 1.81×10^{10} s^{-1}), explaining the negligible emission intensity from the ^{1}LE state. Another noteworthy observation is that the RISC rate from the ^{3}CT to ^{1}CT state (k_{1RCT}: 2.59×10^8 s^{-1}) was nearly identical to the phosphorescence rate (k_{LUM}^3: 2.09×10^8 s^{-1}), facilitating efficient thermally activated delayed fluorescence (TADF) alongside phosphorescence emission to give high Φ_{em} reaching more than 0.60. Such coexistence of TADF and room-temperature phosphorescence (RTP) is relatively rare, particularly in solution systems.[34] Considering the case in MCH and benzene, probably the population of TADF and RTP path is likely controlled by the solvent systems with relatively low polarity, which will be our future work. The relaxation pathway from the ^{3}CT state to the ^{3}CS state was slower by an

order of magnitude compared to the RISC process, resulting in only a small fraction of the excitons reaching the CS state as their final destination. These CS-state excitons transitioned slowly to the ground state via charge recombination (k_{CR}: $1.2 \times 10^2\ s^{-1}$). Conversely, two competitive fast relaxation pathways were observed: one leading to the ^{1}CT state (k_R^1: $2.82 \times 10^{12}\ s^{-1}$) and the other to the ^{1}LE state (k_R^2: $3.18 \times 10^{11}\ s^{-1}$). The faster charge transfer process quickly transitioned to the ^{1}CS state (k_{1CS}: $1.82 \times 10^{12}\ s^{-1}$), followed by charge recombination (k_{CR}: $5.2 \times 10^{11}\ s^{-1}$) due to a significant stabilization of CT and CS states in polar solvent. On the other hand, the slower relaxation path to the ^{1}LE state eventually reached the ^{3}LE state via ISC (k_{ISC+IC}: $2.9 \times 10^{10}\ s^{-1}$), exhibiting negligible fluorescence emission (k_{FL}: $1.6 \times 10^7\ s^{-1}$).

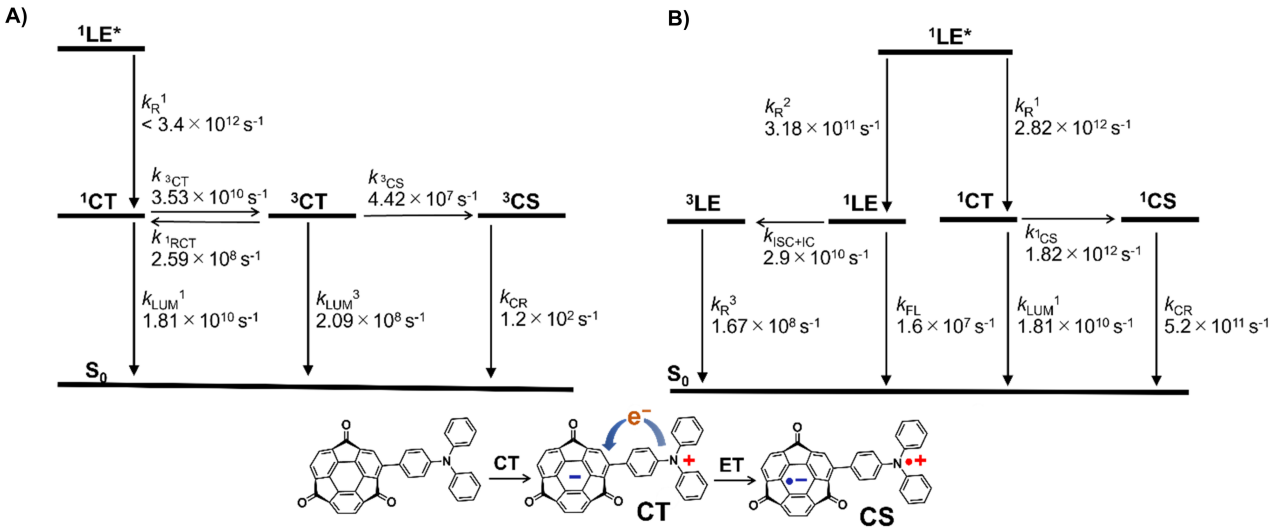

Figure 11. Energy-level diagram of **TPA-TOS**. (A) Schematic illustration of the excited-state energy relationships of **TPA-TOS** in hexane. (B) Schematic illustration of the excited-state energy relationships of **TPA-TOS** in MeCN.

Section 5. Plausible discussion about the effect of the curved-π structure

Considering that previously reported materials exhibiting long-CS lifetimes often feature a C_{60} skeleton, and that the curved-π systems typically display large spin-orbital coupling which accelerates ISC, it is reasonable to have interest in the contribution of the sumanene skeleton for the relevant phenomena. To tackle this mystery, the author conducted density functional theory (DFT) calculation. While several benchmarking studies have recommended some computational methods for the excited-state properties of intramolecular CT systems, it was found that the methodological dependence of **TPA-TOS** is rather complex due to its extended π-conjugation system. Indeed, as already applied in the evaluation of UV-vis absorption measurement results, TD-RB3LYP/6-311G(d,p) level of theory well reproduced the experimental CT band around 600-800 nm, although the excitation energy appears to be underestimated to some extent. The S_1-T_1 gap (ΔE_{ST}) is associated with the dihedral angle θ of **TOS** and **TPA**. This method also predicted the dihedral angle θ-dependent S_1-T_1 gap (ΔE_{ST}) and $\Delta E_{ST} \sim 0$ around $\theta = 90°$ (Figure 12). The S_1 potential energy curve was nearly flat in the range of $30^\circ \leq \theta \leq 120^\circ$, and the geometry optimization for the S_1 state converged to a structure with $\theta \sim 90^\circ$. This result supports experimental observation.

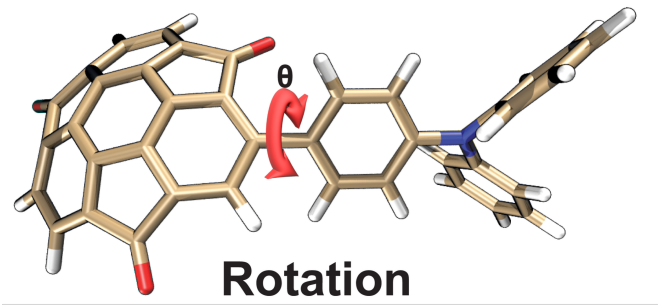

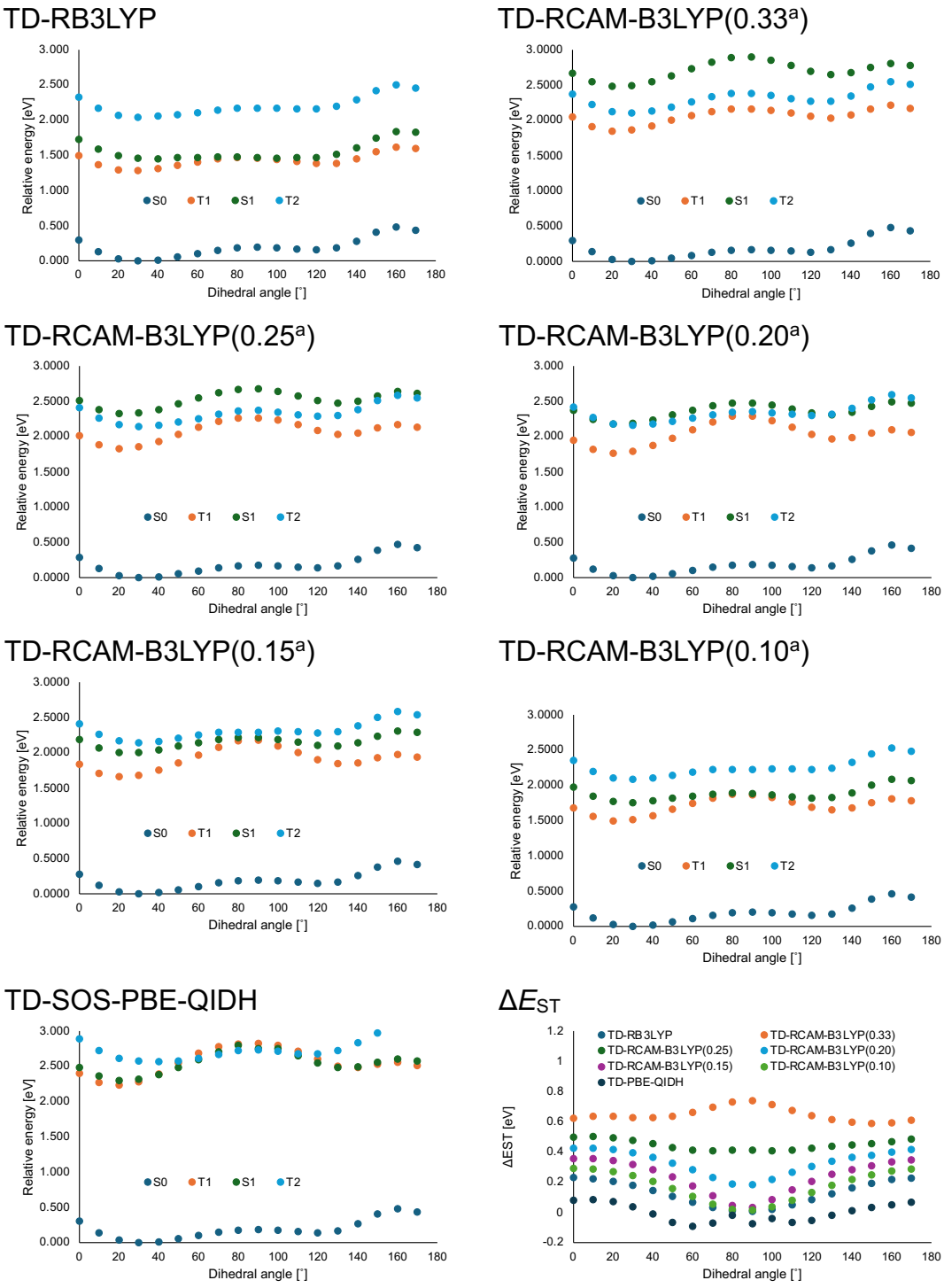

Figure 12. Dihedral angle (θ) dependence of the energies of the S_0, T_1, S_1 and T_2 states of **TPA-TOS** relative to the S_0 state energy at $\theta = 30^\circ$ (solvent: n-hexane) and the results of $\Delta E_{ST}(\theta) = E_{S1}(\theta) - E_{T1}(\theta)$. The θ-dependent geometries were constructed based on the S_0 geometry optimized at the RB3LYP/6-311G(d,p) level, keeping the remaining geometrical parameters frozen. The 6-311G(d,p)

basis set was used. There were some cases where T_3 was lower than S_1. [a] Denotes a range-separated hybrid functional in which the range-separation parameter ω, enabling an improved description of charge-transfer excitations.

However, further theoretical investigation revealed significant dependence on the function used, which prevents us from drawing more detailed conclusions how bowl shape of sumanene contributed the effective ISC and the high stability of CS state with μs-ordered lifetime at this stage. Nevertheless, the effect of curved-π structure of sumanene cannot be overlooked, as it at least contributed to; 1) high solubility of **TPA-TOS** even in non-polar hexane; 2) possessed a large |SOC| to accelerate ISC between ^{1}CT and ^{3}CT, supporting effective TADF and RTP to give high quantum yield, as well as long life time of the CS state. Although additional theoretical refinement is required to fully understand the impact of the sumanene skeleton and its bowl-shaped geometry, the experimental and theoretical findings suggest that this unique curved-π architecture plays a pivotal role in enhancing the photophysical performance of **TPA-TOS**. Indeed, such novel effect of the curved structure has also been confirmed in pristine **TOS**[18] and recently reported *N*-pyrrolic polycyclic aromatic hydrocarbons.[35] In the present case, the curved-π skeleton supports not only efficient ISC and TADF/RTP processes with high quantum yield, but also the observed long-lived CS state, which could have significant implications for applications in advanced photonic and optoelectronic devices. Based on this design strategy, the author further synthesized two additional **TOS** derivatives, **An** (Anthracen)**-TOS** and **Py** (Pyren)**-TOS**. These compounds exhibited photophysical behaviors identical to those of **TPA-TOS** (Figure 13), thereby providing further evidence for the validity and general applicability of this approach.

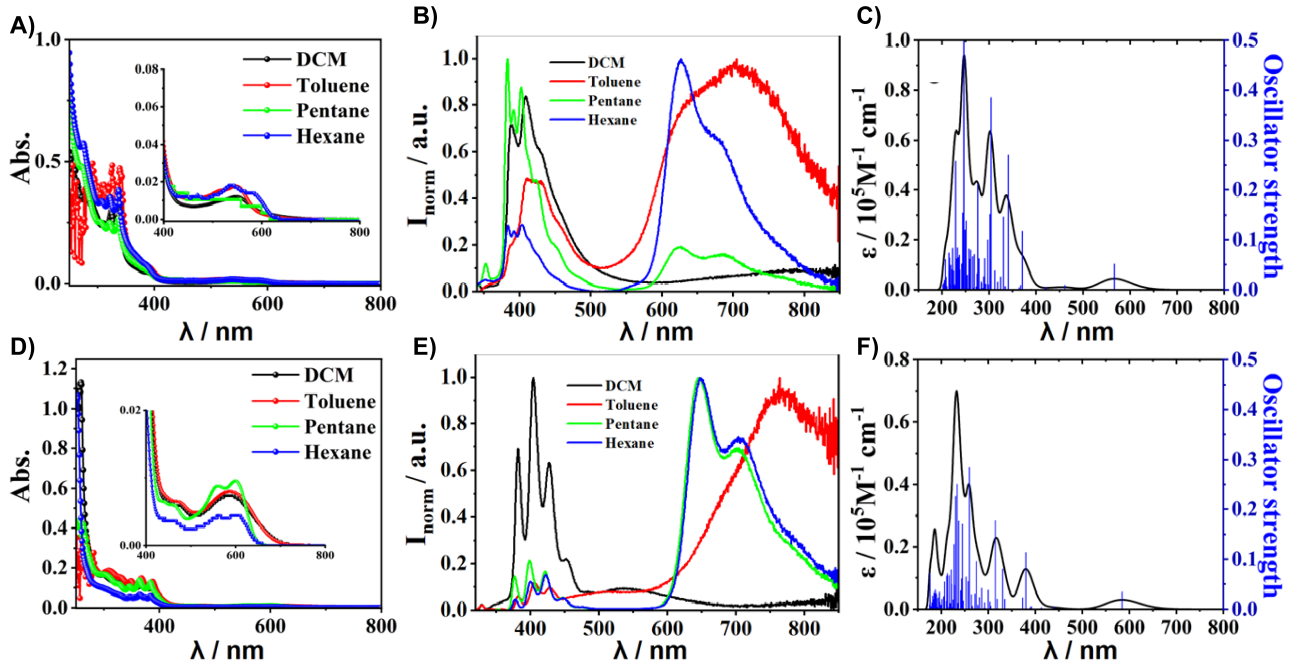

Figure 13. UV−vis-NIR absorption spectra of A) **An-TOS** and D) **Py-TOS** in various solvents (c = 1.0 x 10^{-5} M). Photoluminescence spectra (λ_{ex} = 300 nm) of B) **An-TOS** and E) **Py-TOS** in various solvents (c = 1.0 x 10^{-5} M). Simulated UV-vis spectrum of C) **An-TOS** and F) **Py-TOS**.

Section 6. Summary

In this chapter, the author has developed a novel donor-acceptor (D-A) near-infrared (NIR) dye, **TPA-TOS**, featuring a rigid bowl-shaped acceptor, **TOS**, and a strong donor, **TPA**, without relying on long-range conjugation or complex multi-donor/acceptor systems. This unique molecular design successfully establishes an effective TADF and RTP system, enabling high-efficiency NIR emission with an impressive quantum yield. Remarkably, the exciton in nonpolar hexane proceeds through efficient charge separation, reaching a long-lived CS state despite the short D-A distance. Conversely, in polar MeCN, the CS state becomes short-lived due to faster relaxation dynamics. Although further theoretical studies are required for a deeper understanding, the curved **TOS** framework clearly contributes to the observed

photophysics, providing a high solubility in non-polar hexane, large |SOC| to accelerate ISC between ^{1}CT and ^{3}CT states, giving rise to TADF and RTP. This unique design and the remarkable photophysical characteristics of **TPA-TOS** open new avenues for the development of efficient NIR dyes with innovative molecular architectures. By overcoming conventional limitations of D-A systems, this work provides a promising platform for future advancements in optoelectronic applications and deepens our understanding of charge separation dynamics in tailored curved-π systems.

Experimental section

Instrumentations and chemicals

All the chemical reagents and solvents were commercially purchased and purified according to the standard methods, if necessary. Air- and moisture-sensitive reactions were carried out using commercially available anhydrous solvents under inert atmosphere of nitrogen. Unless otherwise noted. ^{1}H and ^{13}C NMR spectra were recorded on a JEOL JNM-ECS400 NMR spectrometer (^{1}H: 400 MHz and ^{13}C: 100 MHz). Chemical shift (δ) are expressed relative to the resonances of the residual non-deuterated solvent for ^{1}H ($CDCl_3$: $^{1}H(\delta)$ = 7.26 ppm) and for ^{13}C ($CDCl_3$: $^{13}C(\delta)$ = 77.0 ppm). High resolution mass spectra (HRMS) were measured using electron impact mode (EI) methods on JEOL JMS-777V spectrometer. matrix-assisted laser desorption/ionization coupled to time-of-flight (MALDI-TOF) mass spectra were measured on Bruker Autoflex III spectrometer. The preparative TLC (PTLC) purification was conducted using Wako gel B-5F PTLC plates. Flash column chromatography was prepared using Kanto Silica gel 60N (neutral, spherical, 40-50 μm) and performed with a Yamazen preparative medium-pressure liquid chromatography system. UV-vis spectra were recorded on a JASCO V-670 spectrophotometer. Steady-state emission spectra were recorded on JASCO FP-6500DS and HORIBA Fluoromax-4 spectrometers. Phosphorescence, prompt fluorescence (PF), and delayed fluorescence (DF) spectra and decays were recorded using nanosecond gated luminescence and lifetime measurements (from 400 ps to 1 s) using either third harmonics of a high energy pulsed DPSS laser emitting at 355 nm (Q-Spark A50-TH-RE). Electron spin resonance spectrum was recorded on JEOL JES-X310 at 123 K after 365 nm light irradiation using 60 W LED.

Electrochemical characterization

Cyclic voltammetry (CV) was measured using Hokuto Denko HZ-7000 voltammetric analyzer at room temperature with a conventional three-electrode configuration consisting of a glass carbon working electrode, a platinum wire auxiliary electrode and an Ag wire pseudo-reference electrode with ferrocene–ferrocenium (Fc/Fc^+) as the internal standard. Nitrogen purged acetonitrile was used as solvent for scanning the oxidation with tetrabutylammonium perchlorate (TBAP) (0.1 M) as the supporting electrolyte. The cyclic voltammograms were obtained at a scan rate of 100 mV s^{-1}.

Transient absorption measurements

Femtosecond transient absorption measurements

The transient absorption spectroscopy measurements were carried out using a home-made femtosecond pump−probe system. Yb laser (PHAROS PH2-10W, Light Conversion) was used to create fundamental light pulses at 1030 nm at a repetition rate of 1 kHz. The pulse energy was 200 μJ, and the pulse duration was approximately 290 fs. 65% of the fundamental beam was directed to ORPHEUS optical parametric amplifier (Light Conversion) to produce excitation pulses at the desired wavelength or utilized to generate SHG (515 nm) and THG (343 nm) for sample pumping. The rest of the beam was delivered to a delay stage then attenuated appropriately and focused onto liquid D_2O or a sapphire crystal to generate a stable white light continuum for sample probing. The probe light was introduced to polychromators S3 equipped with a CMOS array (USP-PSMM-PK120, Unisoku) for the visible part of the spectrum and an InGaAs diode array (USP-NIR-PDA256, Unisoku) for the near-infrared (NIR) wavelengths. The measurements were carried out by comparing responses with and without excitation using a chopper synchronized with the fundamental laser pulses.

The spectra were typically acquired by recording 2000 shots, that is, averaging over 2 s. Excitation energies were sufficiently lowered to avoid multiple exciton generation; this was verified by recording a series of measurements with different excitation energies for the same sample. No excitation energy dependence of the response was observed.

Picosecond Transient Absorption Measurement[36]

Picosecond transient absorption measurement (picoTAS, Unisok, Osaka, Japan) was conducted by the device made by Unisoku Co., Ltd. Measurement method used in this measurement was Randomly Interleaved Pulse Train Method.

Nanosecond transient absorption measurements

Nanosecond transient absorption measurements were carried out using Unisoku TSP-2000 flash spectrometer. Surelite-I Nd-YAG (Q-switched) laser was employed for the flash photo-irradiation. A 150 W Xenon arc and halogen lamps were used as the monitor light source.

Quantum yield calculation

A relative value of quantum yield was obtained by following relationship with using the corrected spectra data JASCO Spectra Manager™.

$$\Phi_u = \Phi_{st} \cdot \left(\frac{F_u}{F_{st}}\right) \cdot \left(\frac{A_{st}}{A_u}\right) \cdot \left(\frac{D_u}{D_{st}}\right) \cdot \left(\frac{I_{ex,st}}{I_{ex,u}}\right) \cdot \left(\frac{{n_u}^2}{{n_{st}}^2}\right)$$

Here, F_{st} is the fluorescence quantum yield for the standard sample; F_u and F_{st} are the integrated values for the emission spectra of the unknown and standard samples; A_{st} and A_u are the absorbance

at the excitation wavelength of the standard and unknown samples; $I_{ex,st}$ and $I_{ex,u}$ are the intensities of the excitation light at the excitation wavelengths for the standard and unknown samples; and n_u and n_{st} are the average refractive indexes for the emission spectra measurement range for the standard and unknown samples.

In this measurement, Tris(2,2'-bipyridyl)Ru(II) hexahydrates as the reference (QY = 0.55).[37] Sample concentrations were low enough (less than 10% absorption across the spectrum) and the same sample solutions were used in both absorption and emission spectra measurements. Also, $I_{ex,st}/I_{ex,u}$ was corrected automatically in the software and considered to be 1.0. Therefore, the above equation becomes:

$$\Phi_u = \Phi_{st} \cdot \left(\frac{F_u}{F_{st}}\right) \cdot \left(\frac{A_{st}}{A_u}\right) \cdot \left(\frac{{n_u}^2}{{n_{st}}^2}\right)$$

Global and Target Analysis

Global (singular value decomposition-based) and target (differential equation-based) analysis is accomplished using the Glotaran software package (http://glotaran.org).[38]

Dipole moment of ground (μ_g) and excited state (μ_e)

The Stokes shift is determined as the difference in wavenumber between the lowest energy absorption and the highest energy florescence band. Estimates of these values obtained experimentally using the Lippert−Mataga equation.[39]

$$\Delta v = \left[2\left(\mu_{\mathrm{e}} - \mu_{\mathrm{g}}\right)^2 / hca^3\right] \Delta f + v^0$$

$$\Delta f = [(\varepsilon - 1)/(2\varepsilon + 1)] - [(n^2 - 1)/(2n^2 + 1)]$$

Where Δv is Stokes shift, the superscript "0" indicates the absence of solvent, μ_g and μ_e are dipole moments in the ground state and the excited state, respectively, *a* is Onsager cavity radius, here the value gets from gaussian calculation. ε and *n* are solvent dielectric constant and refractive index respectively.

Table 3. The Onsager cavity radius and, Ground-state and Singlet excited state dipole moments (in Debye, D).

	Onsager cavity radius (Å)	$\boldsymbol{\mu_g}$[a]	$\boldsymbol{\mu_e}$[b]	$\boldsymbol{\mu_e}$[c]
TPA-TOS	6.57	3.41	33.32	54.27

[a]Ground-state dipole moment estimated by Gaussian software.

[b]Excited-state dipole moment estimated by Gaussian software.

[c]Excited-state dipole moment calculated from equation.

Calculate spin-spin distance

Spin-spin distance *r* in 3CS state of TPA-TOS was estimated from the EPR *D* value (triplet ZFS) with using the point-dipole approximation.[33]

$$|D| = \frac{\mu_0}{4\pi}\frac{g^2\mu_B^2}{h}\frac{1}{r^3} \Rightarrow r \propto |D|^{-1/3}$$

If *D* is in mT:

$$r(\text{Å}) \approx \left(\frac{52040}{28.025|D(\text{mT})|}\right)^{1/3}$$

Theoretical calculations

The preliminary calculation data of molecular geometry of S_0 state were optimized by density functional theory (DFT), and the geometries of S_1, T_1 states were optimized by time-dependent DFT (TDDFT) at the B3LYP/6-311G** level with the Gaussian-16 program.[40] Isosurfaces of hole and electron distribution, were generated by Multiwfn.[41, 42] The approximate optimization results reveal that the molecular will twist in the excited states. Thus, the efficient intersystem crossing (ISC) or reverse ISC process should be ascribed to a twist structure in the excited state.

To test if the assumption of fast equilibration between the singlet and triplet manifold holds, the rate of ISC and rISC must be estimated. The author only consider the direct T_1 to S_1 transition, because calculation of T2 and S2 have a large energy gap with T_1 and S_1, so neglecting the intersystem crossing. And for this purpose, employ the Fermi Golden Rule approximation in combination with a Marcus formalism to estimate the density of states from the reorganization energy λ and the driving force ΔE according to the equation.[43]

$$k = \frac{2\pi}{\hbar}\left|\langle\psi_f|\widehat{\mathcal{H}}_{SO}|\psi_i\rangle\right|^2\sqrt{\frac{1}{4\pi\lambda k_b T}}\exp\left(-\frac{(\Delta E_{ST}+\lambda)^2}{4\lambda k_b T}\right)$$

Here, ħ is the Planck constant, k_b is the Boltzmann constant and T is the temperature. $\langle\psi_f|\widehat{\mathcal{H}}_{SO}|\psi_i\rangle$ spin-orbit coupling between the initial and final adiabatic electronic states. When calculate k_{ISC}, λ corresponds to the difference between the vertical energy of the final state (here T1) at the geometry and in the solvent field (non-equilibrium regime) of the initial state (here S1) and its adiabatic energy. When calculate k_{ISC}, λ corresponds to the difference between the vertical energy of the final state (here S1) at the geometry and in the solvent field (non-equilibrium regime) of the initial state (here T1) and its adiabatic energy, while the driving force ΔE_{ST} is identified as the adiabatic

singlet–triplet gap. SOC is calculated by using the ORCA with the effective charge approximation of the Breit-Pauli self-selected orbital Hamiltonian.[44]

Calculation of excited state lifetime according to Einstein's formula.

$$\tau = \frac{3}{2fv^2}$$

Table 4. Calculated results of **TPA-TOS**.

	$SOC(S_1\text{-}T_1)$ (cm^{-1})	ISC(s^{-1})	rISC(s^{-1})	lifetimeτ(s)	k_s(s^{-1})	lifetimeτ(t)	k_t(s^{-1})
S_1	0.01	1.25E+03	4.75E+02	1.03E-08	9.68E+07	-[a]	-
T_1	0.32	1.03E+06	3.73E+05	6.52E-07	1.53E+07	1.61E-01	6.20

[a] The oscillator strength is 0.

Difficulties in Theoretical Investigation of TPA-TOS

However, indeed, theoretical results of excitation properties for delocalized intramolecular CT systems depend on the level of approximation. Of course, there have been several benchmarking studies suggesting recommended calculation methods for excitation properties of intramolecular CT systems. Because of the extended π-conjugation system, the methodology dependence on the **TPA-TOS** was somewhat complicated.

Geometry optimization

First, the author performed geometry optimization of **TPA-TOS** (in hexane) in the S_0 state at the RB3LYP/6-311G(d,p) level with the SMD model for the environmental effects. Then, the author simulated the electronic absorption spectrum at the TD-RB3LYP/6-311G(d,p) level, which reproduced well the position experimental CT band around 600-800 nm, although the excitation energy seems to underestimate to some extent. Usually, long-range corrected DFT functionals are recommended for the description of such CT bands. However, TD-RCAM-B3LYP/6-311G(d,p)

overestimated significantly the excitation energies with the default range-separating parameter (μ = 0.33 bohr^{-1}). The author also performed the calculations with a recently proposed global double hybrid functional, SOS-PBE-QIDH,[45] recommended for prediction of CT excitations in a benchmarking study by Mester et al.[46] Among the employed methods, the TD-B3LYP, TD-RCAM-B3LYP(0.15) or TD-RCAM-B3LYP(0.10) seem to better reproduce the experimental absorption wavelength.

The dihedral angle (θ) dependence of relative energies

The author also checked the dihedral angle (θ) dependence of relative energies of the S_0, T_1 and S_1 states. The TD-RB3LYP predicted the θ-dependent S_1-T_1 gap (ΔE_{ST}) and $\Delta E_{ST} \sim 0$ around $\theta = 90^\circ$. However, it is found that the results of $E_{T1}(\theta)$, $E_{S1}(\theta)$, and $\Delta E_{ST}(\theta)$ depend strongly on the choice of functional. For the TD-RCAM-B3LYP results with $\mu \geq 0.2$ bohr^{-1}, ΔE_{ST} was non-zero around $\theta = 90^\circ$. Particularly, when the author employed the TD-RCAM-B3LYP(0.33), $\Delta E_{ST}(\theta = 90^\circ) > \Delta E_{ST}(\theta = 30^\circ)$. Furthermore, the T_2 state was below the S_1 state around $\theta = 90^\circ$. The double hybrid TD-SOS-PBE-QIDH predicted negative ΔE_{ST} probably because the perturbative corrections for the S_1 and T_1 states were performed separately. Another issue is the S_1 potential energy curve. With the TD-RB3LYP method, the S_1 potential energy curve was very flat in the range $30^\circ \leq \theta \leq 120^\circ$, and the geometry optimization for the S_1 state resulted in a geometry with $\theta \sim 90^\circ$. With the TD-RCAM-B3LYP(0.15) method, whose S_1 absorption wavelength (E_{S1} = 1.9992 eV, $\lambda_{abs,calc}$ = 620 nm, f = 0.1642, solvent: n-hexane) seems to reproduce well the experimental result, the S_1 potential energy curve was not so flat around the region and the geometry optimization for the S_1 state (the frequency analysis was not performed yet) resulted in a geometry with $\theta \sim 27^\circ$ (E_{S1} = 1.7389 eV, $\lambda_{em,calc}$ = 713 nm, f = 0.1623, solvent: *n*-hexane).

When the DFT-based results show such strong xc-functional dependences, the author usually try

to perform the wavefunction theory (WFT)-based methods, i.e., *ab initio* post-Hartree-Fock (HF) methods. However, the author faced difficulty in conducting the post-Hartree-Fock methods because of the weak but non-negligible electron correlation effects in the S_0 state that could not be recovered appropriately from the perturbative correction to the spin-restricted (R)HF solution.

When the author performed the spin-unrestricted (U)HF calculation followed by the instability analysis for the UHF solution, the author obtained the broken-symmetry (BS-)UHF solution with lower energy than the RHF solution. Although the diradical character y_0 at the spin-projected (P)UHF level was less than 0.1, meaning that the S_0 state is fairly "closed-shell", the solution showed high spin-contaminations with $<S^2> \sim 4$, because plural diradical characters y_0, y_1, y_2, … exhibited non-zero values. When y_0 of a system at the PUHF level is larger than ~0.5, the system can often be regarded as an "open-shell" system where partially unpaired electrons appear mainly due to the strong (static) electron correlation. In the present case, however, the RHF solution cannot be a good starting point for the post-HF calculations. The author should note that usual hybrid DFT methods did not give the BS solutions (unless the fraction of Hartree-Fock exchange is ~ 100%).

When the post-RHF calculations did not work appropriately, the post-UHF or the multireference calculations may be candidates the author should employ. Unfortunately, the former ones are considered not to give reliable results for the excited states because of the highly spin-contaminated reference state with $<S^2> \sim 4$. The author need to set an appropriate active space for the latter ones, but there are plural non-zero but small diradical characters y_0, y_1, y_2, …, which indicates the difficulty in selecting active space. Indeed, when the author performed the *x*-state averaged (SA*x*-)CASSCF(n,m) + QD-NEVPT2 calculations with different numbers of active electrons (n) and orbitals (m), but the results of S_1 excitation energy overestimated the experimental result.

Table 5. Post-HF vertical excitation energies of **TPA-TOS** for the S_1 state based on the S_0 geometry optimized at the RB3LYP/6-311G(d,p) level.

Method	$E(S_1)$ [eV] (λ [nm])
RHF+RI-CC2/def2-SVP[#]	2.668 (465)
UHF+RI-CC2/def2-SVP[#†]	2.658 (466)
RHF+RI-CC2/def2-TZVP[#]	2.447 (507)
RHF+RI-CIS(D)/6-311G(d,p)[##]	2.651 (468)
SA5-CASSCF(4,4)+QD-NEVPT2/6-311G(d,p)[##]	2.202 (563)
SA5-CASSCF(6,6)+QD-NEVPT2/6-311G(d,p)[##]	2.474 (501)
SA5-CASSCF(8,8)+QD-NEVPT2/6-311G(d,p)[##]	2.384 (520)

[#] Calculations were performed using Turbomole 7.7 (gas phase calculation).

[##] Calculations were performed using ORCA 5.0.4. C-PCM was employed (solvent: n-hexane). SA*x*-CASSCF(*n*,*m*) represent that the state-averaged (SA-)CASSCF calculations were performed for the *x* singlet states with the *n*-electron and *m*-orbital complete active space.

[†]The BS-UHF solution (E_{tot} = -1765.6466007 a.u., $<S^2>$ = 4.09) was lower than the RHF solution (-1765.5899125 a.u., $<S^2>$ = 0.00).

Synthetic procedure and characterization data

2-(4-(diphenylamino)phenyl)-1H-tricyclopenta[def,jkl,pqr]triphenylene-1,4,7-trione (TPA-TOS)

To a 4 mL test tube equipped with a magnetic stir bar were added **TOS-Br** (38.6 mg, 0.10 mmol), 4-(Diphenylamino)phenylboronic acid (34.7 mg, 0.12 mmol), $PdCl_2$(amphos)2 (1.4 mg, 2.0 μmol), Zn complex (52.1 mg, 0.15 mmol), and THF (1.0 mL). The mixture was stirred for one hour at 80 °C and then cooled to room temperature. The mixture was extracted with DCM (ca. 3 mL × 3). The combined organic extract was dried over Na_2SO_4. After filtration, the filtrate was concentrated under reduced pressure. The residue was purified by PTLC (CH_2Cl_2) to give the green solid.

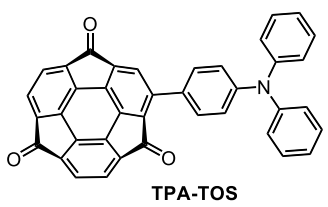

TPA-TOS: mp: 400 °C (dec.). TLC: R_f = 0.55 (CH_2Cl_2); ^{1}H NMR (600 MHz, Chloroform-*d*, ppm): δ = 7.63 (s, 1H), 7.52 (d, *J* = 11.2 Hz, 2H), 7.43 (d, *J* = 7.3 Hz, 1H), 7.40 (d, *J* = 8.0 Hz, 1H), 7.38 (d, *J* = 9.6 Hz, 1H), 7.37 (d, *J* = 7.7 Hz, 1H), 7.31 (t, *J* = 7.7 Hz, 4H), 7.19 (d, *J* = 7.7 Hz, 4H), 7.11 (t, *J* = 7.3 Hz, 2H), 7.09 (d, *J* = 8.4 Hz, 2H); ^{13}C NMR (150 MHz, Chloroform-*d*, ppm): δ = 188.74, 188.48, 186.97, 150.67, 150.48, 149.83, 149.10, 148.88, 147.06, 146.30, 144.50, 144.08, 143.96, 143.57, 143.33, 136.94, 131.04, 129.67, 129.19, 128.38, 128.31, 126.71, 126.62, 126.49, 126.34, 125.92, 125.79, 124.25, 120.95; IR (ATR, cm^{-1}): $\tilde{\nu}$ = 2938, 2923, 2851, 1716, 1589, 1561, 1512, 1488, 1329, 1286, 1193, 1181, 951, 756, 746, 697; HRMS (EI): *m/z* Calcd. for $C_{39}H_{19}NO_3^+$: 549.1365 $[M]^+$; found: 549.1360.

2-(pyren-2-yl)-1H-tricyclopenta[def,jkl,pqr]triphenylene-1,4,7-trione (Py-TOS)

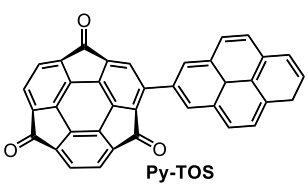

Py-TOS: mp: 321 °C (dec.). TLC: R_f = 0.65 (CH_2Cl_2); ^{1}H NMR (400 MHz, Chloroform-*d*) δ 8.44 (s, 2H), 8.22 (d, *J* = 7.7 Hz, 2H), 8.14 (d, *J* = 0.6 Hz, 4H), 8.07 – 8.02 (t, *J* = 0.6 Hz, 1H), 7.95 (s, 1H), 7.47 (dd, *J* = 22.40, 7.30

Hz, 2H), 7.38 (dd, *J* = 23.32, 7.30 Hz, 2H). ^{13}C NMR (151 MHz, Chloroform-*d*) δ 188.54, 188.45, 186.84, 150.51, 150.22, 149.97, 149.32, 149.27, 147.50, 144.98, 144.38, 144.02, 143.97, 143.79, 143.47, 138.65, 133.10, 131.60, 131.31, 128.35, 128.01, 127.68, 126.84, 126.70, 126.68, 126.54, 126.43, 126.26, 125.53, 125.42, 124.58. IR (ATR): *v* 2957, 2923, 2853, 1716, 1561, 1461, 1396, 1261, 1177, 1071, 951, 839, 814, 744, 719 cm^{-1}; HRMS (EI) m/z Calcd. for [$C_{37}H_{14}O_3^+$] (M^+): 506.0943, found 506.0945.

(r)-2-(anthracen-9-yl)-1H-tricyclopenta[def,jkl,pqr]triphenylene-1,4,7-trione (An-TOS)

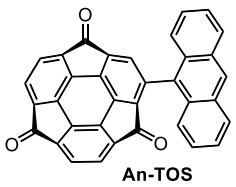

An-TOS: mp: 212 °C (dec.). TLC: R_f = 0.6 (CH_2Cl_2). ^{1}H NMR (400 MHz, Acetonitrile-*d*$_3$) δ 8.66 (s, 1H), 8.17 (d, *J* = 8.2 Hz, 1H), 8.08 (d, *J* = 8.5 Hz, 1H), 8.04 (d, *J* = 8.5 Hz, 1H), 7.62 – 7.54 (m, 2H), 7.50 (s, 2H), 7.41 (d, *J* = 7.4 Hz, 1H), 7.38 (d, *J* = 8.2 Hz, 1H), 7.32 (s, 1H), 7.22 (d, *J* = 7.4 Hz, 1H), 7.12 – 7.05 (m, 2H). ^{13}C NMR (100 MHz, Acetonitrile-*d*$_3$) δ 189.87, 189.64, 188.62, 151.54, 151.47, 151.31, 151.22, 150.88, 150.07, 145.16, 144.83, 144.76, 144.64, 144.56, 143.25, 140.08, 132.54, 132.29, 132.08, 132.06, 130.54, 129.80, 129.60, 129.49, 128.84, 127.40, 127.24, 127.10, 127.01, 126.78, 126.76, 126.59, 126.56, 126.53, 126.29. IR (ATR): *v* 2957, 2923, 2852, 1717, 1635, 1566, 1443, 1394, 1326, 1262, 1200, 1179, 1070, 1011, 949, 844, 729, 701 cm^{-1}. HRMS (EI) m/z Calcd. for [$C_{35}H_{14}O_3^+$] (M^+): 482.0943, found 482.0940.

^{1}H NMR spectrum of **TPA-TOS** (600 MHz, Chloroform-*d*, 300 K).

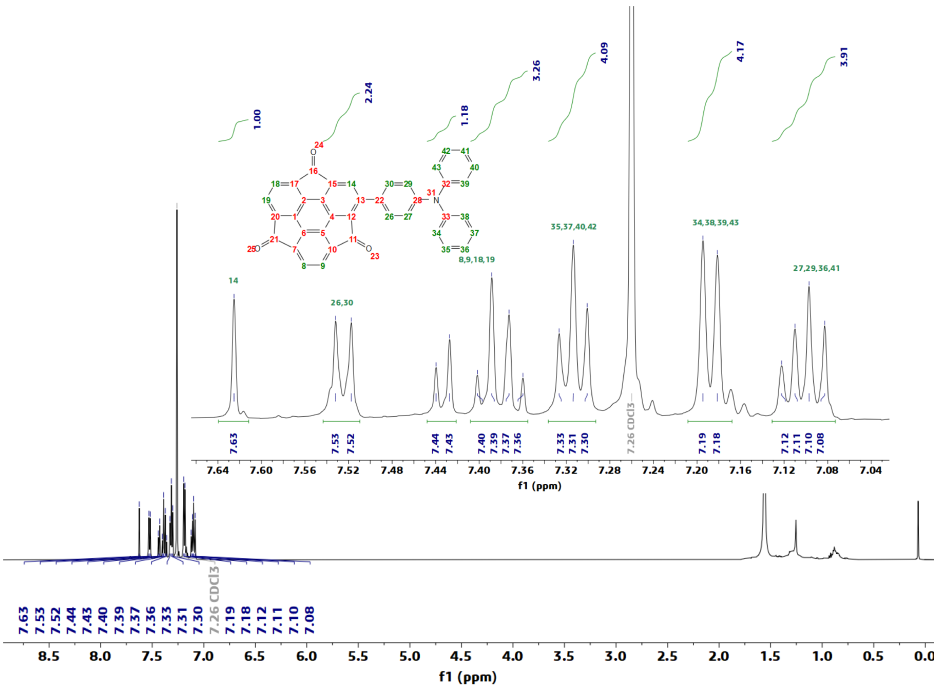

2D NMR Correlation (COSY) spectra of **TPA-TOS** aromatic region in chloroform-*d* at 300 K.

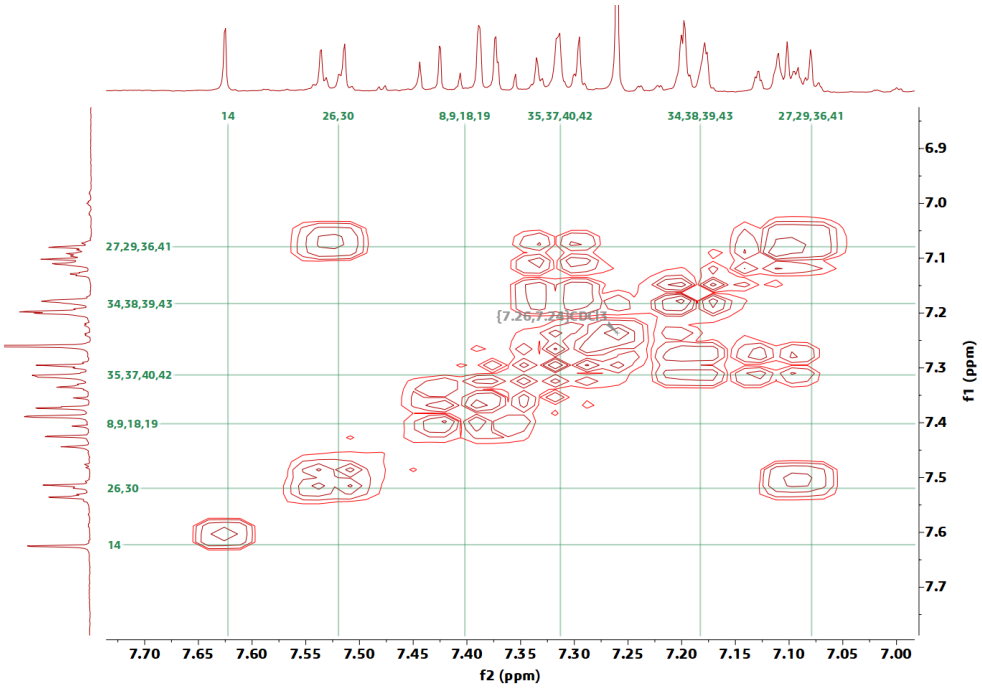

^{13}C NMR spectrum of **TPA-TOS** (150 MHz, Chloroform-*d*, 300 K).

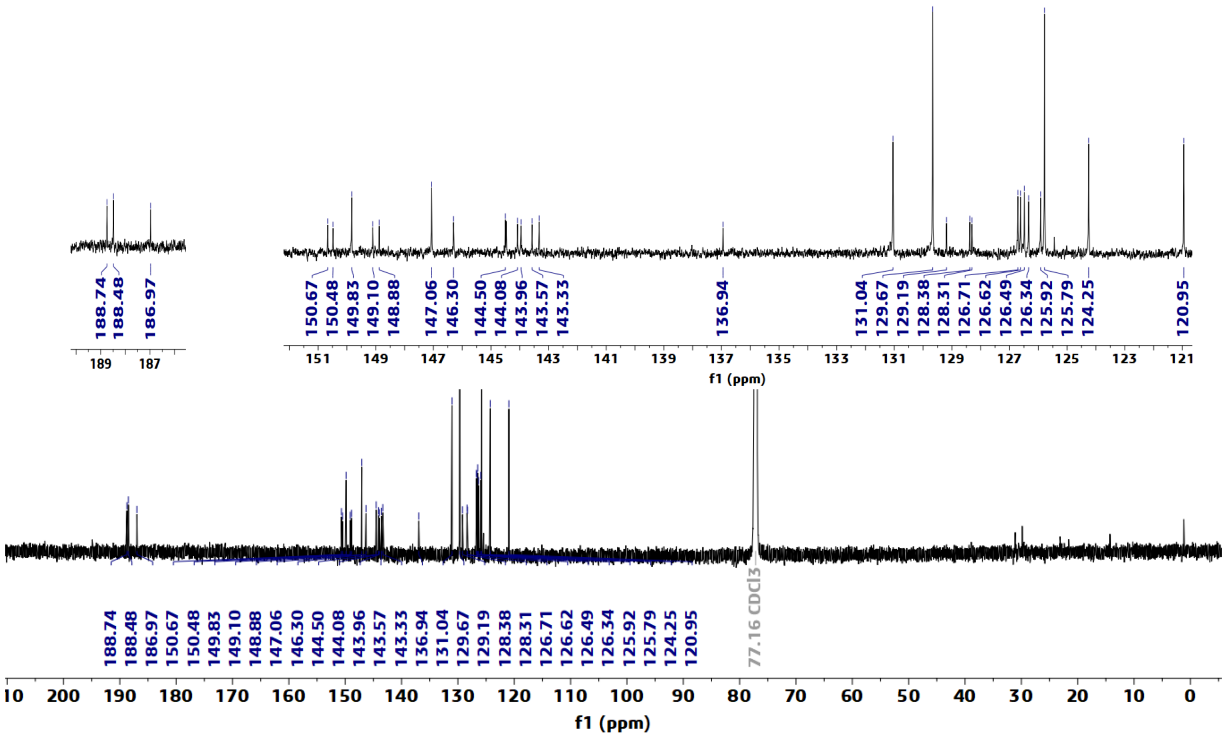

^{1}H NMR spectrum of **Py-TOS** (400 MHz, Chloroform-*d*, 300 K).

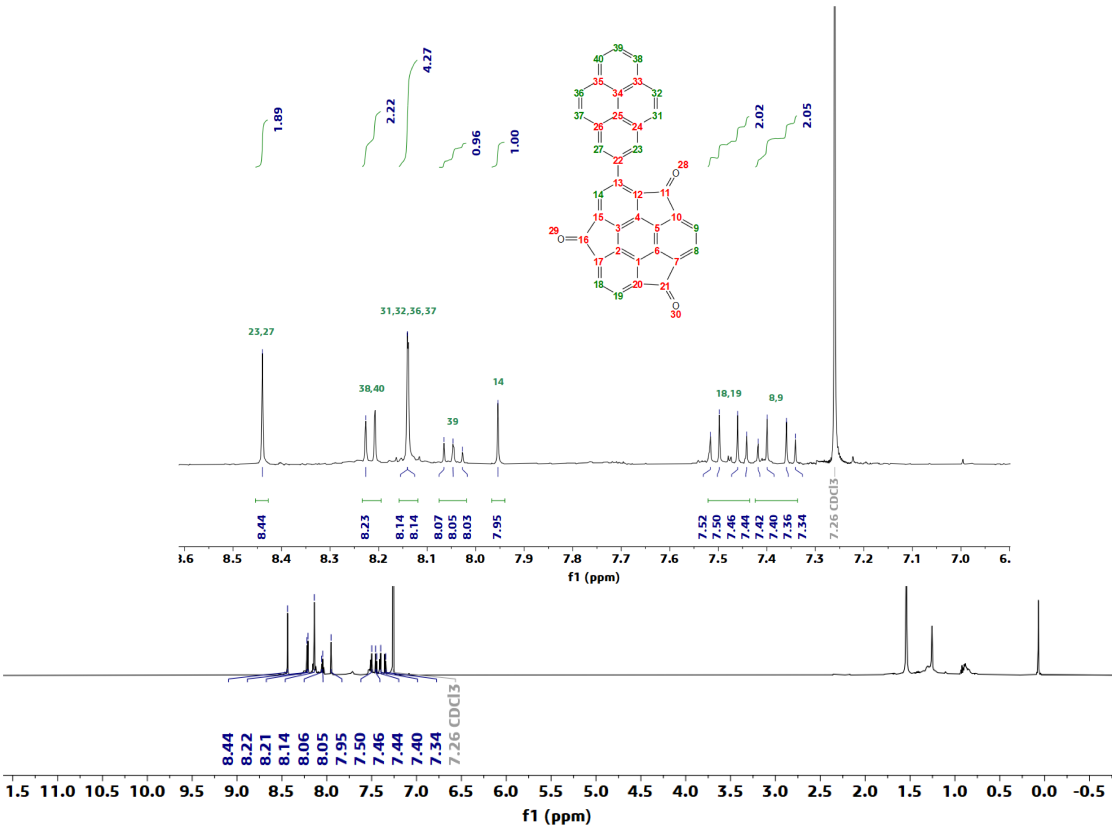

2D NMR Correlation (COSY) spectra of **Py-TOS** aromatic region in chloroform-*d* at 300 K.

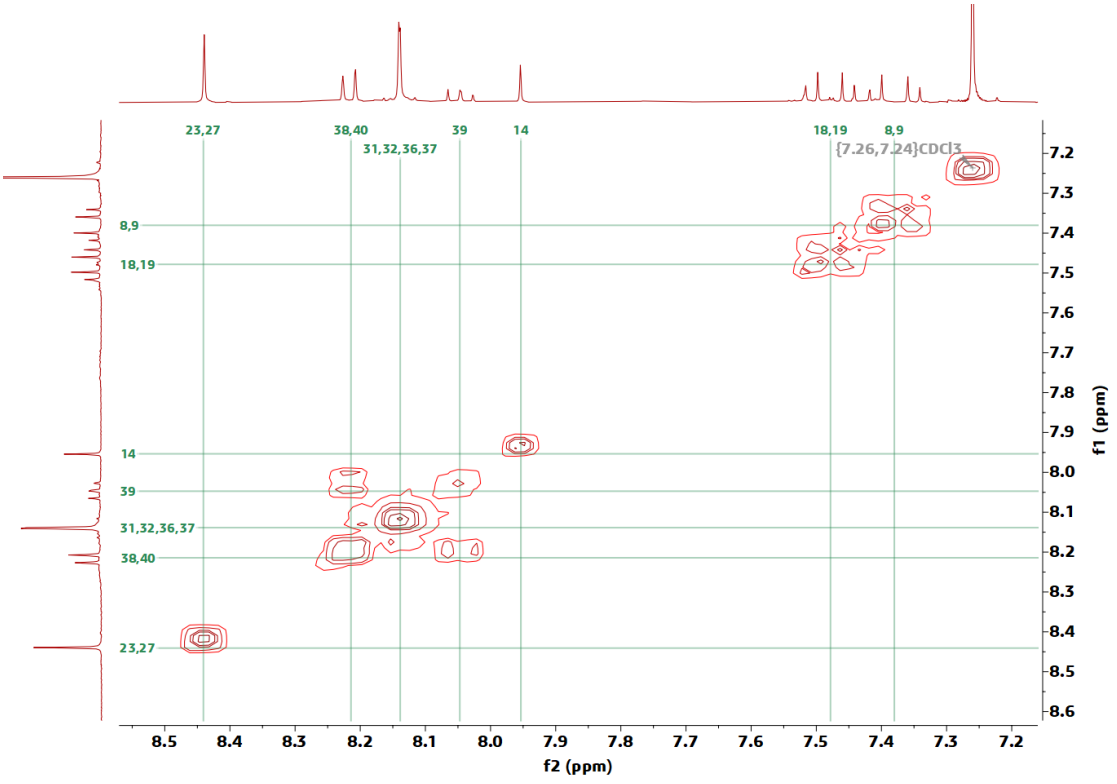

^{13}C NMR spectrum of **Py-TOS** (100 MHz, Chloroform-*d*, 300 K).

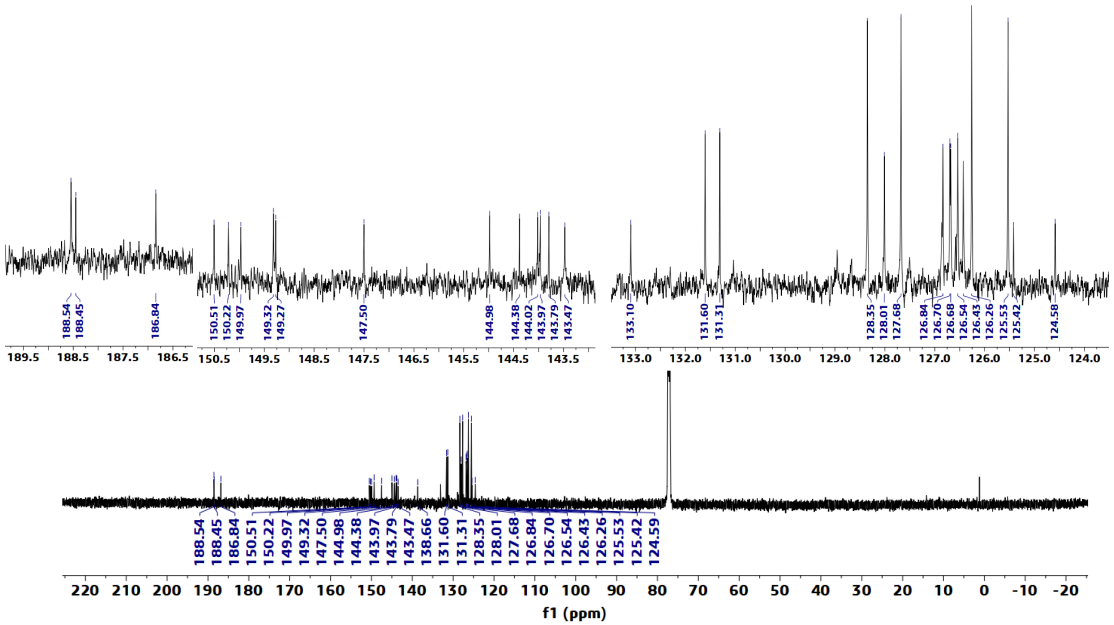

^{1}H NMR spectrum of **An-TOS** (400 MHz, Chloroform-*d*, 300 K).

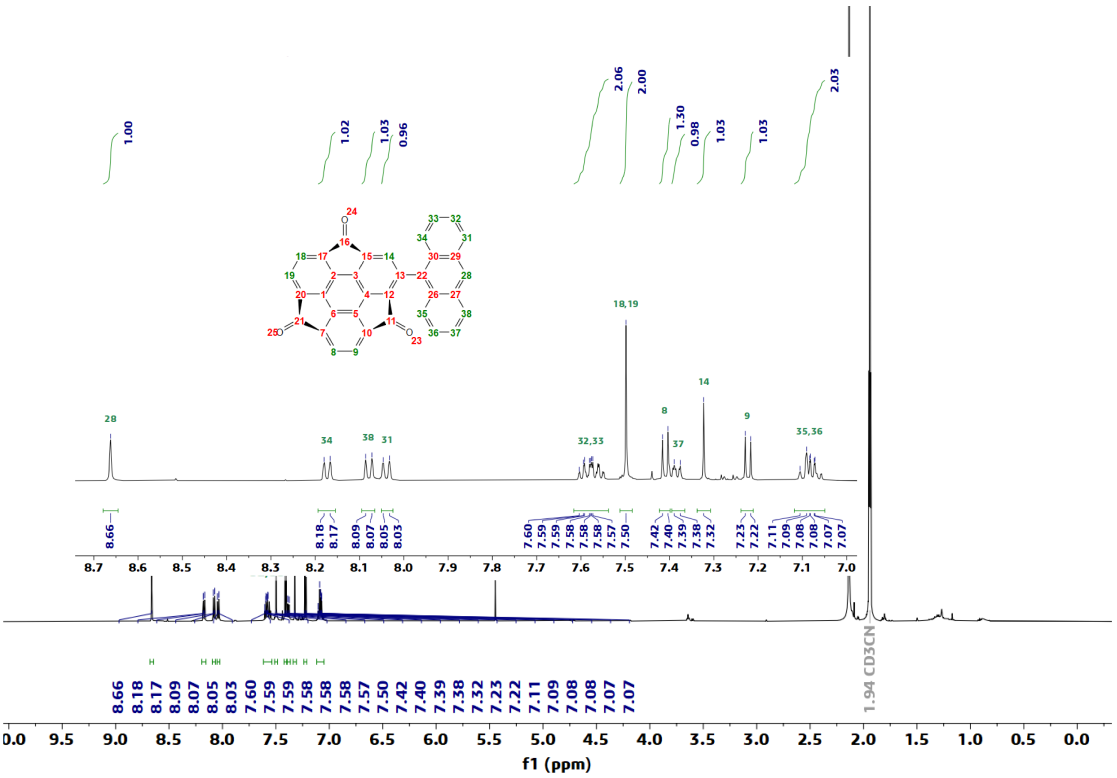

2D NMR Correlation (COSY) spectra of **An-TOS** aromatic region in chloroform-*d* at 300 K.

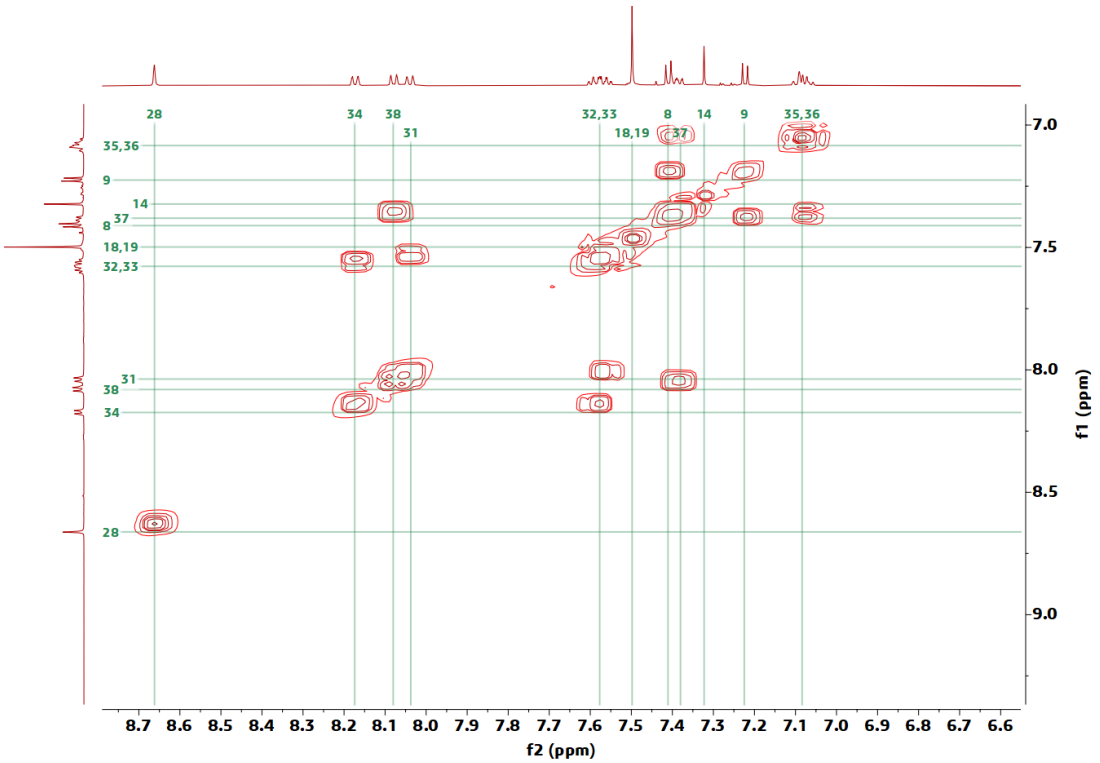

^{13}C NMR spectrum of **An-TOS** (100 MHz, Chloroform-*d*, 300 K).

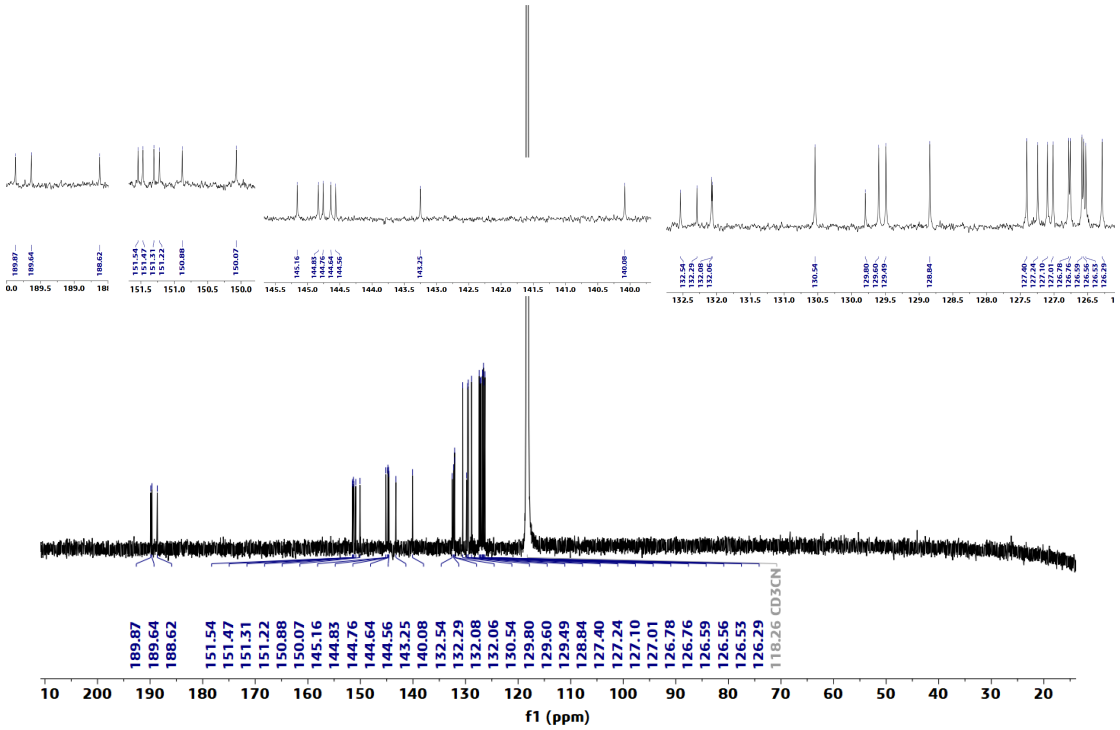

Fig. ^{13}C NMR spectrum of Anthracenetrioxosumanene (100 MHz, Acetonitrile-d_3, 300 K).

References

1. X. Shi, X. Liao, K. Gao, L. Zuo, J. Chen, J. Zhao, F. Liu, Y. Chen and A. K. Y. Jen, *Adv. Funct. Mater.*, 2018, **28**, 1802324.
2. D.-H. Kim, A. D'aléo, X.-K. Chen, A. D. Sandanayaka, D. Yao, L. Zhao, T. Komino, E. Zaborova, G. Canard and Y. Tsuchiya, *Nat. Photonics*, 2018, **12**, 98.
3. Q. Huaulmé, A. Sutter, S. Fall, D. Jacquemin, P. Lévêque, P. Retailleau, G. Ulrich and N. Leclerc, *J. Mater. Chem. C*, 2018, **6**, 9925.
4. Z. Guo, S. Park, J. Yoon and I. Shin, *Chem. Soc. Rev.*, 2014, **43**, 16.
5. R. Weinstain, T. Slanina, D. Kand and P. Klan, *Chem. Rev.*, 2020, **120**, 13135.
6. L. Wang, W. Du, Z. Hu, K. Uvdal, L. Li and W. Huang, *Angew. Chem. Int. Ed.*, 2019, **58**, 14026.
7. P. Brogdon, H. Cheema and J. H. Delcamp, *ChemSusChem*, 2018, **11**, 86.
8. P. M. Beaujuge, W. Pisula, H. N. Tsao, S. Ellinger, K. Müllen and J. R. Reynolds, *J. Am. Chem. Soc.*, 2009, **131**, 7514.
9. J. D. Yuen, R. Kumar, D. Zakhidov, J. Seifter, B. Lim, A. J. Heeger and F. Wudl, *Adv. Mater.*, 2011, **23**, 3780.
10. T. Steckler, M. Lee, Z. Chen, O. Fenwick, M. R. Andersson, F. Cacialli and H. Sirringhaus, *J. Mater. Chem. C*, 2014, **2**, 5133.
11. P. Murto, A. Minotto, A. Zampetti, X. Xu, M. R. Andersson, F. Cacialli and E. Wang, *Adv. Opt. Mater.*, 2016, **4**, 2068.
12. K. Narayanaswamy, A. Venkateswararao, V. Gupta, S. Chand and S. P. Singh, *Chem. Commun.*, 2016, **52**, 210.
13. Y. Zhang, S. K. Hau, H.-L. Yip, Y. Sun, O. Acton and A. K.-Y. Jen, *Chem. Mater.*, 2010, **22**,

2696.

14. J. T. Buck, A. M. Boudreau, A. DeCarmine, R. W. Wilson, J. Hampsey and T. Mani, *Chem*, 2019, **5**, 138.

15. S. Higashibayashi, B. B. Shrestha, Y. Morita, M. Ehara, K. Ohkubo, S. Fukuzumi and H. Sakurai, *Chem. Lett.*, 2014, **43**, 1297.

16. T. Amaya, M. Hifumi, M. Okada, Y. Shimizu, T. Moriuchi, K. Segawa, Y. Ando and T. Hirao, *J. Org. Chem.*, 2011, **76**, 8049.

17. J. Han, Y. Uetake, Y. Yakiyama and H. Sakurai, *Chem. Commun.*, 2023, **59**, 4632.

18. K. Kanahara, M. M. R. Badal, S. Hatano, M. Abe, S. Higashibayashi, N. Takashina and H. Sakurai, *Bull. Chem. Soc. Jpn.*, 2015, **88**, 1612.

19. J. Sworakowski, *Synth. Met.*, 2018, **235**, 125.

20. E. T. Seo, R. F. Nelson, J. M. Fritsch, L. S. Marcoux, D. W. Leedy and R. N. Adams, *J. Am. Chem. Soc.*, 1966, **88**, 3498.

21. M. Soltani, R. Minakar, H. R. Memarian and H. Sabzyan, *J. Phys. Chem. A*, 2019, **123**, 2820.

22. N. Aizawa, A. Matsumoto and T. Yasuda, *Sci. Adv.*, 2021, **7**, eabe5769.

23. T. Kobayashi, A. Niwa, K. Takaki, S. Haseyama, T. Nagase, K. Goushi, C. Adachi and H. Naito, *Phys. Rev. Appl.*, 2017, **7**, 034002.

24. J. M. Dos Santos, D. Hall, B. Basumatary, M. Bryden, D. Chen, P. Choudhary, T. Comerford, E. Crovini, A. Danos and J. De, *Chem. Rev.*, 2024, **124**, 13736.

25. Y. Xiong, J. Gong, J. Liu, D. Wang, H. Wu, Z. Zhao, M. Fang, Z. Li, D. Wang and B. Z. Tang, *J. Mater. Chem. C*, 2022, **10**, 10009.

26. L. Zhan, Z. Chen, S. Gong, Y. Xiang, F. Ni, X. Zeng, G. Xie and C. Yang, *Angew. Chem.*, 2019, **131**, 17815.

27. L. Huang, L. Liu, X. Li, H. Hu, M. Chen, Q. Yang, Z. Ma and X. Jia, *Angew. Chem. Int. Ed.*, 2019, **58**, 16445.

28. S. Dey, M. Hasan, A. Shukla, N. Acharya, M. Upadhyay, S.-C. Lo, E. B. Namdas and D. Ray, *J. Phys. Chem. C*, 2022, **126**, 5649.

29. I. Bhattacharjee, N. Acharya, H. Bhatia and D. Ray, *J. Phys. Chem. Lett.*, 2018, **9**, 2733.

30. F. Chen, Q. Yu, Y. Guo and M. Fan, *Sci China Ser B*, 1991, **34**, 135.

31. O. Yurchenko, D. Freytag, L. zur Borg, R. Zentel, J. r. Heinze and S. Ludwigs, *J. Phys. Chem. B*, 2012, **116**, 30.

32. B. H. Drummond, N. Aizawa, Y. Zhang, W. K. Myers, Y. Xiong, M. W. Cooper, S. Barlow, Q. Gu, L. R. Weiss and A. J. Gillett, *Nat. Commun.*, 2021, **12**, 4532.

33. M. Abe, *Chem. Rev.*, 2013, **113**, 7011.

34. P. Xu, R. Hojo and Z. M. Hudson, *Chem. Eur. J.*, 2023, **29**, e202203585.

35. J. Wagner, P. Zimmermann Crocomo, M. A. Kochman, A. Kubas, P. Data and M. Lindner, *Angew. Chem.*, 2022, **134**, e202202232.

36. T. Nakagawa, K. Okamoto, H. Hanada and R. Katoh, *Opt. Lett.*, 2016, **41**, 1498.

37. G. Reynolds and K. Drexhage, *Opt. Commun.*, 1975, **13**, 222.

38. J. J. Snellenburg, S. Laptenok, R. Seger, K. M. Mullen and I. H. Van Stokkum, *J. Stat. Softw.*, 2012, **49**, 1.

39. J. R. Lakowicz, *Principles of fluorescence spectroscopy*, Springer, 2006.

40. M. J. Frisch, G. W. Trucks, H. B. Schlegel, G. E. Scuseria, M. A. Robb, J. R. Cheeseman, G. Scalmani, V. Barone, G. A. Petersson, H. Nakatsuji, X. Li, M. Caricato, A. V. Marenich, J. Bloino, B. G. Janesko, R. Gomperts, B. Mennucci, H. P. Hratchian, J. V. Ortiz, A. F. Izmaylov, J. L. Sonnenberg, Williams, F. Ding, F. Lipparini, F. Egidi, J. Goings, B. Peng, A. Petrone, T.

Henderson, D. Ranasinghe, V. G. Zakrzewski, J. Gao, N. Rega, G. Zheng, W. Liang, M. Hada, M. Ehara, K. Toyota, R. Fukuda, J. Hasegawa, M. Ishida, T. Nakajima, Y. Honda, O. Kitao, H. Nakai, T. Vreven, K. Throssell, J. A. Montgomery Jr., J. E. Peralta, F. Ogliaro, M. J. Bearpark, J. J. Heyd, E. N. Brothers, K. N. Kudin, V. N. Staroverov, T. A. Keith, R. Kobayashi, J. Normand, K. Raghavachari, A. P. Rendell, J. C. Burant, S. S. Iyengar, J. Tomasi, M. Cossi, J. M. Millam, M. Klene, C. Adamo, R. Cammi, J. W. Ochterski, R. L. Martin, K. Morokuma, O. Farkas, J. B. Foresman and D. J. Fox.*Journal*, 2016.

41. T. Lu and F. Chen, *J. Comput. Chem.*, 2012, **33**, 580.

42. W. Humphrey, A. Dalke and K. Schulten, *J. Mol. Graph.*, 1996, **14**, 33.

43. P. K. Samanta, D. Kim, V. Coropceanu and J.-L. Brédas, *J. Am. Chem. Soc.*, 2017, **139**, 4042.

44. F. Neese, *WIREs Comput. Mol. Sci.*, 2018, **8**, e1327.

45. M. Casanova-Páez and L. Goerigk, *J. Chem. Theory Comput.*, 2021, **17**, 5165.

46. D. Mester and M. Kállay, *J. Chem. Theory Comput.*, 2022, **18**, 1646.

Conclusions

In this doctoral dissertation, the author has explored the unique potential of curved-π molecular systems based on sumanene and trioxosumanene for functional material development, with a particular focus on optoelectronic applications. Through systematic molecular design, synthetic innovation, and photophysical investigations, this work has demonstrated that incorporating intrinsically strained bowl-shaped π-frameworks provides unprecedented advantages in charge transfer dynamics, electron-accepting capabilities, and excited-state behavior. The outcomes not only overcome long-standing synthetic challenges but also offer new insights into molecular curvature–function relationships and present promising opportunities for future applications in advanced organic optoelectronic devices.

In Chapter 2, the author successfully synthesized four sumanene-ligated Ru(II) terpyridine complexes (**C1–C4**). All complexes exhibited significantly enhanced emission properties compared to conventional terpyridylphenyl analogues upon excitation at the ligand-centered π–π* band. Notably, those containing phenylene linker units displayed dual emission attributable to twisted intramolecular charge transfer (TICT), which is facilitated by rapid intramolecular rotation due to the low rotation barrier between sumanene and the adjacent terpyridine in the excited state. Furthermore, cation recognition experiments demonstrated a high susceptibility toward Li^+ trapping at the sumanene core. These findings contribute to the deeper understanding of the bowl-shape effect in curved-π emissive systems and broaden the applicability of sumanene-based materials in molecular sensing.

In Chapter 3, To address the intrinsic difficulty associated with functionalization at the aromatic

periphery of trioxosumanene, the author use the Lewis acid-mediated Suzuki–Miyaura coupling strategy by bromotrioxosumanene as a key intermediate, enabling the preparation of a series of novel coupling products. Photophysical analyses confirmed the exceptional electron-accepting nature of the trioxosumanene moiety. Intriguingly, for the 2-hydroxyphenyl derivative, a spontaneous ring-opening reaction at the adjacent pentagonal ring occurred even at room temperature without any added activation, which can be attributed to strain release. This discovery introduces a rational approach for the chemical utilization of trioxosumanene as a new type of curved-π electron acceptor. Further studies focusing on energy gap modulation via donor incorporation will provide promising directions for the integration of trioxosumanene into optoelectronic device materials.

In Chapter 4, the author designed and synthesized **TPA**–**TOS**, a novel donor–acceptor (D–A) near-infrared (NIR) dye that utilizes a rigid bowl-shaped acceptor (**TOS**) and strong electron donor (**TPA**) without relying on extended conjugation or complex architectures. This molecular design successfully establishes an efficient system exhibiting both TADF and RTP, achieving high-efficiency NIR emission with an outstanding quantum yield. In non-polar hexane, the exciton undergoes efficient charge separation leading to a long-lived CS state, whereas in polar MeCN rapid relaxation suppresses emission. Although further theoretical investigation is required, the **TOS** curvature clearly enhances solubility in non-polar solvents and induces strong SOC, facilitating ISC between ^{1}CT and ^{3}CT states. This work demonstrates that curved-π frameworks offer a powerful design platform for constructing simplified yet high-performance NIR dyes, presenting new opportunities for future optoelectronic applications.

Collectively, this thesis highlights the extraordinary potential of bowl-shaped curved π-systems as emerging functional motifs in organic materials. By establishing synthetic strategies, revealing

structure–property relationships, and demonstrating high-efficiency optoelectronic output, this work provides fundamental insights and valuable guidance for future molecular design. The approaches presented herein not only advance the understanding of curved-π photophysics and electron transfer dynamics but also pave the way toward innovative materials for next-generation organic electronic and photonic technologies.

List of Publications

The content of this thesis has been published in the following papers.

Copyright

Acknowledgments

I would like to express my sincere gratitude to Professor Hidehiro Sakurai for providing a comprehensive research environment, as well as invaluable guidance and encouragement throughout the course of my doctoral research. I am deeply grateful to Associate Professor Yumi Yakiyama for her careful supervision, insightful advice on data analysis, and extensive knowledge. I also sincerely thank Assistant Professor Yuta Uetake for his helpful advice during my research and for generously sharing his expertise.

I would like to express my sincere gratitude to Professor Takahiro Kozawa and Professor Ken-ichi Nakayama for reviewing my doctoral dissertation and for their suggestions and advice.

I would like to thank Associate Professor Youhei Takeda (University of Osaka), Associate Professor Hayato Sakai (Keio University), Professor Taku Hasobe (Keio University) for their cooperation in spectroscopic analysis. Associate Professor Ryohei Kishi (University of Osaka), Professor Kei Ohkubo (University of Osaka) for their cooperation in theoretical analysis and computational studies.

I would like to express my appreciation to all former and current members of the Sakurai Laboratory. I would like to thank Mr. Zhou Dongyi, Dr. Li Minghong, Mr. Wang Chaoyu, Mr. Shi Yuqing, Dr. Nazgul Assan, Dr. Sitanan Sartyoungkul, Dr. Artur Kasprzak, Ms. Michiko Ebukuro, Dr. Barana Hettirachchi, Dr. Threeraphat Chutimasakul, Dr. Butsaratip Suwattanuruk, Ms. Svetlana Em, Ms. Yuka Motohashi, Mr. Takumi Hasegawa, Dr. Maiki Nishimoto, Dr. Hironobu Nakazawa, Ms. Mio Nishimura, Mr. Katsuaki Iwasa, and Mr. Shinji Kubota for their support, helpful discussions, and the enjoyable research atmosphere they created.

Finally, I would like to express my deepest gratitude to my father, Han Xiaofeng, my mother, Wang Liping, and my wife, Wei Meng, as well as my newborn son, Han Youchen (Popeye). It is your love and support that sustained me throughout this journey.